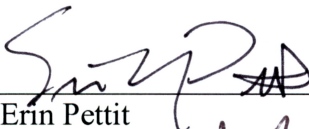


MAPPING METHODS AND OBSERVATIONS OF SURFICIAL SNOW/ICE COVER
AT REDOUBT AND PAVLOF VOLCANOES, ALASKA USING OPTICAL
SATELLITE IMAGERY

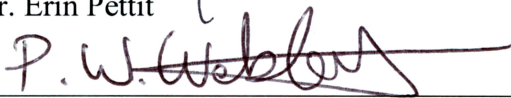
By

Kristen E. Rahilly

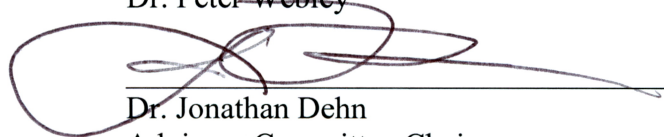
RECOMMENDED:



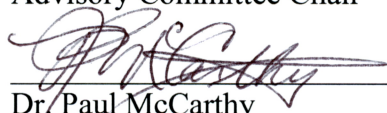
Dr. Erin Pettit



Dr. Peter Webley

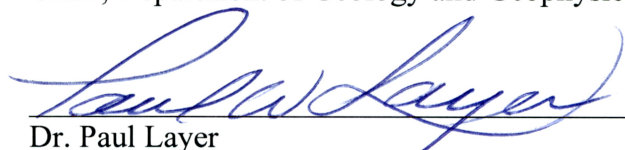


Dr. Jonathan Dehn
Advisory Committee Chair

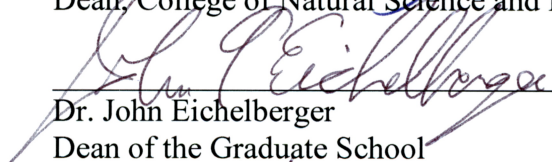


Dr. Paul McCarthy
Chair, Department of Geology and Geophysics

APPROVED:



Dr. Paul Layer
Dean, College of Natural Science and Mathematics



Dr. John Eichelberger
Dean of the Graduate School



Date

MAPPING METHODS AND OBSERVATIONS OF SURFICIAL SNOW/ICE COVER
AT REDOUBT AND PAVLOF VOLCANOES, ALASKA USING OPTICAL
SATELLITE IMAGERY

A
THESIS

Presented to the Faculty
of the University of Alaska Fairbanks

in Partial Fulfillment of the Requirements
for the Degree of

MASTER OF SCIENCE

By

Kristen E. Rahilly, B.A.

Fairbanks, Alaska

August 2014

Abstract

Alaska is a natural laboratory for the study of how active volcanism interacts with underlying seasonal snow, perennial snow, and glacial ice cover. While over half of the historically active volcanoes in Alaska have some degree of perennial snow or glacial ice, all Alaskan volcanoes have a covering of seasonal snow for a period of time throughout the year. Previous research has centered on how volcanic deposits erode away the underlying snow/ice cover during an eruption, producing volcanic mudflows called lahars. Less emphasis has been placed on how variations in the snow/ice cover substrate affect the efficiency of meltwater generation during a volcanic eruption. Glacial ice, perennial snow, and seasonal snow can all contribute significantly to meltwater, and therefore the variations in the types of snow/ice cover present at Alaskan volcanoes must be analyzed. By examining the changing spatial extent of seasonal snow present at a volcano during multiple Alaskan summers, the approximate boundaries of perennial snow and ice can be mapped as the snow/ice cover consistently present at the end of each ablation season. In this study, two methods of snow/ice cover mapping for Redoubt and Pavlof volcanoes are analyzed for efficiency and accuracy. Identification of the best method allows for mapping of the snow/ice cover consistently present during each Alaskan summer month over at least two different years. These maps can serve as approximations for the snow/ice cover likely to be present at both volcanoes during each summer month. Volcanic deposits produced during the 2009 Redoubt and 2013 Pavlof eruptions are spatially linked to these snow/ice cover maps so that future research can focus on the interaction between deposits and type of snow/ice substrate. Additional

observations and conclusions are made regarding how the visible snow/ice cover varies during and after each eruption.

	Page
Signature Page.....	i
Title Page	iii
Abstract.....	v
Table of Contents	vii
List of Figures.....	xi
List of Tables	xv
Acknowledgments	xvii
Chapter 1 Introduction.....	1
1.1 Background.....	1
1.2 Comparison of snow/ice cover mapping methods for Alaskan volcanoes	2
1.3 Mapping snow/ice on Redoubt and Pavlof during quiescence and eruption	4
1.4 Summary of final outcomes	5
1.5 References.....	6
Chapter 2 Methods for snow/ice cover mapping of Redoubt and Pavlof volcanoes using optical satellite imagery	9
2.1 Introduction.....	9
2.1.1 Satellite remote sensing of glaciers and snow cover in Alaska	10
2.1.2 Previous work and methods for studying snow/ice on volcanoes	12
2.1.3 Challenges of mapping snow/ice cover at Alaskan volcanoes	13
2.2 Setting of Redoubt volcano.....	14
2.2.1 Basic setting of Redoubt volcano	14

2.3	Setting of Pavlof volcano.....	15
2.3.1	Basic setting of Pavlof volcano.....	15
2.4	Methods.....	16
2.4.1	Previous work in snow/ice cover mapping using satellite imagery	16
2.4.2	Sensors used for snow/ice cover mapping.....	17
2.4.3	Pre-processing of satellite imagery.....	18
2.4.4	Methods used to map snow/ice cover at Redoubt and Pavlof	20
2.4.5	Technique 1: band ratios.....	21
2.4.6	Technique 2: principal component analysis.....	23
2.4.7	Technique 3: linear spectral unmixing.....	24
2.5	Results and discussion	26
2.5.1	Snow/ice cover mapping using threshold method	27
2.5.2	Snow/ice cover mapping using linear spectral unmixing method	31
2.5.3	Improvements to linear spectral unmixing method for snow/ice cover mapping.....	35
2.5.4	Validation of results.....	38
2.6	Conclusion	40
2.7	Figures.....	42
2.8	Tables.....	63
2.9	References.....	68
Chapter 3	Observations of surficial snow/ice cover changes due to seasonal and eruptive influences on Redoubt and Pavlof volcanoes, Alaska using optical remote sensing	73

3.1	Introduction.....	74
3.1.1	Alaskan volcanoes	75
3.2	Volcano – snow/ice interactions	76
3.2.1	Short term interactions.....	76
3.2.2	Long term interactions	79
3.2.3	Lahar formation and hazards	80
3.2.4	Influence of snow/ice substrate type on lahar generation.....	82
3.3	Background on Redoubt volcano.....	82
3.3.1	Setting of Redoubt volcano.....	82
3.3.2	Recent eruptions at Redoubt volcano	83
3.3.3	Eruption effects on Drift Glacier	84
3.3.4	Lahar hazards at Redoubt volcano.....	85
3.4	Background on Pavlof volcano.....	86
3.4.1	Setting of Pavlof volcano.....	86
3.4.2	Recent eruptions at Pavlof volcano.....	87
3.4.3	Lahar hazards at Pavlof volcano.....	88
3.5	Methods.....	89
3.5.1	Sensors used to create Products 1, 2, and 3	90
3.5.2	Methods used to produce Product 1: individual snow/ice cover maps.....	91
3.5.3	Methods used to produce Product 2: snow/ice cover summary maps	92
3.5.4	Methods used to produce Product 3: composite maps of eruptive deposits and snow/ice cover.....	94
3.6	Results and discussion	95

3.6.1	Product 1: individual snow/ice cover maps of Redoubt subset	95
3.6.2	Product 2: snow/ice cover summary maps of Redoubt subset.....	97
3.6.3	Product 3: composite maps of eruptive deposits and snow/ice cover of Redoubt subset.....	101
3.6.4	Product 1: individual snow/ice cover maps of Pavlof subset	108
3.6.5	Product 2: snow/ice cover maps of Pavlof subset.....	111
3.6.6	Product 3: composite maps of eruptive deposits and snow/ice cover of Pavlof subset	114
3.7	Conclusion	118
3.8	Figures.....	122
3.9	Tables.....	150
3.10	References.....	158
Chapter 4	Conclusion	163
4.1	Comparison of snow/ice cover mapping methods for Alaskan volcanoes	163
4.2	Mapping snow/ice on Redoubt and Pavlof during quiescence and eruption .	165
4.3	Limitations and future work.....	168
4.4	References.....	170

List of Figures

	Page
Figure 2.1: Introduction to Redoubt and Pavlof volcanoes	42
Figure 2.2: Alaskan glaciers mapped by GLIMS and World Glacier Inventory	43
Figure 2.3: Location of Redoubt study area used for analysis.....	44
Figure 2.4: Location of Pavlof study area used for analysis.....	45
Figure 2.5: Snow/ice pixels mapped in Redoubt subset using threshold method.....	46
Figure 2.6: Snow/ice pixels mapped in Pavlof subset using threshold method.....	47
Figure 2.7: Landsat 5 TM June 29, 2006 natural color and NDSI images of Redoubt	48
Figure 2.8: Landsat 5 TM June 29, 2006 threshold images of the Drift Glacier lobe	49
Figure 2.9: Landsat 7 ETM+ June 17, 2012 band ratio and PC images of Pavlof	50
Figure 2.10: Landsat 5 TM May 16, 2009 natural color and PC images of Pavlof.....	51
Figure 2.11: Landsat 5 TM May 16, 2009 natural color and endmember selection images of Pavlof	52
Figure 2.12: Landsat 5 TM May 16, 2009 linear spectral unmixing images of Pavlof.....	53
Figure 2.13: Landsat 7 ETM+ June 17, 2012 natural color and endmember selection images of Pavlof	54
Figure 2.14: Landsat 7 ETM+ June 17, 2012 linear spectral unmixing images of Pavlof	55
Figure 2.15: Comparison of snow/ice pixels mapped at Pavlof using threshold and linear spectral unmixing methods	56
Figure 2.16: Landsat 5 TM from June 29, 2006 linear spectral unmixing and band ratio images of the Drift Glacier lobe.....	57
Figure 2.17: Comparison of snow/ice pixels mapped at Redoubt using threshold and linear spectral unmixing.....	58

Figure 2.18: Landsat 7 ETM+ May 10, 2005 endmember and linear spectral unmixing images of Redoubt	59
Figure 2.19: Landsat 7 ETM+ May 10, 2005 multiple-iteration image of Redoubt.....	60
Figure 2.20: Landsat 7 ETM+ May 13, 2006 natural color and linear spectral unmixing images of Redoubt	61
Figure 2.21: Validation of linear spectral unmixing method.....	62
Figure 3.1: Location map of Redoubt and Pavlof volcanoes within Alaska	122
Figure 3.2: Spatial extent of the Redoubt subset	123
Figure 3.3: Spatial extent of the Pavlof and Pavlof Sister subsets.....	124
Figure 3.4: Snow/ice area of individual Redoubt images	125
Figure 3.5: Daily maximum radiant AVHRR band 3 temperatures for the Redoubt area.....	126
Figure 3.6: Range of dates for the first appearance of seasonal snow after the ablation season for the Redoubt subset.....	127
Figure 3.7: Snow/ice area mapped in the Redoubt monthly summary images.....	128
Figure 3.8: May and June monthly snow/ice summary maps for Redoubt	129
Figure 3.9: July, August, and September monthly snow/ice summary maps for Redoubt	130
Figure 3.10: Summary of webcam imagery of Redoubt volcano from May – September	131
Figure 3.11: Snow/ice cover mapped within the Redoubt subset on March 18	132
Figure 3.12: Lahar channels visible at Redoubt volcano on March 26, 2009	133
Figure 3.13: Lahar channels visible at Redoubt volcano on April 1, 2009	134
Figure 3.14: Lahar channels visible at Redoubt volcano on April 4, 2009	135
Figure 3.15: Lahar channels on April 4 that were reused from the March 26 – April 1 lahars	136

Figure 3.16: Analysis of visible snow/ice area after the 2009 Redoubt eruption	137
Figure 3.17: Webcam imagery of Redoubt volcano on April 20 and May 12, 2009.....	138
Figure 3.18: Snow/ice area of individual Pavlof and Pavlof Sister images	139
Figure 3.19: Range of dates for the first appearance of seasonal snow after the ablation season for the Pavlof subset.....	140
Figure 3.20: Daily maximum radiant AVHRR band 3 temperatures for the Pavlof area	141
Figure 3.21: April and October images of the Pavlof and Pavlof Sister subsets	142
Figure 3.22: Snow/ice area mapped in the Pavlof and Pavlof Sister monthly summary images	143
Figure 3.23: April, May, and June monthly snow/ice summary maps for Pavlof and Pavlof Sister subsets	144
Figure 3.24: July, August, and October monthly snow/ice summary maps for Pavlof and Pavlof Sister subsets.....	145
Figure 3.25: Images showing significant deposits from May 16 – June 28 in the 2013 Pavlof eruption.....	146
Figure 3.26: Propagation direction of major ash emissions between May 16 – June 25 in the 2013 Pavlof eruption.....	147
Figure 3.27: Snow/ice cover and deposit maps for the May 13 – May 19 2013 Pavlof eruption.....	148
Figure 3.28: Snow/ice cover and deposit maps for the May 13 – May 19 and June 4 – 29 2013 Pavlof eruption	149

List of Tables

	Page
Table 2.1: Sensors used to map snow/ice cover at Redoubt and Pavlof volcanoes	63
Table 2.2: Method combinations used to map snow/ice cover with thresholding for Redoubt study area.....	64
Table 2.3: Method combinations used to map snow/ice cover with thresholding for Pavlof study area.....	65
Table 2.4: Data for linear spectral unmixing iterations of Redoubt study area	66
Table 2.5: Data for linear spectral unmixing iterations of Pavlof study area	67
Table 3.1: Sensors used to map the snow/ice cover area and eruptive products at Redoubt and Pavlof.....	150
Table 3.2: Percent variance and total difference between monthly summaries of snow/ice area at the Redoubt subset	151
Table 3.3: Summary of main 2009 eruptive events and deposits at Redoubt.....	152
Table 3.4: Summary of Redoubt lahar channel measurements.....	153
Table 3.5: Percent variance and total difference between the snow/ice area at the Pavlof and Pavlof Sister subsets	154
Table 3.6: Percent variance and total area difference between monthly summaries of snow/ice area at the Pavlof and Pavlof Sister subsets.....	155
Table 3.7: Summary of main 2013 eruptive events and deposits produced at Pavlof	156
Table 3.8: Summary of 2013 Pavlof deposit measurements.....	157

Acknowledgements

This project was supported financially by the Alaska Satellite Facility, the Department of Geology and Geophysics at the University of Alaska Fairbanks (UAF), the Alaska Volcano Observatory, and the NSF Changing Alaska Science Education (CASE) program out of UAF. The inspiration for this project was largely conceived through a number of graduate classes at UAF and I would especially like to thank Drs. Anupma Prakash and Christian Haselwimmer, who provided invaluable advice related to the methodology of this project.

I would like to thank my committee members: Drs. Jon Dehn (chair), Peter Webley, and Erin Pettit for their support and advice on this project. I am grateful to Dr. Webley and Dr. Pettit for their extensive and thoughtful edits on multiple copies of this thesis. I would like to thank my advisor, Dr. Dehn, for supporting my interests in this project, no matter where they led. I would also like to thank Dr. Dehn for bringing me up to Alaska to study volcanoes, something that has been a goal of mine for many years.

Finally, I would like to thank my family for their continual support of my graduate school work in Alaska. I would also like to thank Zebulon Maharrey for being there through everything from the very first day I arrived in Alaska.

Chapter 1 Introduction

1.1 Background

More than 50 volcanoes have been active in Alaska within the last 200 years, the majority of which are located along the 2,500 km long Aleutian Arc (Schaefer and Nye, 2008). The expansive area over which Alaskan volcanoes can be found is both remote and sparsely populated, making it a challenge to monitor daily changes in activity (Dean et al., 2002). Therefore, observing relative changes in activity has become a pivotal component of monitoring remote Alaskan volcanoes. This is done by understanding how a volcano behaves and its general characteristics during times of quiescence (Dean et al., 2002). Background levels of thermal output, ash/steam emissions, and seismic activity have been monitored at Alaskan volcanoes so that, during times of increased activity, abnormalities can be better understood (Dehn et al., 2000; Webley et al., 2009; Werner et al., 2011; Buurman et al., 2013). In this study, background levels of perennial snow, glacial ice, and seasonal snow will be mapped for two Alaskan volcanoes: Redoubt and Pavlof.

Perennial snow or ice cover can be found to some extent on over 30 Holocene-aged Alaskan volcanoes (Wessels et al., 2007), while seasonal snow covers most of the state of Alaska for at least six months out of the year (Shulski and Wendler, 2007). In this thesis, the seasonal snow, perennial snow, and glacial ice will be referred to together as snow/ice cover. Similar to non-volcanic Alaskan glaciers, the snow/ice cover on a volcano is subjected to changes in regional climate and precipitation. Previous work in Alaska has shown that even glaciers within the same 30 km radius may undergo different

climate conditions (Arendt et al., 2002). An additional challenge to monitoring Alaskan glaciers over time is that, dependent on glacier size and location, it may take up to 40 years for a glacial system to respond to a change in climate (Arendt et al., 2002). All of these challenges are then compounded when studying glaciers on volcanoes, where both climatological and volcanological influences can be relevant (Rivera et al., 2006). The overarching goal of this study is to analyze how both of these influences affect snow/ice cover on two Alaskan volcanoes. This will be achieved by first identifying the background spatial extent of snow/ice present at each volcano throughout multiple ablation seasons, when the seasonal snow varies dramatically and the maximum extent of perennial snow and ice can be established (Boresjö Bronge and Bronge, 1999; Sijak and Wheate, 1999; Xiao et al., 2001). Once background snow/ice area is measured, the effects an eruption has on the snow/ice cover can be better understood. Before any conclusions can be made about the snow/ice cover area at Redoubt and Pavlof, an effective mapping method must be ascertained.

1.2 Comparison of snow/ice cover mapping methods for Alaskan volcanoes

Chapter two will focus on a number of possible methods used to map snow/ice cover. Satellite imagery has been identified as a useful tool for mapping snow/ice cover, especially in remote areas where frequent field-based mapping may be challenging (König et al., 2001). In this thesis, all of the satellite imagery analyzed came from optical satellites, instruments that are sensitive to the visible and infrared wavelengths of the electromagnetic spectrum (Lillesand et al., 2008). Much of the previous research has

focused on mapping glacial ice in both the icefield and alpine environments (see Boresjö Bronge and Bronge, 1999; Sidjak and Wheate, 1999; Paul, 2000; Rivera et al., 2007; Gjermundsen et al., 2011). There has also been an effort to map daily changes in global glacier ice cover. Many global coverage maps of snow/ice, used for monitoring purposes, utilize lower spatial resolution sensors that acquire daily images such as the Moderate Resolution Imaging Spectroradiometer (MODIS) and the Advanced Very High Resolution Radiometer (AVHRR) (Hall et al., 1998; Xiao et al., 2001; Dozier and Painter, 2004). While the use of these sensors may work effectively for large ice sheets, sub-pixel variations in snow/ice cover are lost due to the integration of data over a larger spatial resolution pixel (König et al., 2001). In order to better study the smaller scale snow/ice cover features present at Redoubt and Pavlof volcanoes, higher spatial resolution sensors, such as those on the Landsat and Earth Observing 1 satellites, will be used. These sensors have longer amounts of time between image acquisitions but will be sufficient in mapping the snow/ice cover at both volcanoes.

Two different methods of snow/ice cover mapping will be compared using subsets from areas surrounding both Pavlof and Redoubt. All image processing will be completed using ENVI 4.5 Image Analysis Software. The purpose of Chapter 2 is to analyze which method most effectively maps the snow/ice cover. In this case, the most effective method will map the greatest proportion of snow/ice cover with the smallest amount of noise or background included. Additionally, the best method should preferably require the least amount of user input.

1.3 Mapping snow/ice on Redoubt and Pavlof during quiescence and eruption

Chapter 3 will utilize the methods from Chapter 2 to map the snow/ice cover at subsets surrounding the areas around Redoubt and Pavlof volcanoes. In order to analyze the presence of volcanological influences on snow/ice cover, the Pavlof subset will be compared with a subset of similar area around Pavlof Sister. Pavlof Sister is a volcano that has not erupted in the past 200 years but is located approximately 5 km north-northwest of Pavlof, ensuring that the two volcanoes experience the same climate (Rivera et al., 2006; Waythomas et al., 2006). The results in Chapter 3 will be broken up into the creation of three different products:

Product 1.) Snow/ice cover maps of individual images from the Alaskan summer ablation season,

Product 2.) Summer monthly maps showing the snow/ice cover consistently present during multiple years for each month,

Product 3.) Maps spatially linking the snow/ice cover present with deposits produced during the 2009 eruption of Redoubt and 2013 eruption of Pavlof.

An additional component to Product 3 will be comparing the visible snow/ice cover area present directly before, during, and after an eruption to the expected snow/ice cover measured in the monthly summary maps from Product 2. All three products will be completed for both Redoubt and Pavlof volcanoes. Products 1 and 2 will also be created for Pavlof Sister in order to make comparisons with Pavlof.

1.4 Summary of final outcomes

This thesis will combine previous efforts made within the remote sensing and glaciological communities to map snow/ice cover with volcanological interpretations of eruptive activity. There are three main goals for the project: 1.) identification of the most efficient and effective method for mapping the snow/ice cover at remote Alaskan volcanoes using optical satellite imagery; 2.) determination of the variations in snow/ice cover during the Alaskan summer months at Redoubt and Pavlof in order to delineate areas of perennial snow and ice from seasonal snow; and 3.) an analysis on the intersection between snow/ice cover type and overlying volcanic products emplaced during an eruption. As first author on all the chapters of this thesis, I was responsible for acquiring and processing the satellite imagery as well as completing all analyses and recording results. It is my goal that the methods analyzed within this thesis can serve as a basis for the creation of a snow/ice cover database at all remaining Alaskan volcanoes as well as for further work in understanding how snow/ice cover type influences the generation of meltwater-related hazards during a volcanic eruption.

References

- Arendt, A.A., Echelmeyer, K.A., Harrison, W.D., Lingle, C.S., and Valentine, V.B. 2002: Rapid Wastage of Alaska Glaciers and Their Contribution to Rising Sea Level: *Science*, v. 297, n. 5580, 382 – 386.
- Boresjö Bronge, L. and Bronge, C. 1999: Ice and snow-type classification in the Vestfold Hills, East Antarctica, using Landsat-TM data and ground radiometer measurements: *International Journal of Remote Sensing*, v. 20, n. 2, 225 – 240.
- Buurman, H., West, M.E., and Thompson, G. 2013: The seismicity of the 2009 Redoubt eruption: *Journal of Volcanology and Geothermal Research*, v. 259, 16 – 30.
- Dean, K.G., Dehn, J., Engle, K., Izbekov, P., Papp, K., and Patrick, M. 2002: Operational Satellite Monitoring of Volcanoes at the Alaska Volcano Observatory: *Advances in Environmental Monitoring and Modeling*, v. 1, no. 1, 70 – 97.
- Dehn, J., Dean, K., and Engle, K. 2000: Thermal monitoring of North Pacific volcanoes from space: *Geology*, v. 28, no. 8, 755-758.
- Dozier, J. and Painter, T.H. 2004: Multispectral and Hyperspectral Remote Sensing of Alpine Snow Properties: *Annual Review of Earth and Planetary Sciences*, v. 32, 465-494.
- Gjermundsen, E.F., Mathieu, R., Käab, R., Chinn, T., Fitzharris, B., Hagen, J.O. 2011: Assessment of multispectral glacier mapping methods and derivation of glacier area changes, 1978-2002, in the central Southern Alps, New Zealand, from ASTER satellite data, field survey and existing inventory data: *Journal of Glaciology*, v. 57, no. 204, 667 – 683.
- Hall, D.K., Foster, J.L., Verbyla, D.L., Klein, A.G., and Benson, C.S. 1998: Assessment of Snow-Cover Mapping Accuracy in a Variety of Vegetation-Cover Densities in Central Alaska: *Remote Sensing of Environment*, v. 66, 129-137.
- König, M., Winter, J.G., and Isaksson, E. 2001: Measuring snow and glacier ice properties from satellite: *Reviews of Geophysics*, v. 39, Issue 1, 1 – 27.
- Lillesand, T.M., Kiefer, R.W., and Chipman, J.W. 2008. Remote Sensing and Image Interpretation, 6th Ed. John Wiley & Sons, Inc., Hoboken, N.J.
- Paul, F. 2000: Evaluation of Different Methods for Glacier Mapping Using Landsat TM: *EARSeL eProceedings*, no. 1, 239 – 245.
- Rivera, A., Bown, F., Mella, R., Wendt, J., Casassa, G., Acuña, C., Rignot, E., Clavero, J., and Brock, B. 2006: Ice volumetric changes on active volcanoes in southern Chile: *Annals of Glaciology*, v.43, 111-122.
- Rivera, A., Benham, T., Casassa, G., Bamber, J., and Dowdeswell, J.A. 2007: Ice elevation and areal changes of glaciers from the Northern Patagonia Icefield, Chile: *Global and Planetary Change*, v. 59, Issues 1 – 4, 126 – 137.
- Schaefer, J. and Nye, C. 2008: The Alaska Volcano Observatory – 20 Years of Volcano Research, Monitoring, and Eruption Response: *Alaska GeoSurvey News*, v. 11, no. 1, 1 – 9.

- Shulski, M. and Wendler, G. 2007. *The Climate of Alaska*, University of Alaska Press, Fairbanks, A.K.
- Sidjak, R.W. and Wheate, R.D. 1999: Glacier mapping of the Illecillewaet icefield, British Columbia, Canada, using Landsat TM and digital elevation data: *International Journal of Remote Sensing*, v. 20, n. 2, 273 - 284.
- Waythomas, C.F., Miller, T.P., Mangan, M.T. 2006. Preliminary volcano hazard assessment for the Emmons Lake Volcanic Center, Alaska. United States Geological Survey Scientific Investigations Report 2006 – 5248, 33 p.
- Webley, P.W., Dehn, J., Lovick, J., Dean, K.G., Bailey, J.E., and Valcic, L. 2009: Near-real-time volcanic ash cloud detection: Experiences from the Alaska Volcano Observatory: *Journal of Volcanology and Geothermal Research*, v.186, Issues 1-2, 79-90.
- Werner, C.A., Doukas, M.P., and Kelly, P.J. 2011: Gas emissions from failed and actual eruptions from Cook Inlet Volcanoes, Alaska, 1989 – 2006: *Bulletin of Volcanology*, v. 73, 155 – 173.
- Wessels, R., Neal, C.A., Waythomas, C., Huggel, C., and Dean, K. 2007: Satellite measurement of glaciers on volcanoes in Alaska: Building an inventory of ice extent and hazards: *Abstract from the 103rd Annual Meeting of the Cordilleran Section of the Geological Society of America*
- Xiao, X., Shen, Z., and Qin, X. 2001: Assessing the potential of VEGETATION sensor data for mapping snow and ice cover: a Normalized Difference Snow and Ice Index: *International Journal of Remote Sensing*, v. 22, n. 13, 2479 - 2487.

Chapter 2 Methods for snow/ice cover mapping of Redoubt and Pavlof volcanoes using optical satellite imagery¹

Abstract

Over half of the historically active volcanoes in Alaska are covered by some quantity of perennial snow or glacial ice. Additionally, seasonal snow covers the flanks of all Alaskan volcanoes for at least half of the year. Although Alaskan glaciers have been studied in depth using a variety of methods, the mapping of snow/ice cover at Alaskan volcanoes has been limited. An effective method to map the snow/ice cover across a wide range of Alaskan volcanoes is needed in order to better quantify the snow/ice available for hazard generation during an eruption. Although ground-based methods of snow/ice cover mapping are ideal, the remote nature of most Alaskan volcanoes requires the use of satellite imagery. Two methods to map snow/ice cover on Alaskan volcanoes are examined in this study using a variety of optical satellite techniques such as band combinations, principal component analysis, and linear spectral unmixing analysis. Although limitations exist, the linear spectral unmixing method is more effective and efficient at mapping the snow/ice cover at remote Alaskan volcanoes.

2.1 Introduction

Monitoring Alaskan volcanoes presents a serious set of challenges, the most significant being the need to understand a wide range of volcanic behaviors as well as contend with highly variable environmental conditions. The majority of Alaskan

volcanoes are located along the 2,500 km long Aleutian Arc, within the Alaska Peninsula, and through Alaska's Cook Inlet, with more than 50 Alaskan volcanoes active historically, or approximately within the last 200 years (Schaefer and Nye, 2008). The expansive area over which Alaskan volcanoes can be found is both remote and sparsely populated, making monitoring of daily changes at a volcano challenging. Therefore, an effective approach to monitoring volcanism within Alaska is to focus on relative change by understanding the nature of each volcano during times of quiescence (Dean et al., 2002). This approach has been an effective way to monitor background levels of thermal output, ash/steam emissions, and seismic activity at Alaskan volcanoes so that periods of increased activity can be better understood (Dehn et al., 2000; Webley et al., 2009; Werner et al., 2011; Buurman et al., 2013). Now, the need to monitor background levels of snow/ice cover at Alaskan volcanoes in the same way has been recognized (Wessels et al., 2007).

2.1.1 Satellite remote sensing of glaciers and snow cover in Alaska

At least 30 of the Holocene-age volcanoes in Alaska are characterized by some level of glacier ice or perennial snow (Wessels et al., 2007), while seasonal snow covers most of the state of Alaska for at least six months out of the year (Shulski and Wendler, 2007). Initial efforts by the Alaska Volcano Observatory (AVO) to create a database of current snow/ice aerial extent on Alaskan volcanoes have included field work as well as analysis of satellite imagery, aerial photos, and historical maps (Wessels et al., 2007). Preliminary results from comparisons with historical imagery have shown that glaciers on

Alaskan volcanoes have decreased in extent over the last 30 – 50 years (Wessels et al., 2007). The glacial ice or snow on a volcano is subjected to changes in regional climate and precipitation. This trend of overall retreat is consistent with conclusions made for non-volcanic glaciers in Alaska. Arendt et al. (2002) estimated that the volume of ice lost at Alaskan glaciers from the mid-1990's through 2001 was nearly twice the volume lost from the Greenland Ice Sheet during this same period. Monitoring the net mass balance of glaciers in Alaska has been a major focus in the glaciological literature (see Bitz and Battisti, 1999; Arendt et al., 2002; Larsen et al., 2007; Berthier et al., 2010). The net mass balance is defined as the net change of the mass of a glacier at the end of the ablation season relative to the mass recorded the previous year. The net mass balance can vary greatly between maritime and continental or inland glaciers. The net mass balance of maritime glaciers is typically more influenced by precipitation during the winter season, while continental glaciers are more influenced by temperatures during the summer (Cuffey and Paterson, 2010). On top of these variations in maritime versus continental settings, previous work in Alaska has shown that even glaciers within the same 30 km radius may undergo different climate conditions (Arendt et al., 2002). An additional challenge to monitoring Alaskan glaciers over time is that, depending on glacier size and location, it may take up to 40 years for a glacial system to respond to a change in climate (Arendt et al., 2002). All of these challenges are then compounded when studying glaciers on volcanoes, where both climatological and volcanological influences can be relevant (Rivera et al., 2006).

2.1.2 Previous work and methods for studying snow/ice on volcanoes

The majority of studies relating snow/ice and volcanism center around periods of increased volcanic activity, such as how melt generation is influenced by increased thermal output or the deposition of volcanic products (Driedger, 1981; Pierson et al., 1990; Trabant and Hawkins, 1997; Smellie, 2006; Begét, 2010; Edwards et al., 2012; Bleick et al., 2013). The relationship between an active volcano and any overlying snow/ice cover can be broken up into two distinct parts: short-term and long-term interactions. Short-term interactions occur during an active volcanic eruption when volcanic products such as lava (Edwards et al., 2012) and pyroclastic flows (Begét, 2010) interact with underlying snow/ice. Much of the focus during an eruption has been on the formation of lahars, or volcanic mudflows, as a result of excessive meltwater generated during these short-term interactions (Pierson et al., 1990; Trabant et al., 1994). Examples of long-term interactions include the affect an ash cover has on the ablation rate of underlying snow/ice (Driedger, 1981) as well as the more gradual melting of overlying snow/ice due to increased thermal output from a volcano either before or after an eruption (Smellie, 2006; Bleick et al., 2013).

Rivera et al. (2006) report on a technique to study the change in glacial area and thickness between an active and dormant volcano over time. The two volcanoes chosen were Villarrica, an active volcano with more than 50 eruptive events in the past 450 years, and the dormant volcano Mocho (Rivera et al., 2006). Both of these volcanoes are located within a 60 km radius of each other in southern Chile and were chosen because they were estimated to be within a similar climate. While the glacial ice cover on both

volcanoes underwent a reduction in area, the glacial ice on Villarrica volcano had thinned to a greater extent between 1961 and 2004. Additionally, during specific times of increased volcanic activity, a larger number of crevasses were observed to form at the summit of the volcano (Rivera et al., 2006). Another aspect of the setting on Villarrica is that ash and other debris cover deposited on top of the glacial ice can help to thermally insulate the ice from ablation (Rivera et al., 2006). The insulating effect of debris cover on glacial ice has been seen at non-volcanic glaciers worldwide. The effect of debris cover, when mapping snow/ice extent using satellite imagery, has been shown to be a challenge by many researchers (Sidjak and Wheate, 1999; Boresjö Bronge and Bronge, 1999; Paul, 2000; Gjermundsen et al., 2011).

2.1.3 Challenges of mapping snow/ice cover at Alaskan volcanoes

The 1.7 million km² area of Alaska and, more specifically, the regions along which most volcanoes are found, represent a wide variety of climates (Bitz and Battisti, 1999; Arendt et al., 2002; Larsen et al., 2007). Without considering the volcanological influences, these different climate conditions prevent snow/ice cover observed at one volcano from being extrapolated to other volcanoes located in a different climatic region (see work in Arendt et al., 2002). For the purposes of this study another challenge, outside of differences in volcanism, is that glacial ice, perennial snow, and seasonal snow need to be mapped in order to identify the most relevant maps for hazard analysis (Trabant et al., 1994; Smellie, 2006; Wessels et al., 2007). Many previous efforts to map perennial snowfields and glaciers have focused on examining a single satellite image

acquired at the end of the ablation season, in August in the northern hemisphere and February in the southern hemisphere (Boresjö Bronge and Bronge, 1999; Sidjak and Wheate, 1999; Xiao et al., 2001). The purpose of using images acquired at the end of the ablation season is to remove the effect of extraneous seasonal snow. However, seasonal and perennial snow can also be contributors of melt water and resulting hazards during an eruption. For example, melting of the seasonal snowpack downstream from Redoubt volcano is estimated to have contributed contributed $35 \times 10^6 \text{ m}^3$ of meltwater during the 1989-1990 eruption (Trabant et al., 1994). Another challenge is found in the range of elevations characterizing Alaskan volcanoes. The elevation of a volcano or even a non-volcanic mountain helps determine whether the summit will be glaciated during the summer months or if it will be mostly snow and ice free. The two volcanoes we choose to study, Redoubt and Pavlof, have both similarities and differences that make them intriguing localities for snow/ice mapping. While both Redoubt and Pavlof (Figure 2.1) are stratovolcanoes with similar elevations that have erupted within the past 5 years, they vary in general setting, location, and eruptive styles (see Waythomas et al., 2006 for Pavlof; and Waythomas et al., 2013 for Redoubt).

2.2 Setting of Redoubt volcano

2.2.1 Basic setting of Redoubt volcano

Redoubt volcano (Figure 2.1A) is a stratovolcano which peaks at approximately 3,110 m above sea level (asl) and located on the Western coast of Cook Inlet,

approximately 175 km southwest of Anchorage, the largest city in Alaska. Located within the northeast end of the Aleutian Arc, Redoubt has mainly erupted products of an andesitic to dacitic composition and has had three major eruptions in the past 50 years: 1965-1968, 1989-1990, and most recently in 2009. Redoubt is covered by approximately 4 km³ of ice and perennial snow, with ice from the Drift glacier comprising 1 km³ of the total volume (Waythomas et al., 2013). Drift glacier begins within the northern rim of Redoubt's summit crater and flows to the north down a narrow canyon that ends in a piedmont lobe at an elevation of about 650 m asl (Figure 2.1B). At 300 m asl, the terminus of the piedmont lobe meets up with the head of the Drift River and Drift River valley (Trabant et al., 1994; Bleick et al., 2013). The Drift River then flows east, confined mostly within braided channels of the Drift River valley before entering a broader, tidal flat region within the coastal plain of Cook Inlet where a seven-tank oil storage facility, the Drift River Oil Terminal, is located.

2.3 Setting of Pavlof volcano

2.3.1 Basic setting of Pavlof volcano

Pavlof volcano (Figure 2.1A) is a basaltic stratovolcano approximately 2,518 m asl and, due to its high elevation, sustains a cover of snow/ice throughout the entire year. Pavlof is located within the Alaska Peninsula region of the state, approximately 965 km west of Anchorage, Alaska. Pavlof has erupted at least 40 times since 1790, making it the most historically active volcano in Alaska (Waythomas et al., 2006). The eruptions at

Pavlof have typically lasted from several days to a couple of months (McNutt, 1987). Pavlof is one of the six stratovolcanoes that comprise the Emmons Lake Volcanic Complex. The snow/ice cover on Pavlof has been described to a lesser degree formally than the snow/ice flanking Redoubt. Most researchers agree that a portion of Pavlof's flanks remain snow/ice covered year-round, however no suggested formal or informal names for the glacier(s) on Pavlof currently exist. The most extensive, field-based observations of the snow/ice cover on Pavlof were attempted in the 1940's and documented by Kennedy and Waldron (1955). This field study observed that a large proportion of volcanic ash was entrained in the glacier ice at Pavlof, leaving a thin layer of ash that covers much of the glacier when melt water redistributes it in the summer (Kennedy and Waldron, 1955). Waythomas et al. (2006) reported a similar observation of the area when estimating that up to 2 km³ of debris-covered glacial ice can be found along the flanks of Pavlof volcano (Figure 2.1C).

2.4 Methods

2.4.1 Previous work in snow/ice cover mapping using satellite imagery

Satellite imagery is a useful tool for mapping snow/ice cover, especially in remote areas where frequent field-based mapping may be challenging (König et al., 2001). Extensive work has been performed to complete glacier inventories such as the Global Land Ice Measurement from Space (GLIMS) project developed in 2005 (Raup et al., 2013) and the World Glacier Inventory (WGI), first conceived in the late 1950's with

further development into the World Glacier Inventory Extended Format (WGI-XF) (Cogley, 2010). GLIMS strives to obtain measurements on the estimated 160,000 glaciers present worldwide using satellite imagery, historical maps, and aerial photos (Raup et al., 2013). As of 2013, the GLIMS database has measurements on over 116,000 glaciers, including over 3,700 in Alaska (GLIMS and NSIDC, 2013). The WGI-XF currently has approximately 34% - 36% of the total glaciated area in Alaska mapped (Radić and Hock, 2010). However, glaciers within the Alaska Peninsula and Aleutian Islands chain have remained largely unmapped by both of these global inventories, with only a small percentage of Alaskan volcanoes along Cook Inlet included (Figure 2.2).

Many of the techniques used to map snow/ice cover with optical satellite imagery take advantage of the visible and near infrared (VNIR) through shortwave infrared (SWIR) spectral region of the electromagnetic spectrum, where wavelengths range from 0.4 to 3.0 μm (König et al., 2001). As reflectance varies with wavelength, the resulting reflectance versus wavelength relationships vary with surface type (König et al., 2001).

2.4.2 Sensors used for snow/ice cover mapping

In satellite remote sensing, there is a trade-off between high spatial resolution and high temporal resolution. Many global coverage maps of snow/ice used for daily monitoring purposes use lower spatial resolution sensors such as the Advanced Very High Resolution Radiometer (AVHRR) with an at nadir 1.1 km spatial resolution in visible channels or the Moderate-Resolution Imaging Spectroradiometer (MODIS) sensor with a 250 m - 500 m spatial resolution at visible wavelengths. The benefit of using these

two particular sensors is that they can provide daily images for much of the global surface (Dozier and Painter, 2004). However, higher spatial resolution (below 500 m) has been sacrificed for this daily access to data. While the use of MODIS or AVHRR may work effectively for large ice sheets such as those in Greenland, the data quality and understanding of surface structure at smaller snow/ice covered areas are lost as large areas are integrated into one pixel (König et al., 2001). In order to better study smaller scale snow/ice cover features, higher spatial resolution sensors can be used. We use three high spatial resolution sensors (Table 2.1). Access to daily imagery is not required for our study, as we are interested in mapping quiescent-phase snow/ice cover.

2.4.3 Pre-processing of satellite imagery

In total, 21 scenes were selected for each volcano. To pre-process each image, we first converted digital number (DN) values to spectral radiance and then to Top-of-Atmosphere (TOA) reflectance. We then applied a dark object subtraction to the data to remove any atmospheric effects from features such as haze or water vapor (Chavez, 1988). These pre-processing steps allow for normalization among images taken under different atmospheric conditions.

Bands with VNIR to SWIR wavelengths from the Landsat 5 Thematic Mapper (TM) and Landsat 7 ETM+ satellites were converted from digital number values to at-sensor spectral radiance by using Equation (2.1) (Chander et al., 2009):

$$L_{\text{radiance}} = ((L_{\text{max}\lambda} - L_{\text{min}\lambda}) / (Q_{\text{calmax}} - Q_{\text{calmin}})) \times (Q_{\text{cal}} - Q_{\text{calmin}}) + L_{\text{min}\lambda} \quad \textbf{Equation (2.1)}$$

Here, Q_{calmax} is the maximum quantized calibrated digital number value (usually 255 for Landsat), Q_{calmin} is the minimum quantized calibrated digital number value (usually 1 for Landsat), Q_{cal} is the input digital number of the pixel, $L_{radiance}$ is output spectral radiance of each pixel, $L_{max\lambda}$ is the spectral radiance scaled to Q_{calmax} , $L_{min\lambda}$ is the spectral radiance scaled to Q_{calmin} . Values for Q_{calmax} , Q_{calmin} , $L_{min\lambda}$, and $L_{max\lambda}$ were all obtained from the image metadata while Q_{cal} was input from pixels for each band (Variable designations from Chander et al., 2009).

Then, the at-sensor spectral radiance values were converted to TOA reflectance using Equation (2.2) (Chander et al., 2009):

$$R_{TOA} = (\pi \times L_{radiance} \times d^2) / (ESUN \times \cos(Z)) \quad \text{Equation (2.2)}$$

Where R_{TOA} is the output top-of-atmosphere reflectance for each pixel, $L_{radiance}$ is the input spectral radiance of each pixel value (found from Equation (1)), d is the Earth-Sun distance on the Julian Day the image was acquired, $ESUN$ is the mean solar exoatmospheric irradiance of each band (a constant dependent on sensor type and band number), Z is the solar zenith angle at the time of image acquisition, and \cos is cosine (Variable designations from Chander et al., 2009).

Finally, a dark object subtraction was performed using the method described by Chavez (1988). Although Chavez (1988) states that this method has its limitations and is simpler than other methods, it is a first-step approach to accounting for obvious atmospheric effects. This method uses a Region of Interest (ROI) within a dark object with low reflectance values, such as a body of water or a shadow, and assumes that it

should have a zero reflectance value. Any value above zero reflectance in the dark object ROI can then be assumed to be from unwanted atmospheric influences. The average reflectance value for the ROI is then subtracted from the reflectance value of each pixel in the image in order to remove the atmospheric effect. Finally, Landsat 7 ETM+ had a failure of the instrument's scan line corrector (SLC) that resulted in striping across images acquired after May 31, 2003. In our study, pixels within SLC-off stripes were masked and given a value of zero.

Pre-processing of ASTER data was performed by automatically converting ASTER DN values to radiance values by referencing the unit conversion coefficients reported for each band in the ASTER User Handbook (Abrams et al., 2004). Before further processing, the VNIR and SWIR bands were stacked together, with the SWIR bands resampled to the 15 m pixel size of the VNIR bands using Nearest Neighbor resampling (Abrams et al., 2004). After converting to radiance values, the VNIR/SWIR ASTER data set was converted to Top-of-Atmosphere reflectance using the appropriate wavelength values in Equation (2.2). Finally, the dark object subtraction technique was performed in order to remove atmospheric effects from the ASTER VNIR/SWIR data set (Chavez, 1988).

2.4.4 Methods used to map snow/ice cover at Redoubt and Pavlof

For the purposes of mapping snow/ice cover on Alaskan volcanoes in our study, we used the following three techniques: (1) band ratios; (2) principal component analysis; and (3) linear spectral unmixing. These three techniques will be divided into two different

methods. The first method uses a combination of band ratios, principal component analysis, and manual mapping where needed. The second method uses linear spectral unmixing. The steps to perform each of these three techniques will be given in the following section.

2.4.5 Technique 1: band ratios

For Landsat sensors, similar reflectance values in the visible bands (bands 1, 2, and 3) but different reflectance values in the mid-infrared (MIR) band 5 make it possible to characterize snow/ice cover by calculating a ratio of the bands (Dozier, 1989). Furthermore, differences in grain size are especially evident in the MIR band while difficult to see in visible bands (Dozier, 1989). These spectral differences between snow and ice have been used with success by the Normalized Difference Snow Index (NDSI), shown in Equation (2.3) (Dozier, 1989):

$$\text{NDSI} = (B2 - B5) / (B2 + B5) \quad \text{Equation (2.3)}$$

Where $B2$ is the at-ground reflectance pixel values in the green (visible) band and $B5$ is the at-ground reflectance pixel values in the MIR band in Landsat 5 TM and Landsat 7 ETM+.

A NDSI calculation can also be generated from ASTER imagery by taking a band ratio including the VNIR band 1 and SWIR band 4 (Equation 2.4) (Gjermundsen et al., 2011):

$$\text{NDSI} = (B1 - B4) / (B1 + B4) \quad \text{Equation (2.4)}$$

Where $B1$ is the at-ground reflectance pixel values in the VNIR band and $B4$ is the at-ground reflectance pixel values in the SWIR band in ASTER.

Additional band ratios can be used to further distinguish between variations in snow/ice cover. For example, Sidjak and Wheate (1999) found that taking the ratio between the at-ground reflectance pixel values in the near-infrared (NIR) and SWIR bands (a band 4/5 ratio for Landsat 5 TM and Landsat 7 ETM+) can define areas where ice is present versus snow. Boresjö Bronge and Bronge (1999) identified blue ice versus snow by using a ratio of the red and NIR bands (a band 3/4 ratio for Landsat 5 TM and Landsat 7 ETM+). A ratio of the red and SWIR bands can be used to enhance differences in grain size of snow, identifying fresh snow versus snow with varying levels of metamorphism (Boresjö Bronge and Bronge, 1999).

The choice for which band ratio to use depends on extraneous features in the image being analyzed. For example, Sidjak and Wheate (1999) contend that the red/NIR band ratio (using Landsat bands 4/5) provides the clearest delineation of ice versus snow in areas of shadow, while Boresjö Bronge and Bronge (1999) state that the Landsat bands 3/4 ratio is the best to use in areas of shadow or thin cloud cover. Gjermundsen et al. (2011) used a VNIR/SWIR band ratio with ASTER bands 3/4 (similar in reflectance properties to a Landsat 4/5 ratio). They found that this band ratio is the most efficient at discriminating between turbid lake water and snow/ice cover. One method used to remove extraneous features in an image, which can interfere with mapping efforts, is to subset the image so that it only includes the area covered by glacial ice or snow (Boresjö

Bronge and Bronge, 1999). We utilize this method in order to better map the snow/ice cover at Redoubt and Pavlof.

2.4.6 Technique 2: principal component analysis

In order to increase the variations between ground cover along the flanks of each volcano, a Principal Component Analysis (PCA) can be performed. PCA has been used in snow/ice cover mapping to enhance features of interest and to identify the features that may be mistaken for snow/ice cover, such as clouds and liquid water (Sidjak and Wheate, 1999; Boresjö Bronge and Bronge, 1999).

A Principal Component Analysis (PCA) breaks down the image into the main variations between bands and therefore decreases the number of existing correlations (Jolliffe, 2002). A PCA outputs the variations present within the original image as a stack of images, known as principal components (PCs). After a PCA, the dataset changes from a large, highly variable collection of data to a smaller set of PCs that represent the main variances within the image (Jolliffe, 2002). Each PC represents a greater amount of variance than the one after it. For instance, PC 1 has the greatest amount of variance while PC's 2, 3, 4, etc. represent decreasing amounts of variance. The last PC's that are created will then represent the smallest amount of variance and are largely noise (Jolliffe, 2002). For the purposes of snow/ice cover classification, PC's can be used to highlight a different feature such as areas of shadow and even variations in ground cover composition between different flow units (Sidjak and Wheate, 1999). More importantly, a PCA can discriminate between textures (Boresjö Bronge and Bronge, 1999). For

instance, although a volcano may be largely covered by a fresh layer of powdery snow, it is possible to distinguish underlying snow/ice cover textures using PC's (Sidjak and Wheate, 1999). The components from a PCA of the whole image may be dominated by features outside of the snow/ice cover (Boresjö Bronge and Bronge, 1999). However, if a PCA is completed solely for the subsetting area, features within the glacial ice or snow may be further enhanced. In essence, finer variances will be identified by the PCA when smaller areas are used as input (Sidjak and Wheate, 1999; Boresjö Bronge and Bronge, 1999).

In our study, a PCA was performed for each image with inputs from both a larger area, including features outside of the snow/ice cover, and from smaller subsets of only the snow/ice covered area. As Sidjak and Wheate (1999) state, the thermal band(s) do not provide much information on the snow/ice cover surface, and therefore only the visible, NIR, MIR, and SWIR bands were used for each image.

2.4.7 Technique 3: linear spectral unmixing

One of the significant challenges of accurately mapping what is on the ground surface from satellite imagery is that the reflectance spectra of each pixel is actually a mixture of the reflectances of individual surfaces within the pixel area (König et al., 2001). The greater the area of the pixel, the more likely it is that there will be mixed surfaces integrated across that pixel (König et al., 2001). Therefore, it is important to select a sensor with a spatial resolution that is compatible to the chosen study area. For instance, the low spatial resolution of the MODIS and AVHRR sensors would not be able

to accurately map the snow/ice cover variations on a volcano. Such features are much smaller than the large glaciers and ice sheets these instruments are typically used to study (König et al., 2001). This is compounded by the fact that a pixel composed primarily of ice from a large ice sheet will be much less spectrally mixed than the same sized pixel on a volcano containing a mix of snow, rock, and vegetation (König et al., 2001).

The main goal in performing a linear spectral unmixing analysis is to examine what the ground cover is at the subpixel scale. In order to do this, a couple of assumptions must be made. The first assumption is that the spectral signature of a pixel is actually a linear combination of multiple ground surfaces within the pixel area. Secondly, it's assumed that the reflectance of each ground cover type within the pixel is spectrally distinct from the other ground cover types (Dozier and Painter, 2004). Each distinct ground cover spectrum is characterized as an "endmember". In order to identify the endmembers within an image, the pixels with the purest spectrum for each ground cover type are selected.

To reduce the variability of the data to a few bands, a PCA is performed on the image. As the majority of the variability is found within the first two PCs, a 2-dimensional scatter plot is then generated with PC1 as the independent variable and PC2 as the dependent variable (Van Der Meer and De Jong, 2000). Van Der Meer and De Jong (2000) show that the spectra of the endmembers are the vertices of the polygon created by the PC1 versus PC2 scatter plot. The contribution of each endmember to the spectral reflectance of the entire pixel is then solved for by using a set of simultaneous linear equations for each band wavelength (König et al., 2001). The output data from a

linear spectral unmixing analysis is a set of images that correspond to each chosen endmember. The pixel values in each endmember image range from 0 to 1, and correspond to the percentage of the pixel containing that endmember. For example, if snow/ice is chosen as an endmember, a pixel with a value of 0.60 within the snow/ice endmember image will have an area that is composed of 60% snow/ice cover. Along with the endmember images, an additional band with root mean square (RMS) errors is calculated so that the maximum, mean, and minimum errors for the analysis can be computed.

2.5 Results and discussion

Snow/ice cover maps were made for 21 images over the area of each volcano. Two snow/ice cover maps were generated for each individual image over the same spatial area for each volcano to test the effectiveness of different mapping methods. A locality map of the Redoubt study area is shown in Figure 2.3 and the Pavlof study area is shown in Figure 2.4. The first type of map, hereafter referred to as a threshold map, uses a combination of two techniques: band ratios and PCA, with manual mapping of snow/ice pixels where needed. The second type of map uses only the linear spectral analysis technique.

2.5.1 Snow/ice cover mapping using threshold method

The first set of snow/ice cover maps produced for both Pavlof and Redoubt volcanoes use a mixture of band ratios and PCA in order to correctly identify the greatest portion of snow/ice through pixel value thresholding (Table 2.2 and Table 2.3). The images we use for each volcano span from the local Alaskan late spring to early fall, approximately May through September, in order to focus mapping efforts on the period of time when snow/ice cover approaches its annual minimum and where the distinction between seasonal snow, perennial snow, and glacial ice can be approximated. The images we analyze represent a diversity of physical conditions from variations in cloud cover to the possibility of liquid water in stream or river beds to the changing influences of shadow. The presence of diverse physical conditions within an image requires variations of the thresholding method necessary to map snow/ice cover as some techniques are more heavily influenced by certain physical conditions (Sidjak and Wheate, 1999; Xiao et al., 2001). Despite attempting to combine mapping techniques to best distinguish the snow/ice cover from other land cover, it isn't always possible to encompass all snow/ice pixels into one simple threshold of values.

In instances where the snow/ice cover cannot be sufficiently mapped using a threshold of values from a PCA or band ratio analysis, the remaining snow/ice pixels are identified visually and manually mapped. This is necessary for images of both the Redoubt and Pavlof study areas, although the use of smaller subsets decreases the need for manual mapping of images for Redoubt (Figures 2.5 and 2.6). Figures 2.7 – 2.11

include select images that represent the techniques we use to overcome challenges in mapping snow/ice cover at Redoubt and Pavlof volcanoes using the threshold method.

Liquid water can result in high NDSI values, resulting in possible misclassification as snow/ice (Klein and Barnett, 2003). For instance, because the selected images were acquired during the Alaskan summer months when melt generation is at a maximum, the varying presence of liquid water had a significant influence on mapping efforts. The presence of liquid water was especially prevalent within the Drift River valley at the base of Redoubt volcano (Figure 2.7A). Figure 2.7B shows the influence of the liquid Drift River on the NDSI band ratio values in a Landsat 5 TM image from June 29, 2006.

The presence of liquid water within the river valley has resulted in high NDSI values in the lower reaches of the Drift River, erroneously characterizing these river water pixels as snow/ice. Kulkarni et al. (2002) and Klein and Barnett (2003) have shown that improvements to snow/ice identification using the NDSI band ratio is possible by masking out water pixels using the NIR band, where water has a reflectance much lower than snow and ice.

We apply a simpler solution for the Redoubt image from June 29, 2006. Based on visual interpretation of the natural color image (Figure 2.7A), the spatial extent of the snow/ice within the Drift River valley appears to be confined to the Drift Glacier lobe as discontinuous patches of exposed snow/ice (Figure 2.8A). This allows for further subsetting of the image to the Drift Glacier lobe area (Figure 2.8B) in order to completely remove the influence of the Drift River. Most images between May and September for

Redoubt volcano required subsetting to include only the Drift Glacier and can be identified by the “lobe only” designation in Table 2.2.

The NDSI image of the Drift Glacier lobe (Figure 2.8C) demonstrates another difficulty with using the NDSI band ratio to map snow/ice cover. Dark targets, such as shadows from high elevation or clouds, can also cause high NDSI values that approach snow/ice values (Klein and Barnett, 2003). The yellow-outlined areas in Figure 2.8B identify three shadows created by clouds within the image. The NDSI band ratio of this image (Figure 2.8C) results in low values for clouds within the area, while mapping the cloud shadows with high NDSI values, characterizing them as snow/ice. In order to eliminate this problem, the NDSI image is multiplied by the Band 1 reflectance image (Figure 2.8D) in order to utilize the high reflectance of snow/ice and low reflectance of shadows in Band 1, while taking advantage of the low NDSI values for clouds. Figure 2.8D is then used as the input for the threshold to produce a snow/ice map (Figure 2.8E).

As Tables 2.2 and 2.3 demonstrate, combining multiple techniques is a common method we employ to produce thresholdable images to map snow/ice cover for both the Redoubt and Pavlof study areas. Figure 2.9 demonstrates an analysis of the Pavlof study area, where a combination of mapping techniques resulted in an image that was easier to threshold for snow/ice pixels.

As the first component of the PCA, Figure 2.9A represents the highest variance of the scene. Both the snow/ice cover and cloud cover within this image are characterized by bright white pixels, making it difficult to reliably distinguish between these two features. The NDSI image, in Figure 2.9B, corrects this issue by mapping snow/ice with

high pixel values and clouds as dark grey in color with low pixel values. However, the NDSI band ratio also results in high pixel values along the coastline with Pavlof Bay (Figures 2.9B and 2.9C). Using the second principal component produces low pixel values for clouds (Figure 2.9C). However, both the water in Pavlof Bay and the SLC-off stripes are assigned mid-to-high pixel values, decreasing the separation between snow/ice pixel values and background values. By combining the first and second principal components (Figure 2.9D), the resulting image decreases the pixel values of clouds, SLC-off stripes, and water while highlighting snow/ice with high pixel values.

Unlike Redoubt, the Pavlof study area is not analyzed as smaller spatial subsets but instead as one large area that includes Pavlof volcano, Pavlof Sister volcano, and the northern rim of the Emmons Lake volcanic complex. The use of this larger rectangular area for all the Pavlof study area images results in a larger proportion of snow/ice cover maps requiring manual delineation as well as thresholding (Figure 2.6).

Figure 2.10A is a Landsat 5 TM image from May 16, 2009 showing the Pavlof study area under haze cover. The PCA is heavily influenced by this haze, resulting in low pixel values for the snow/ice cover in the first principal component (Figure 2.10B). By taking advantage of this distinct characterization of the snow/ice in PC1, a threshold can be used to create a ROI that encompasses the largest amount of snow/ice pixels (Figure 2.10C). However, based on visual interpretation, a large proportion of snow/ice pixels remain unmapped using a threshold alone. In order to complete the map, manual delineation of the remaining snow/ice pixels is performed with approximately 24% of the total snow/ice pixels for this image mapped in this way (Figure 2.10D).

2.5.2 Snow/ice cover mapping using linear spectral unmixing method

The second set of snow/ice cover maps for each image was produced using the linear spectral unmixing method. The same Redoubt and Pavlof study areas were used as input in order to compare the effectiveness of the two mapping methods. The first step is to select the appropriate endmembers from a graph of the PC1 versus PC2 scatter plot, demonstrated by Figure 2.11.

The specificity to which endmembers may be mapped depends on the spectral resolution of the sensor used. Hyperspectral sensors, such as Hyperion on the Earth Observing 1 satellite, have many bands that each cover a small range of wavelengths and thus are able to easily discriminate between finer variations in spectral signature such as differences in rock type or grain size and water content of snow (Cloutis, 1996). Multispectral sensors, like Landsat 5 TM and Landsat 7 ETM+ have a coarser spectral resolution, so endmembers must be grouped into broader spectral categories (Dozier and Painter, 2004). Based on visual interpretation, the Landsat 5 TM image of the Pavlof study area from May 16, 2009 (Figure 2.11A) can be broken down into three broad spectral endmembers: snow/ice, bare rock, and liquid water in Pavlof Bay (Figure 2.11B). These three endmembers are confirmed by the two-dimensional plot of the first and second principal components, where three distinct vertices can be identified (Figure 2.11C). Each vertex in the PC1 versus PC2 graph represents a different spectral class.

After endmember selection, the resulting regions of interest are used as input for a linear spectral unmixing analysis. The output is a pixel percentage map for the snow/ice endmember (Figure 2.12A), rock endmember (Figure 2.12B), and water endmember

(Figure 2.12C) along with a root mean square error image (Figure 2.12D). If mapping of the whole scene was required, better discrimination would be needed in order to identify the flow deposits surrounding Pavlof and Pavlof Sister volcanoes as a separate endmember. This would help to spectrally distinguish these flow deposits from the water in Pavlof Bay (Figure 2.12C). Snow/ice was mapped using a threshold value of pixel percentages. The map created in Figure 2.12E includes all pixels that contain at least 30% snow/ice. Inclusion of pixels that contain less than this percentage of snow/ice would result in the mapping of superfluous background pixels. Just as with the thresholding technique used to create the snow/ice map for this image in Figure 2.10, a cover of indiscrete haze creates challenges for the linear spectral unmixing analysis. Unmapped areas of snow/ice can be seen as whitish-grey features along the periphery of the mapped snow/ice region in Figure 2.12E. This area of unmapped snow/ice is the same area that required manual mapping in Figure 2.10D.

If there is discrete cloud cover within an image, it can be identified as an endmember vertex in the PC1 versus PC2 scatter plot. A Landsat 7 ETM+ image of the Pavlof study area from June 17, 2012 demonstrates how cloud cover can be included as an endmember in linear spectral unmixing. The natural color image of this scene shows partially-distinguishable cloud cover. However, cloud cover becomes indistinguishable when it overlaps areas of snow/ice (Figure 2.13A). The following endmembers: rock type one (previous flow deposits), rock type two, snow/ice, and cloud cover (Figure 2.13B) are identified as vertices in the PC1 versus PC2 scatter plot (Figure 2.13C). The snow/ice cover pixel percentage image (Figure 2.14A) is used as the input to map the pixels

composed of at least 25% snow/ice (Figure 2.14B). Small regions of unmapped snow/ice cover pixels can be seen adjacent to the mapped region. However, when comparing the threshold/manual map with the map created using linear spectral unmixing (Figure 2.14C), it is apparent that linear spectral unmixing identifies a larger area of snow/ice. Despite the results observed in this June 17 image, the linear spectral unmixing method does not consistently map a smaller or greater snow/ice area than that mapped by the threshold method across the entire set of images at the Pavlof study area. With a quantitative comparison of the resulting snow/ice areas mapped by the threshold versus linear spectral unmixing methods for each image of the Pavlof subset, the percent difference between methods ranges from 0.4 – 41.8% for the 21 images studied, with the average percent difference as approximately 17.9% (Figure 2.15).

Linear spectral unmixing is also used to map snow/ice cover at Redoubt volcano. Similar problems exist in discriminating between liquid water, within the Drift River valley, and snow/ice. Figure 2.16 is an analysis of a Landsat 5 TM image from June 29, 2006 of the Drift Glacier lobe subset. The threshold mapping analysis of this image was shown in Figure 2.8, where misidentification of cloud shadows as snow/ice occurred in the NDSI image. Figures 2.16A - C are the three pixel percentage images resulting from endmember selection in the PC1 versus PC2 scatter plot: snow/ice (Figure 2.16A), cloud cover (Figure 2.16B), and cloud shadow (Figure 2.16C) with the RMS error image (Figure 2.16D). Unlike with the threshold mapping technique, the cloud shadows are able to be mapped effectively using linear spectral unmixing analysis. This allows the snow/ice cover to be mapped without interference from cloud shadow (Figure 2.16E) and

to a similar extent as the [Reflectance Band *NDSI] threshold image (Figure 2.16F). Similar to the results observed in the Pavlof study area, the linear spectral unmixing method does not consistently map a smaller or greater snow/ice area than that mapped by the threshold method across the entire set of images at the Redoubt study area. However, the two different methods produced snow/ice maps for the Redoubt area that varied greater than those produced for the Pavlof study area. The percent differences between the snow/ice areas mapped by each method range from 0.9 – 116.0% for the 21 images and the average percent difference across the whole dataset is approximately 25.7% (Figure 2.17). The largest difference between the areas mapped by the two methods occurs in the Landsat 5 TM image from August 30, 2008. This could be due to a cover of thin clouds over a large proportion of the volcano's flanks. In the threshold method used to map this image, the first and second principal components are multiplied together to enhance the snow/ice above background values (Table 2.2). While this method effectively maps the snow/ice that is not under a cover of thin clouds, a large area of snow/ice under cloud cover is not included in the snow/ice total. Better discrimination between land cover types is achieved with the linear spectral unmixing method by defining clouds and snow/ice as separate endmembers. This permits more snow/ice to be mapped beneath thin cloud cover, resulting in a greater area of snow/ice than that mapped by the threshold method. If the anomalously high percent difference between the two methods in this August 30 image are removed, the average percent difference between the methods for the Redoubt study area becomes approximately 21.2%. More analysis is needed to determine why the two methods produce greater variances in the resulting

snow/ice maps for the Redoubt than the Pavlof study areas. However, it is likely that the smaller overall size of the Redoubt study area, as well as the usage of smaller subsetting regions, results in there being a greater overall effect of how sensitive each method is to influences such as shadow and cloud cover.

2.5.3 Improvements to linear spectral unmixing method for snow/ice cover mapping

One of the main issues with using the PC1 versus PC2 scatter plot to identify spectral endmembers is that the vertex for spectrally pure snow/ice, for instance, changes dependent on the viewing window utilized to make the endmember selection. For instance, if the viewing window is held over a region of snow/ice in shadow, the spectrally pure pixels will be chosen within that region rather than within the whole image. Snow/ice pixels may exist within the image that are more spectrally pure than those chosen as the snow/ice endmember using the PC1 versus PC2 scatter plot (EXELIS, 2014). Pixels that are more spectrally pure than the chosen endmember pixels will have a snow/ice value of over 1 (equivalent to a pixel percentage of over 100%) in the linear spectral unmixing output image (EXELIS, 2014). The number of pixels with a value over 1 varied from under 100 to over 100,000 pixels in the images analyzed (Tables 2.4 and 2.5).

In order to decrease the number of snow/ice pixels with a value over 1, the most spectrally pure pixels need to be chosen as the snow/ice endmember. Determining which pixels are the most spectrally pure requires examination of the output from the first analysis with linear spectral unmixing, referred to as “iteration one”. If a value over 1

relates to a pixel that is more spectrally pure than the chosen endmember, the snow/ice pixels with the highest values over 1 in the spectral unmixing image should therefore represent the most spectrally pure pixels. The approximately 100 highest valued pixels in the iteration one output image were then chosen as the snow/ice endmember to be input into a second linear spectral unmixing iteration (iteration two) along with the original additional scene endmembers (such as rock, water, or cloud cover).

Examples of these iterations are shown in Figures 2.18 and 2.19. In iteration one (Figure 2.18A), the spectrally pure pixels representing the snow/ice endmember are chosen as one of the vertices in the PC1 versus PC2 scatter plot (Figure 2.18B). The viewing window is positioned towards the tidal flat region along the coast of Cook Inlet, resulting in an endmember based on snow/ice within the lower reaches of the Drift River valley (Figure 2.18A). The linear spectral unmixing output effectively maps the snow/ice but with a large proportion (116,296 pixels) of pixels with a value over 1 (Figure 2.18C). This output image is then used to locate the group of snow/ice pixels with the highest pixel percentage value (Figure 2.19A).

The highest percentage values range from 1.175 to 1.190 and include 115 pixels (Figure 2.19A insert). These 115 pixels are then input as an endmember along with the other two original endmembers (rock and water) in the linear spectral unmixing algorithm. The output image from this second iteration has a total of 49 pixels with a value over 1 (Figure 2.19B), all centered along the southeasterly-facing flank of the volcano (Figure 2.19B insert). Although this multi-iteration method vastly improves the amount of snow/ice pixels with a value above 1, the resulting second iteration image has

a higher RMS error than the first iteration image (see Table 2.4), though still within the same magnitude as those errors recorded by Van Der Meer and De Jong (2000).

As can be seen in the color mapping of Figure 2.18C and Figure 2.19B, the pixel percentage values vary widely across the image with the highest values centered along the highly illuminated southeastern ridge, suggesting that variations in illumination and shadow may have a strong influence on pixel spectra. Although the effect of illumination on the image was taken into account during pre-processing, this may not have been enough to completely remove the influence of variations in illumination on sub-pixel spectral signals (Foppa et al., 2002). Foppa et al. (2002) removed these effects by adding an endmember that represents areas of low reflectance in order to account for shadow (Foppa et al., 2002). In this study, we map shadow-on-snow/ice pixels where the need for such an endmember is determined from the vertices of the PC1 versus PC2 scatter plot. For instance, Figure 2.20 is a Landsat 7 ETM+ image of the Redoubt volcano subset from May 13, 2006 that is heavily affected by snow under shadow.

Small regions of shadow on snow/ice occur in the natural color image (Figure 2.20A) caused by the topographic highs throughout the volcano's flanks, particularly to the north. The linear spectral unmixing output of the snow/ice endmember (Figure 2.20B), shows high pixel percentage values along the highly reflective south-facing summit ridge with low snow/ice percentage values along the lower reaches of the volcano. The resulting snow/ice map reveals an underestimation of the snow/ice pixels at the volcano's base (Figure 2.20C). However, when both the snow/ice and shadow (Figure 2.20D) output images are combined using a 50% threshold of both endmembers, the

resulting map (Figure 2.20E) more effectively represents the snow/ice pixels seen visually in the natural color image. This could be an effective way to map the snow/ice cover in images, where shadow is a large enough factor to be included as an endmember vertex in the PC1 versus PC2 scatter plot.

A large percentage of shadow in an image also affects the number of iterations required to reduce the amount of pixels with percentages over 100%. In certain Redoubt study area images, particularly those later in the season where shadows are longer with a lower solar zenith angle, a total of three iterations are required to achieve less than 100 pixels with a value over 1 (Table 2.4). It is unclear why three iterations are needed for the two Pavlof images from July 8, 2005 and June 4, 2007 (Table 2.5). However, the second iterations for both of these images each contain only 161 – 166 pixels with percentage values over 1, similar to the second iteration for the Redoubt image from June 4, 2000. The highly shadowed fall and winter images for Redoubt from September and March have well over 1,000 pixels with a value greater than 1 in the second iteration image.

2.5.4 Validation of results

While ground control observations are currently unavailable, we validate how well the linear spectral analysis method performs using higher spatial resolution imagery (Foppa et al., 2002). Figure 2.21A shows a Landsat 7 ETM+ image from October 20, 2006 used to validate the linear spectral unmixing method of snow/ice cover mapping against an IKONOS image from November 17, 2006 (Figure 2.21B). IKONOS is a commercial satellite operated by GeoEye © since 1999 (Dial et al., 2003). The IKONOS

image used has 3 visible bands and 1 near-infrared band that were resampled from a 4 m to a 1 m spatial resolution. Although the Landsat and IKONOS images were acquired approximately one month apart, the lack of snow in the lower river valleys within both images suggests significant seasonal snowfall did not occur between the two image dates (Figures 2.21A and 2.21B).

A linear spectral unmixing analysis is performed on the Landsat validation subset image (Figure 2.21B) and we use a 50% pixel percentage threshold to map the snow/ice cover (Figure 2.21C). The same area is used as the IKONOS validation subset (Figure 2.21D) and the visible snow/ice is mapped taking advantage of the 1 m spatial resolution (Figure 2.21E). A total area of 12.208 km² of snow/ice is mapped using the linear spectral unmixing method with the Landsat validation subset while a 12.487 km² snow/ice area is mapped using a threshold on the first band of the IKONOS image. Although the validation subset area used is smaller than the images used throughout this study, the snow/ice map created using linear spectral unmixing is reasonably validated by the higher spatial resolution IKONOS imagery. The snow/ice mapped using the linear spectral unmixing method with the Landsat image has a relative error of only 2.2% compared to that mapped in the IKONOS image, the best approximation for what is actually on the ground surface.

2.6 Conclusion

The goal of this study is to compare two methods of mapping snow/ice cover on Redoubt and Pavlof volcanoes that utilize three different techniques. The first method uses different combinations of band ratios, principal component analysis, and manual mapping where needed. The second method uses only linear spectral unmixing. The snow/ice cover maps created for both study areas result in an approximately 17.9% difference between the threshold method and linear spectral unmixing method for the Pavlof study area and an approximately 25.7% difference for the Redoubt study area. The Pavlof study area generally requires more manual delineation of snow/ice pixels when using the threshold method, as the larger area makes it difficult to include all visible snow/ice within one threshold of values. Breaking the Redoubt study area into three smaller subsets required less manual mapping by removing unwanted features such as liquid water within the lower reaches of the Drift River valley. However, a smaller analysis area also meant that a greater percentage of the total pixels were influenced by shadow. Mapping snow/ice under extreme illumination levels remains a challenge for both the threshold and linear spectral unmixing methods. The most spectrally pure snow/ice pixel endmembers in all images tend to be spatially located along the areas of greatest sun reflectance, particularly along south-facing ridges. Variations in pixel percentage values within a spectral unmixing output image are then largely influenced by these highly illuminated pixels. The influences of shadow are also prominent and can be seen especially within images acquired at a lower sun zenith angle. In these images, a

greater number of spectral unmixing iterations are required to delineate the purest snow/ice endmember pixels.

Although challenges still remain when using linear spectral unmixing to map snow/ice cover at Alaskan volcanoes, the amount of user time and input is generally less than that required by the threshold method. Linear spectral unmixing of a Landsat image also produced a snow/ice area with a relative error of only 2.2% from that mapped using a 1 m spatial resolution image, helping to validate the technique despite a lack of ground control points. Future ground referencing is needed to address the issue of debris covered snow/ice, a feature that can only be approximated by satellite-based mapping methods. However, linear spectral unmixing is a good first-approximation technique to map snow/ice cover at small, remote Alaskan volcanoes.

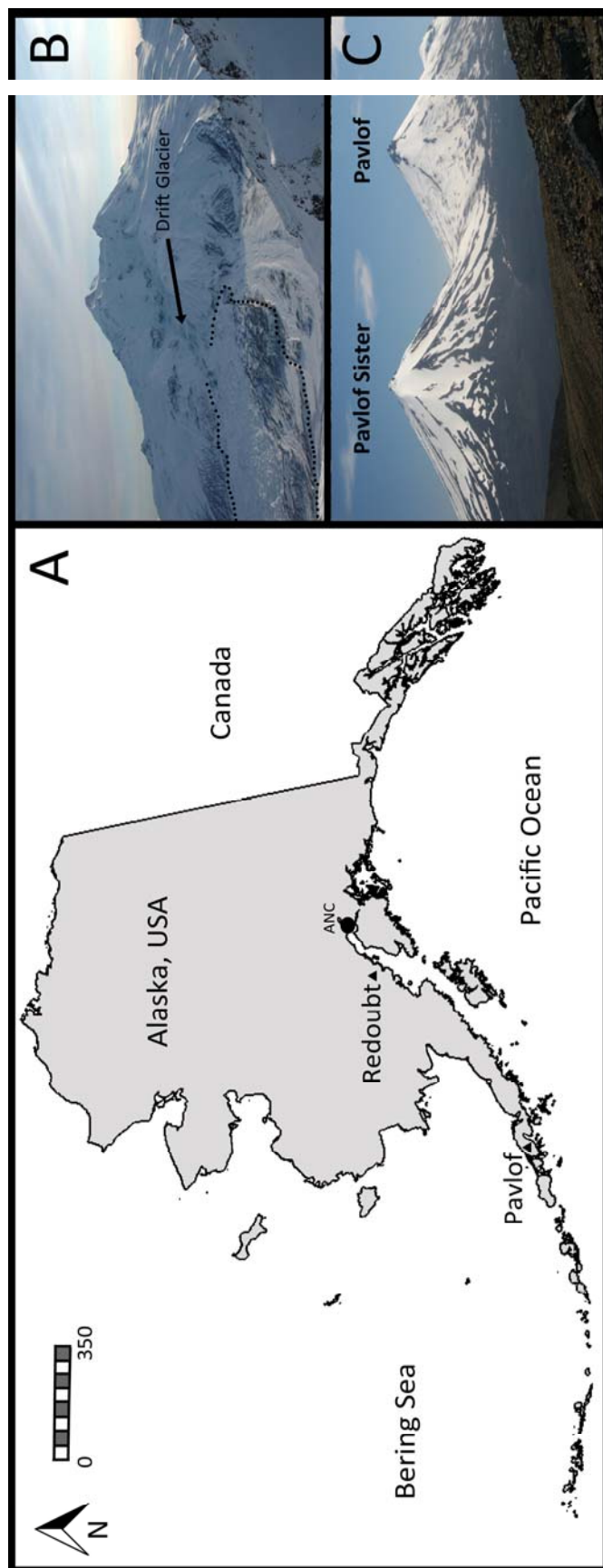


Figure 2.1. Introduction to Redoubt and Pavlof volcanoes. (A) Location map of Redoubt and Pavlof volcanoes within Alaska. Note the location of Anchorage, Alaska (ANC) at the circle shape. (B) Photograph of Redoubt volcano courtesy of G. McGimsey (United States Geological Survey Alaska Volcano Observatory) with the Drift Glacier piedmont lobe outlined with black dotted line. (C) Photograph of Pavlof and Pavlof Sister volcanoes courtesy of C. Waythomas (United States Geological Survey Alaska Volcano Observatory). Base outline of Alaska courtesy of the Alaska Volcano Observatory and the United States Geological Survey.

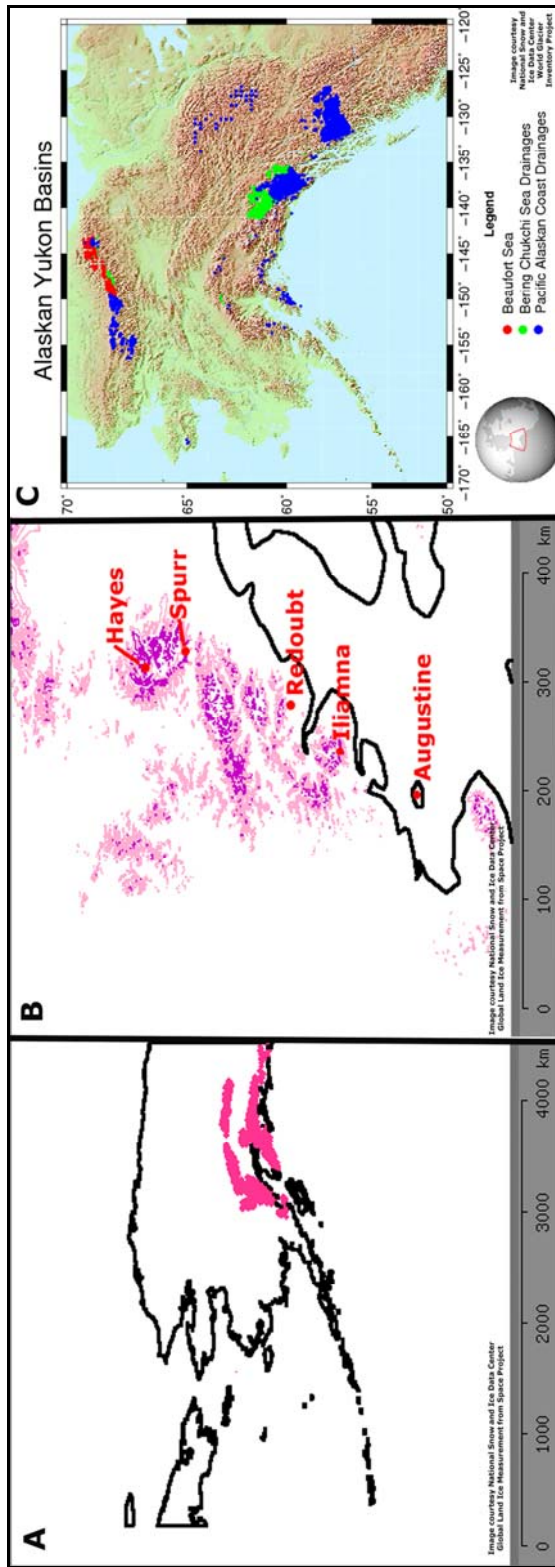


Figure 2.2. Alaskan glaciers mapped by GLIMS and World Glacier Inventory. (A) Alaskan glaciers mapped by GLIMS (in pink), (B) Glaciers mapped by GLIMS in relation to historically active Cook Inlet volcanoes (noted in red). Glacier elevations shown with low elevations in pink and high elevations in dark purple, (C) Alaskan glaciers mapped in World Glacier Inventory.

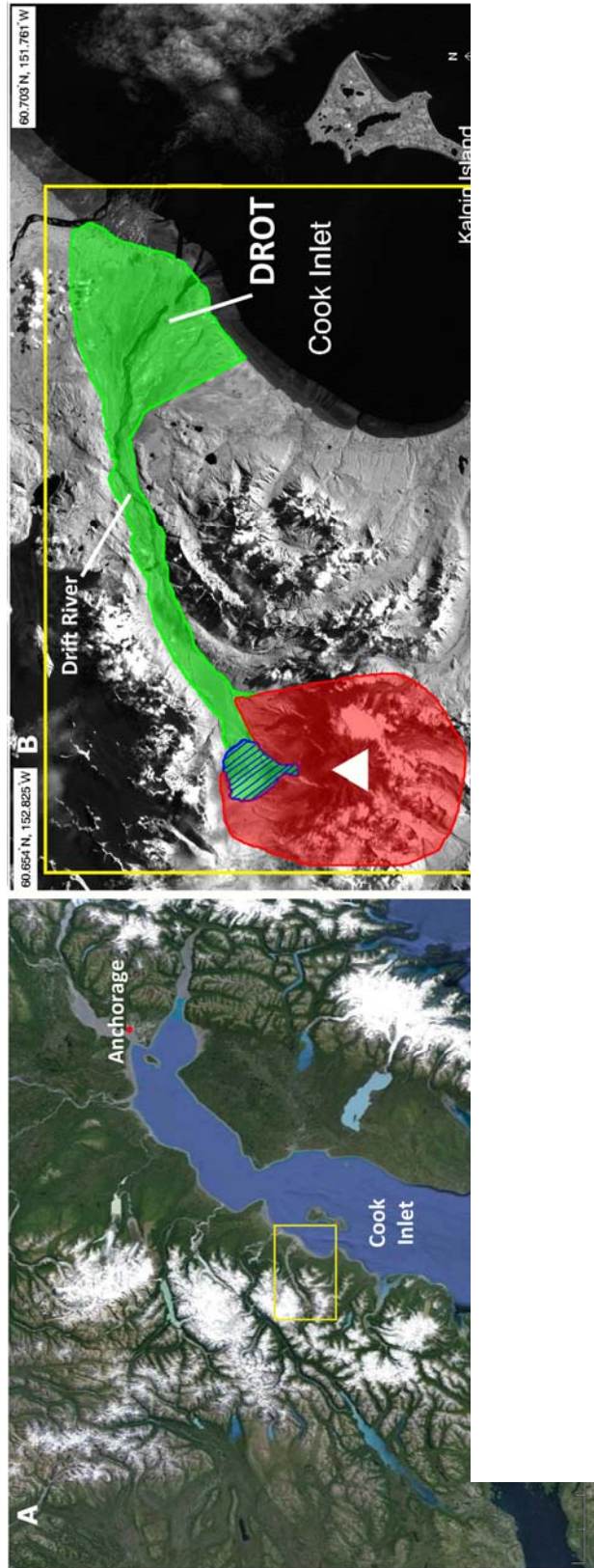


Figure 2.3. Location of Redoubt study area used for analysis. (A) Location of Redoubt study area (outlined in yellow) in relation to larger Cook Inlet region (image modified from Google Earth™) and (B) Closer view of Redoubt study area (outlined in yellow). Images used to analyze study area were broken into three different subsets: a volcano subset (in red), a glacier lobe subset (blue-hatched area), and a Drift River valley subset (in green).

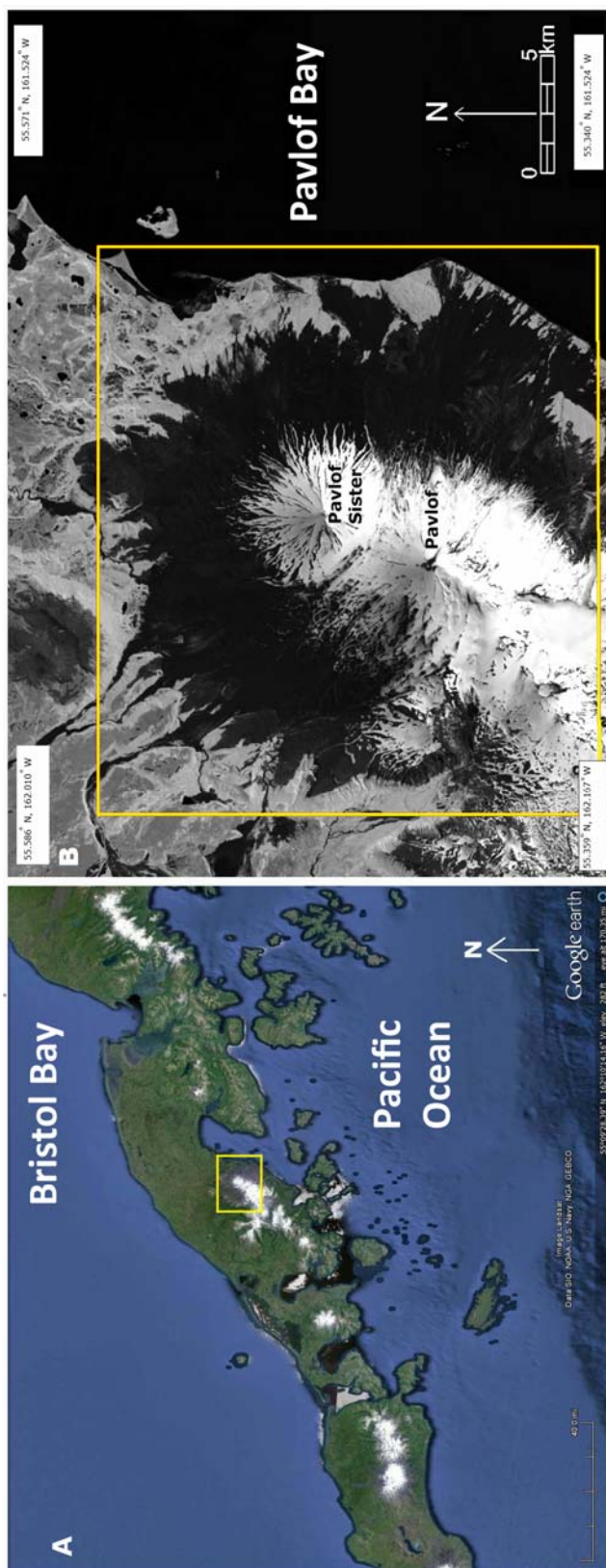


Figure 2.4. Location of Pavlof study area used for analysis. (A) Location of Pavlof study area (outlined in yellow) in relation to larger Aleutian arc (image modified from Google Earth™) and (B) Closer view of Pavlof study area (outlined in yellow) within the Pavlof Bay area. Note: Study area will be referred to as “Pavlof study area” despite encompassing both Pavlof and Pavlof Sister volcanoes.

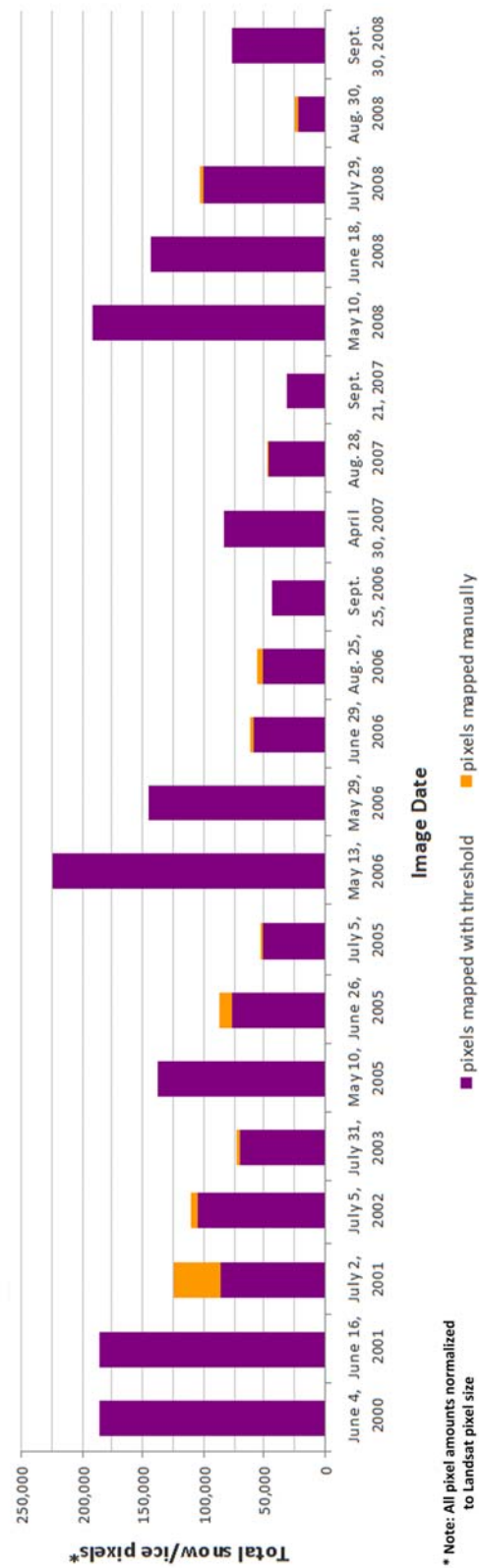


Figure 2.5. Snow/ice pixels mapped in Redoubt subset using threshold method. Total number of snow/ice pixels mapped using value threshold (in purple) and supplemented with manual delineation (in yellow) when necessary for Redoubt study area.

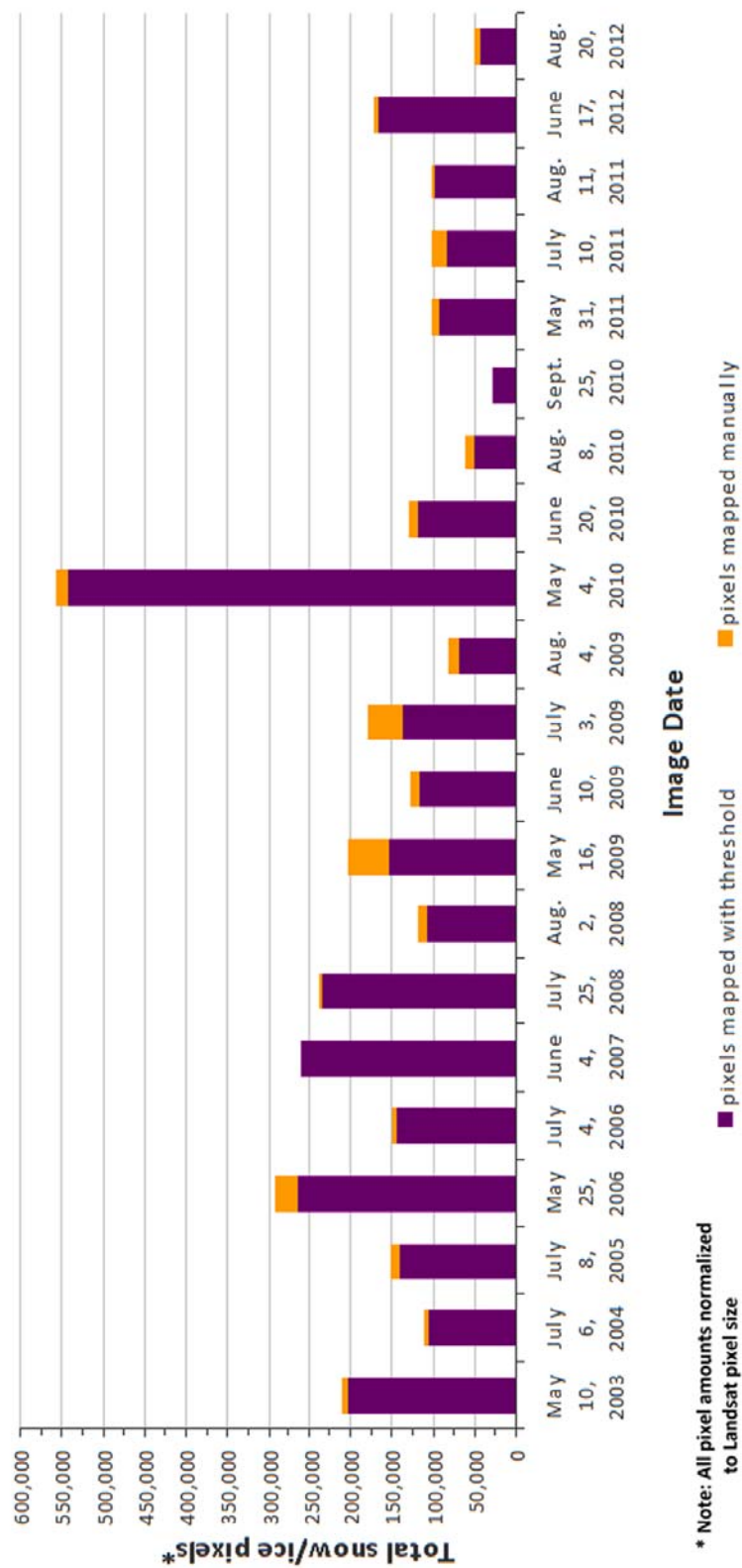


Figure 2.6. Snow/ice pixels mapped in Pavlof subset using threshold method. Total number of snow/ice pixels mapped using value threshold (in purple) and supplemented with manual delineation (in yellow) when necessary for Pavlof study area.

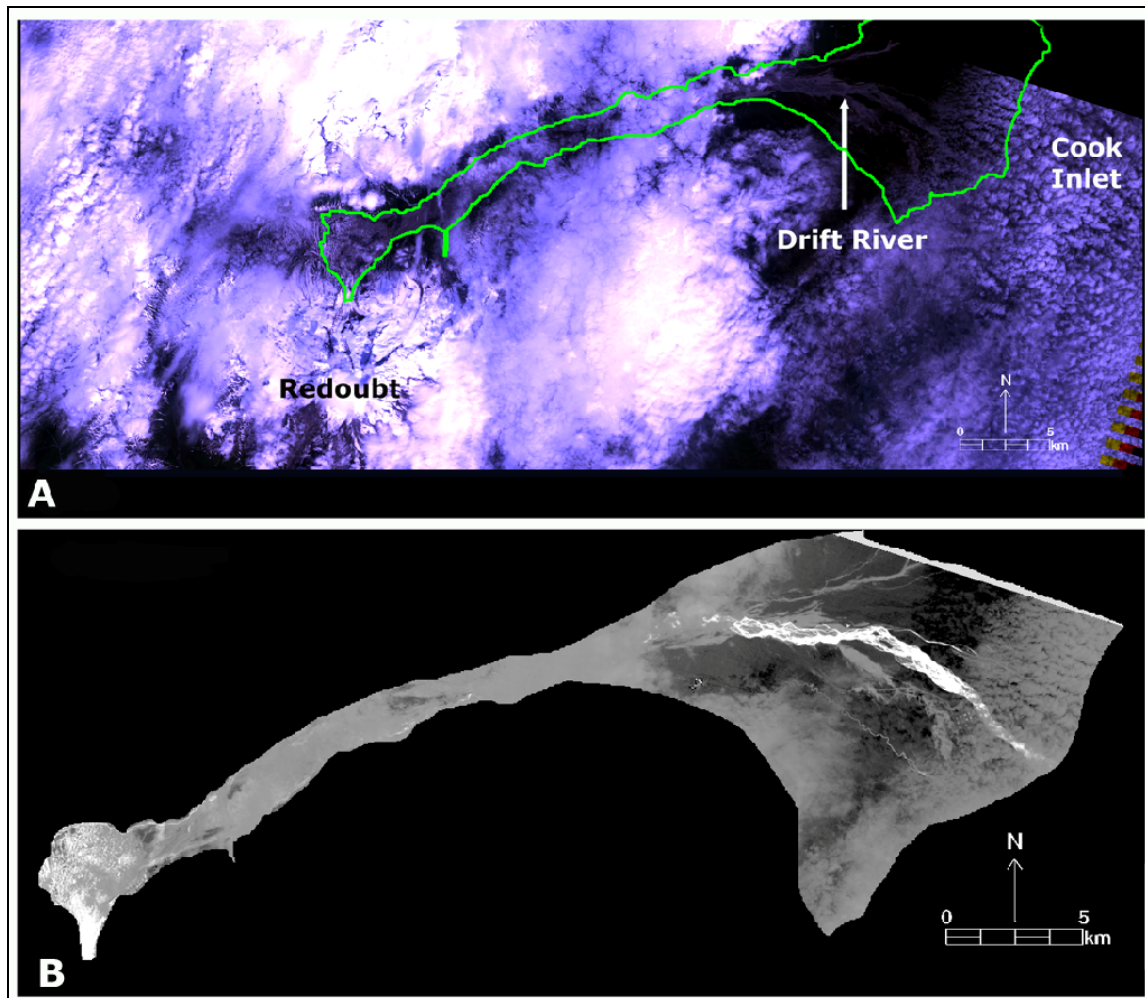


Figure 2.7. Landsat 5 TM June 29, 2006 natural color and NDSI images of Redoubt. (A) Natural color image with the spatial extent of the Drift River valley subset outlined in green and analyzed in (B) using the NDSI band ratio with bright white pixels classified as snow.

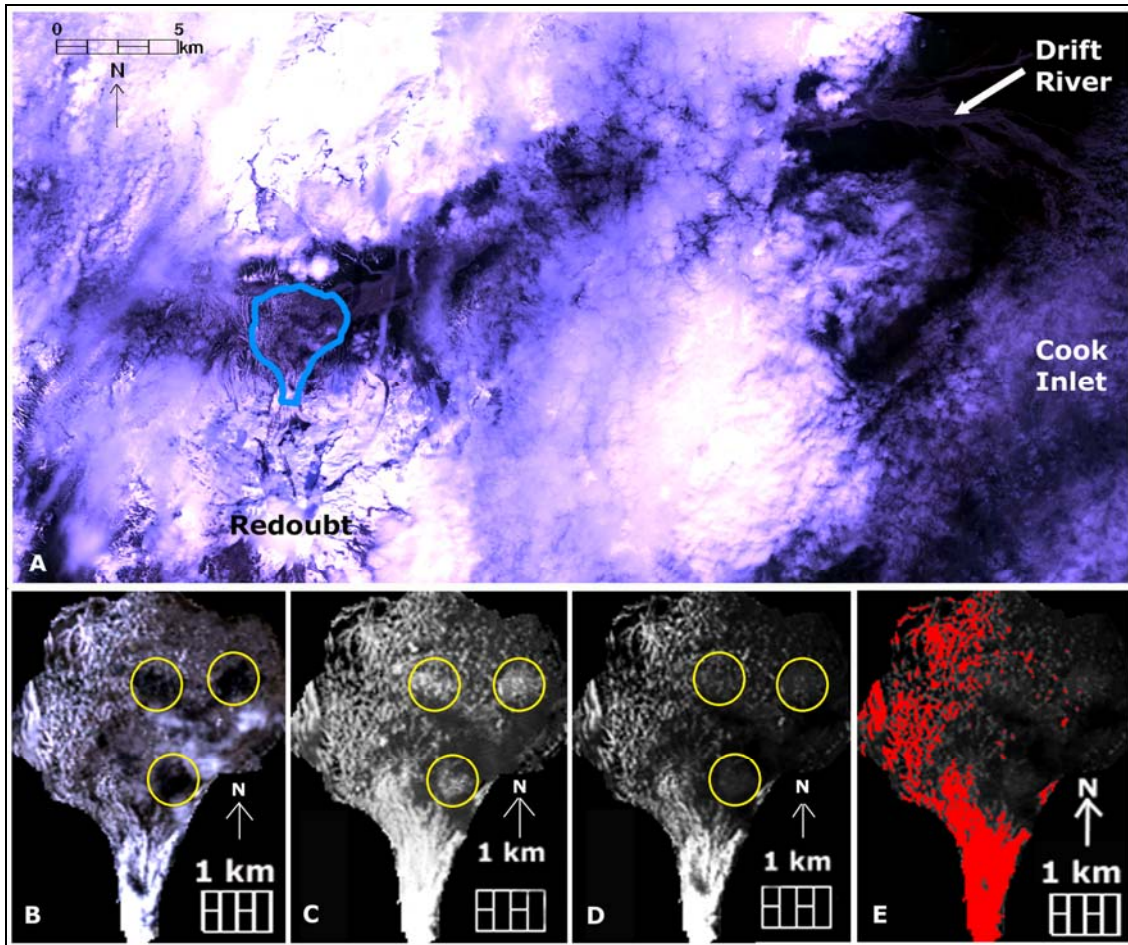


Figure 2.8. Landsat 5 TM June 29, 2006 threshold images of the Drift Glacier lobe. (A) Natural color image showing location of Drift Glacier lobe subset (blue outline). (B) Natural color image of Drift Glacier lobe subset, (C) NDSI band ratio image of Drift Glacier lobe subset with bright white pixels classified as snow/ice, (D) Image of Drift Glacier lobe produced from [Reflectance Band 1 * NDSI] band math with bright white pixels classified as snow/ice. Regions outlined in yellow in (B), (C), and (D) indicate areas of cloud shadow. (E) [Reflectance Band 1 * NDSI] image with mapped snow/ice pixels in red.

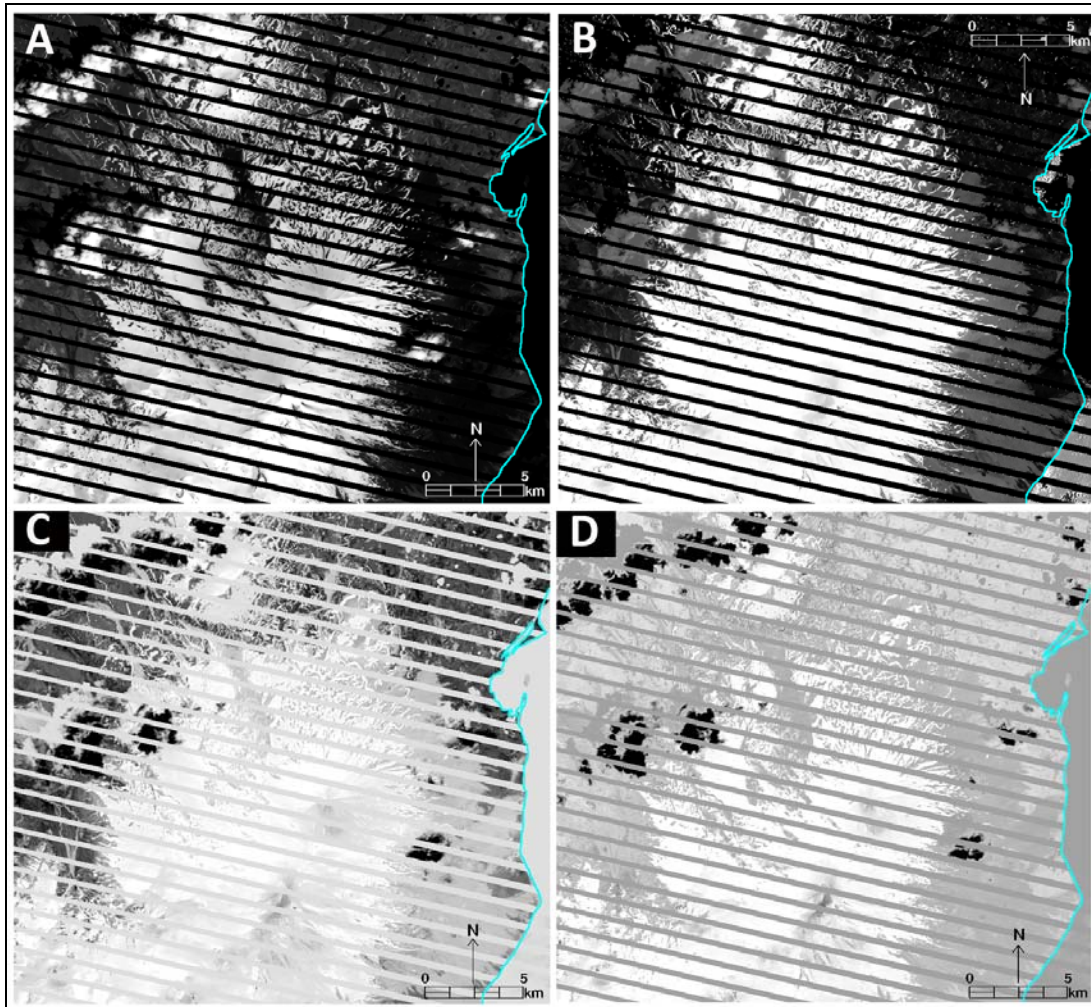


Figure 2.9. Landsat 7 ETM+ June 17, 2012 band ratio and PC images of Pavlof. (A) PC1 image of Pavlof study area, (B) NDSI band ratio image of Pavlof study area with bright white pixels classified as snow/ice, (C) PC2 image of Pavlof study area, and (D) Image of Pavlof study area produced from $[PC1 * PC2]$ band math with bright white pixels classified as snow/ice. Cyan outline in all images denotes coastline. Note: diagonal stripes in all images are SLC-off stripes associated with Landsat 7 ETM+ images acquired after May 31, 2003.

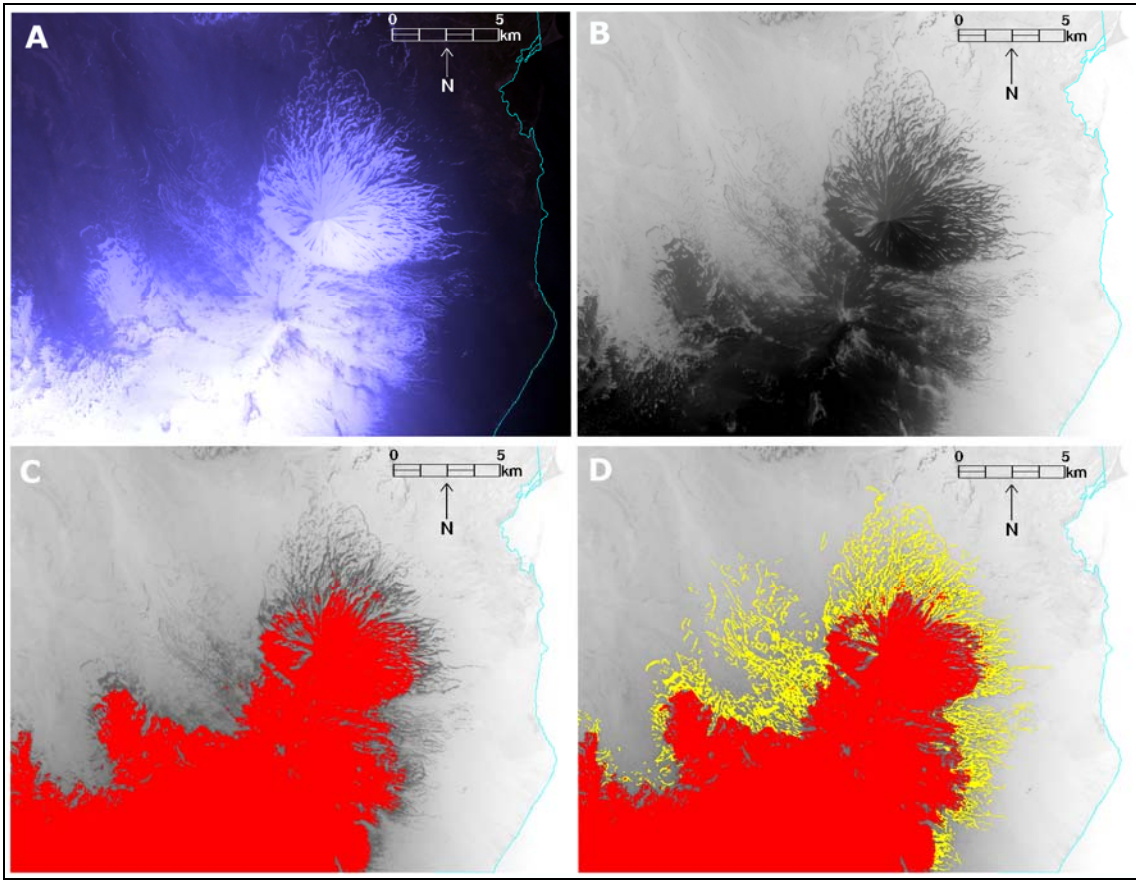


Figure 2.10. Landsat 5 TM May 16, 2009 natural color and PC images of Pavlof. (A) Natural color image of Pavlof study area, (B) PC1 image of Pavlof study area, (C) Map of snow/ice cover using value threshold (in red) using PC1 image of Pavlof study area, (D) Map of snow/ice cover using value threshold (in red) and manual delineation of snow/ice pixels (in yellow) using PC1 image of Pavlof study area. Cyan outline in all images denotes coastline.

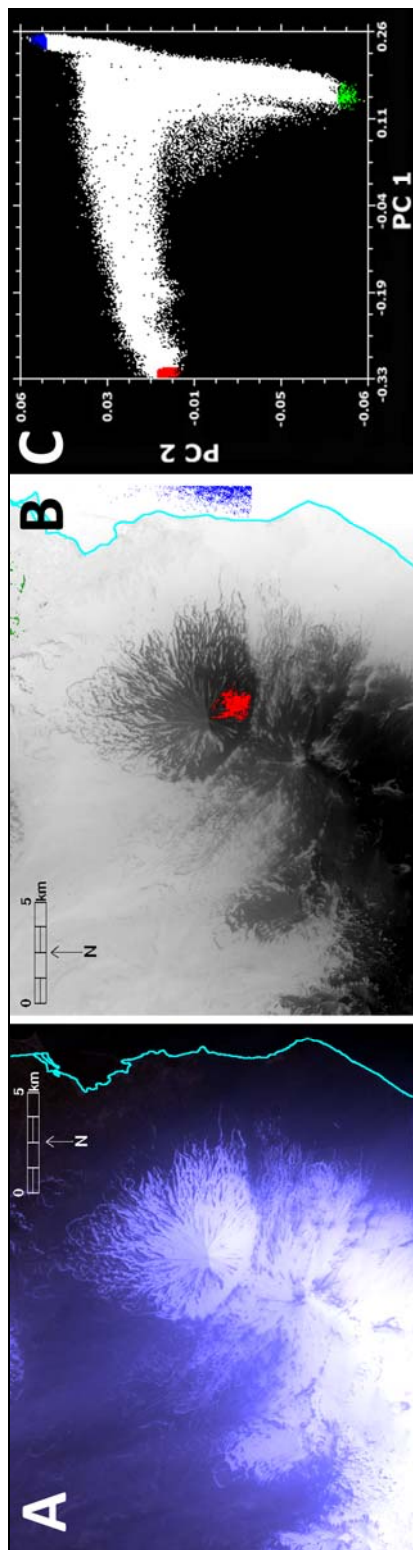


Figure 2.11. Landsat 5 TM May 16, 2009 natural color and endmember selection images of Pavlof. (A) Natural color image of Pavlof study area, (B) PC1 image of Pavlof study area showing spatial location of three main pixel endmembers: snow (in red), water (in blue), and rock (in green), (C) PC1 versus PC2 scatter plot with three colored vertices representing the spectral characteristics of each associated endmember. Cyan outline in all images denotes coastline.

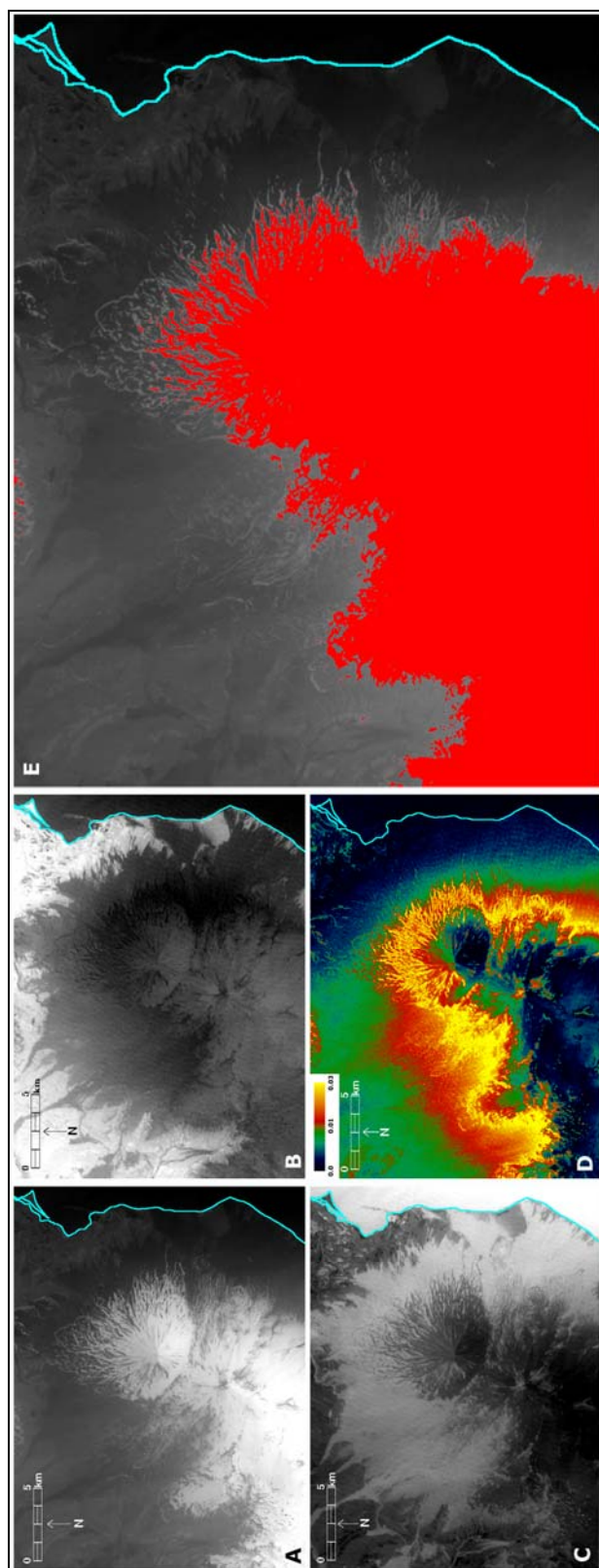


Figure 2.12. Landsat 5 TM May 16, 2009 linear spectral unmixing images of Pavlof. (A) Snow/ice pixel percentage band with high percentage values mapped in white, (B) Bare rock pixel percentage band with high percentage values mapped in white, (C) Water pixel percentage band with high percentage values mapped in white, (D) RMS error band with color mapping that shows yellow pixels as having a high RMS error and black pixels as having a low RMS error, and (E) Snow/ice mapped (in red) using a threshold of pixels with at least 30% snow/ice. Unmapped snow/ice pixels are seen along the periphery of the mapped pixels as whitish-grey features. Cyan outline in all images denotes coastline.

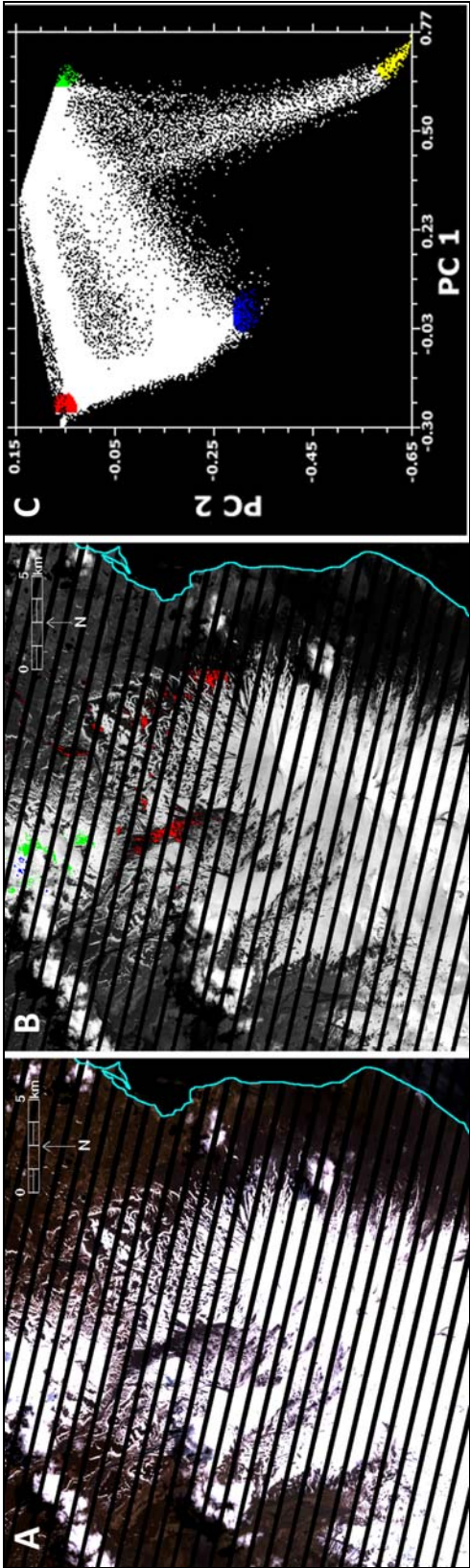


Figure 2.13. Landsat 7 ETM+ June 17, 2012 natural color and endmember selection images of Pavlof. (A) Natural color image of Pavlof study area, (B) PC1 image of Pavlof study area showing spatial location of four main pixel endmembers: rock type one (in red), rock type two (in blue), snow (in green), and cloud cover (in yellow). (C) PC1 versus PC2 scatter plot with four colored vertices representing the spectral characteristics of each associated endmember. Cyan outline in all images denotes coastline.

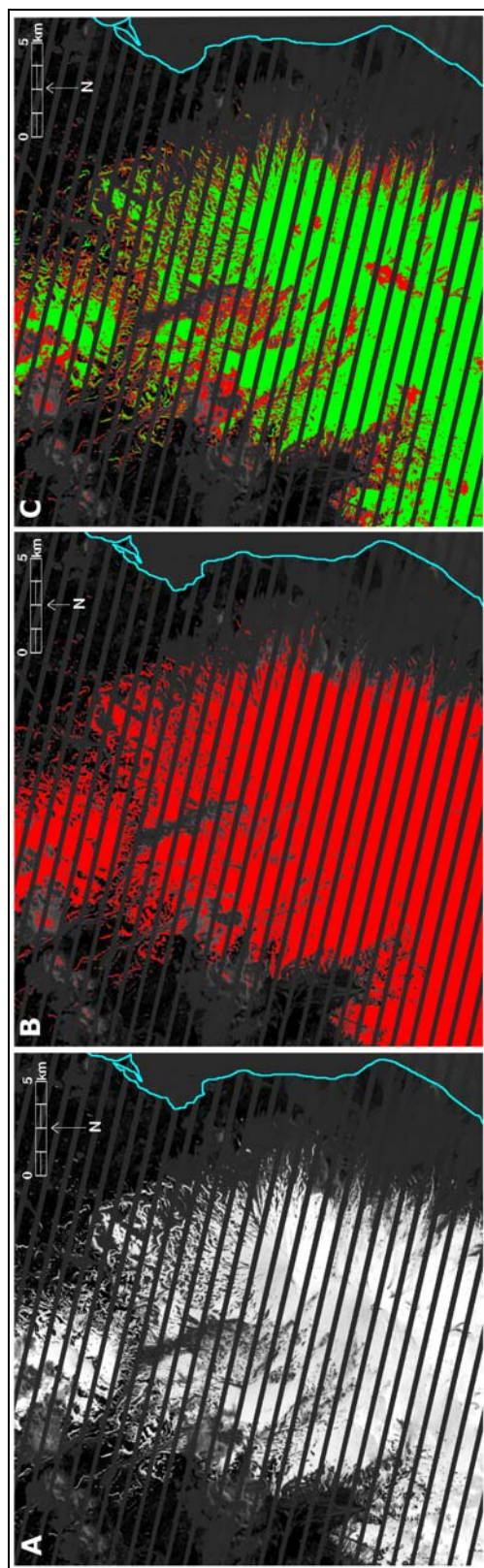
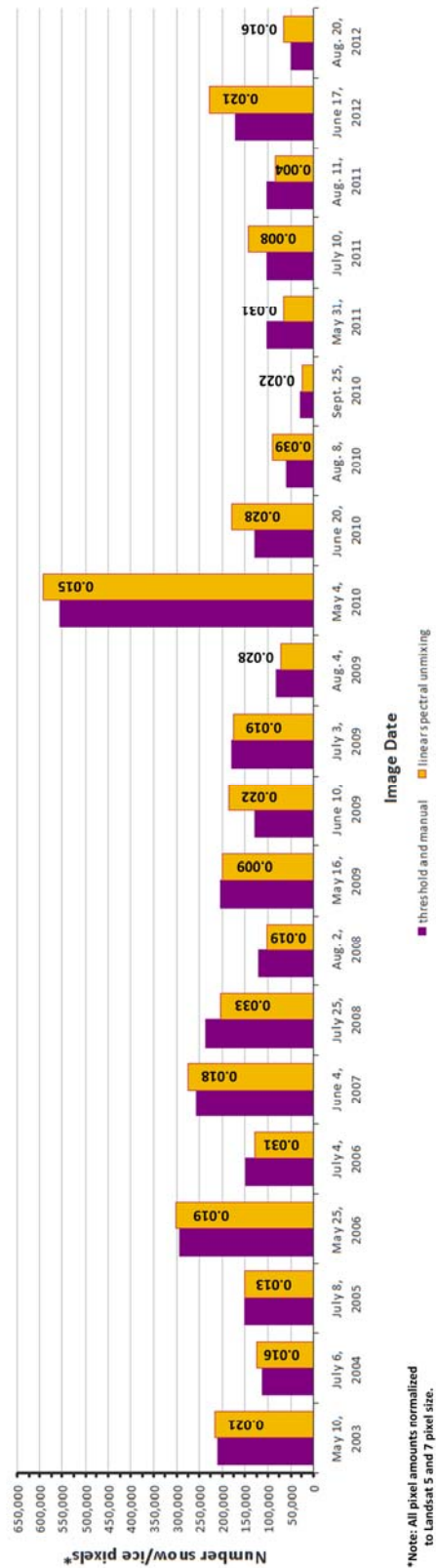


Figure 2.14. Landsat 7 ETM+ June 17, 2012 linear spectral unmixing images of Pavlof. (A) Snow/ice pixel percentage band with high percentage values mapped in white, (B) Snow/ice mapped (in red) of pixels with at least 25% snow/ice. Unmapped snow/ice pixels can be seen along the mapped region as whitish-grey features, and (C) Comparison of snow/ice mapped using threshold/manual technique (in green) and linear spectral unmixing technique (in red). Cyan outline in all images denotes coastline.



*Note: All pixel amounts normalized to Landsat 5 and 7 pixel size.

Figure 2.15. Comparison of snow/ice pixels mapped at Pavlof using threshold and linear spectral unmixing methods Total number of snow/ice pixels mapped using threshold method (in purple) and linear spectral unmixing method (in yellow with RMS error values noted on data bars) for Pavlof study area.

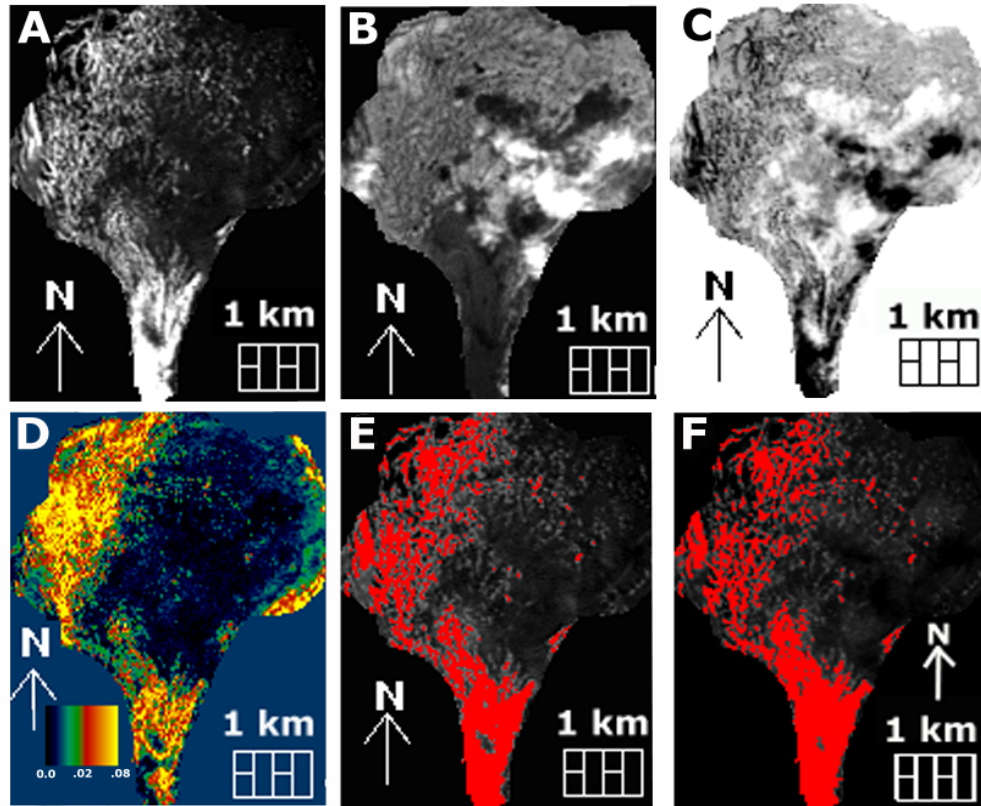


Figure 2.16. Landsat 5 TM June 29, 2006 linear spectral unmixing and band ratio images of the Drift Glacier lobe. Landsat 5 TM image from June 29, 2006 of the Redoubt study area. (A) Snow/ice pixel percentage band with high percentage pixels mapped in white, (B) Cloud cover pixel percentage band with high percentage pixels mapped in white, (C) Shadow pixel percentage band with high percentage pixels mapped in white, (D) RMS error band with color mapping that shows yellow pixels as having a high RMS error and black pixels a low RMS error, (E) Snow/ice mapped (in red) of pixels with at least 25% snow/ice, and (F) [Reflectance Band 1 * NDSI] image with mapped snow/ice pixels in red.

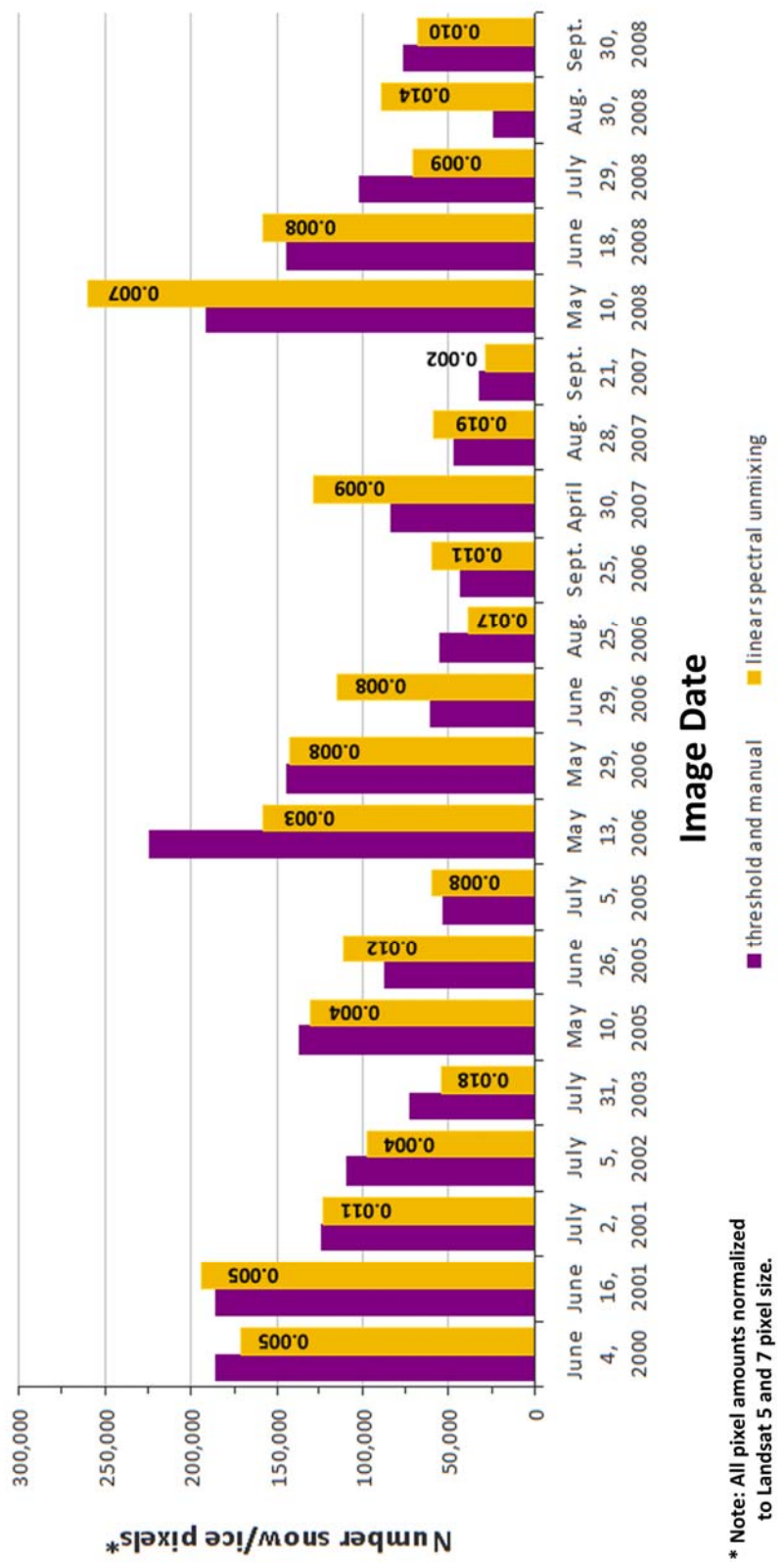


Figure 2.17. Comparison of snow/ice pixels mapped at Redoubt using threshold and linear spectral unmixing methods. Total number of snow/ice pixels mapped using threshold method (in purple) and linear spectral unmixing method (in yellow with RMS error values noted on data bars).

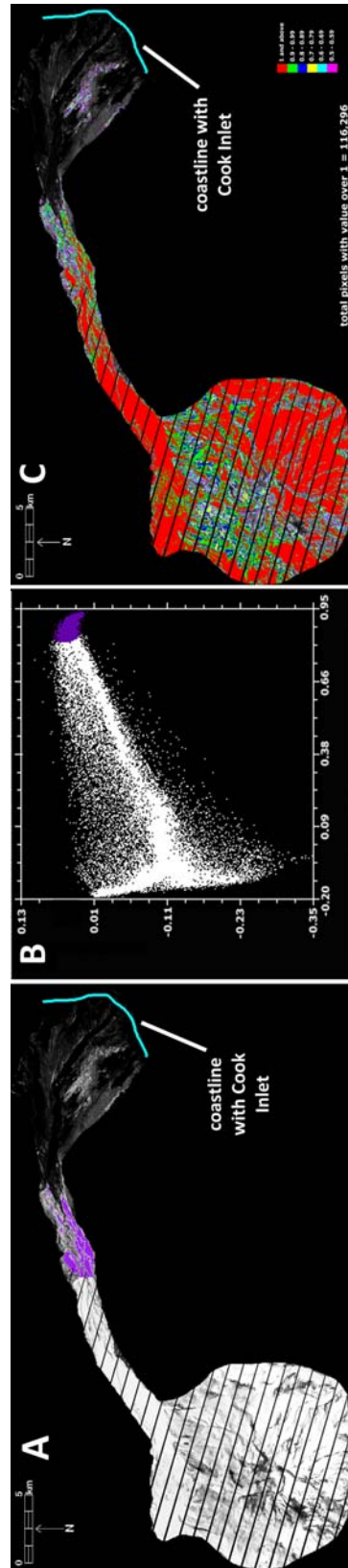


Figure 2.18. Landsat 7 ETM+ May 10, 2005 endmember and linear spectral unmixing images of Redoubt. (A) PC1 image with purple area representing the pixels chosen as the snow/ice endmember, (B) The first iteration of the linear spectral unmixing analysis showing the amount of specific pixel values from 0.50 to above 1, (C) the PC1 versus PC2 scatter plot showing the snow/ice endmember vertex chosen in purple. Coastline with Cook Inlet is outlined in cyan

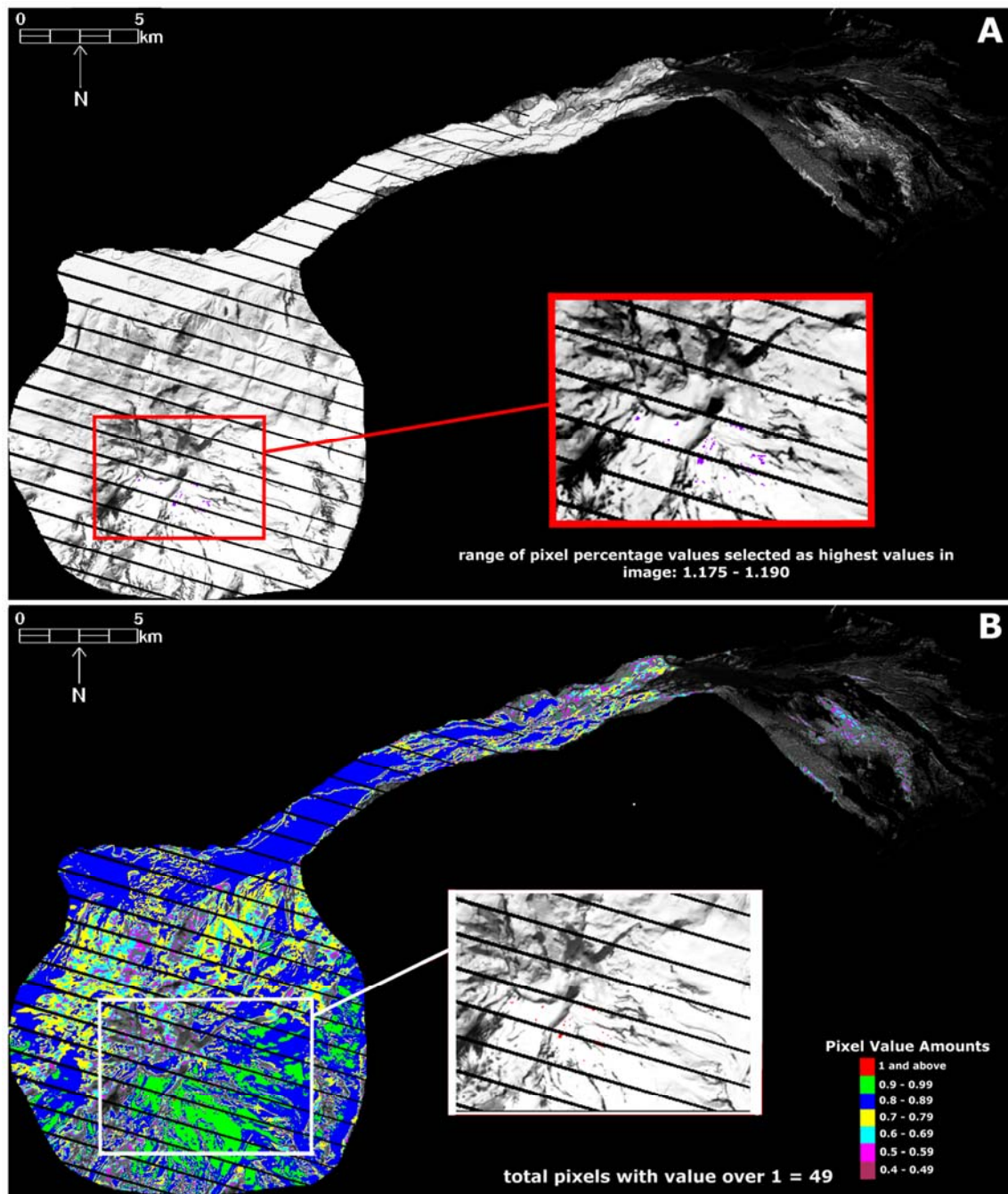


Figure 2.19. Landsat 7 ETM+ May 10, 2005 multiple-iteration image of Redoubt. (A) Iteration 1 linear spectral unmixing output image with purple pixels having the highest pixel percentage value (insert), (B) The second iteration of the linear spectral unmixing analysis showing the amount of specific pixel values from 0.40 to above 1. A total of 49 pixels have values over 1 (insert) in the second iteration image.

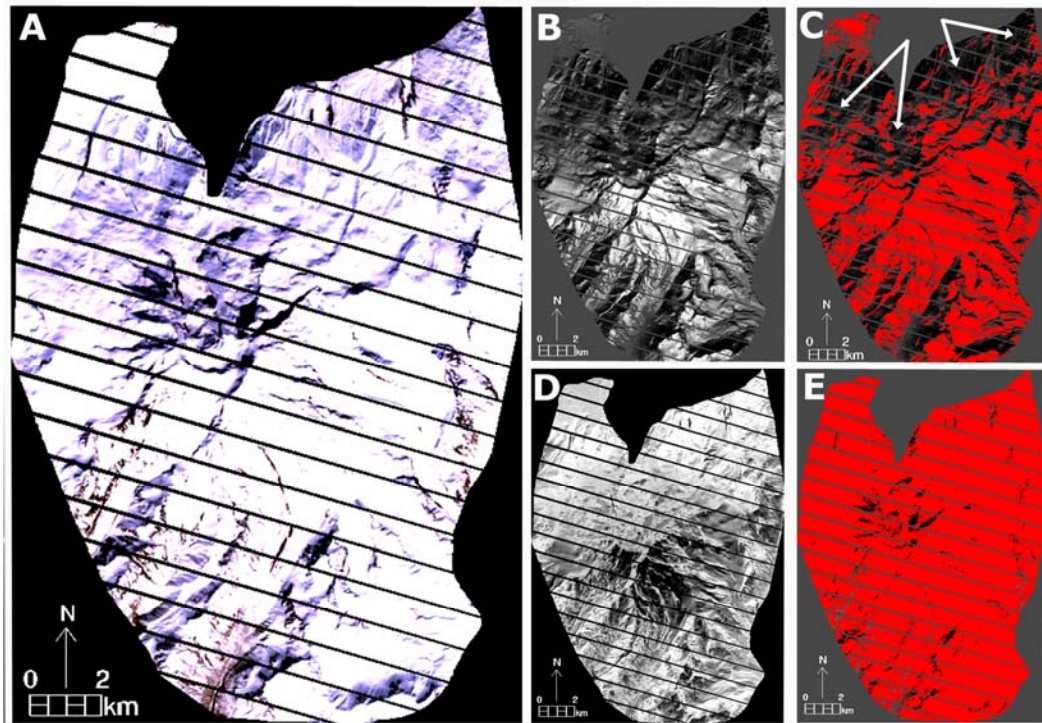


Figure 2.20. Landsat 7 ETM+ May 13, 2006 natural color and linear spectral unmixing images of Redoubt. (A) Natural color image of volcano subset, (B) Output of snow/ice endmember from linear spectral unmixing analysis, (C) Mapped snow/ice pixels using a 30% snow/ice threshold with unmapped shadow areas on the flank of the volcano indicated by white arrows, (D) Output of shadow endmember from linear spectral unmixing analysis, (E) Mapped snow/ice pixels using a combination of 50% snow/ice pixels and 50% shadow pixels.

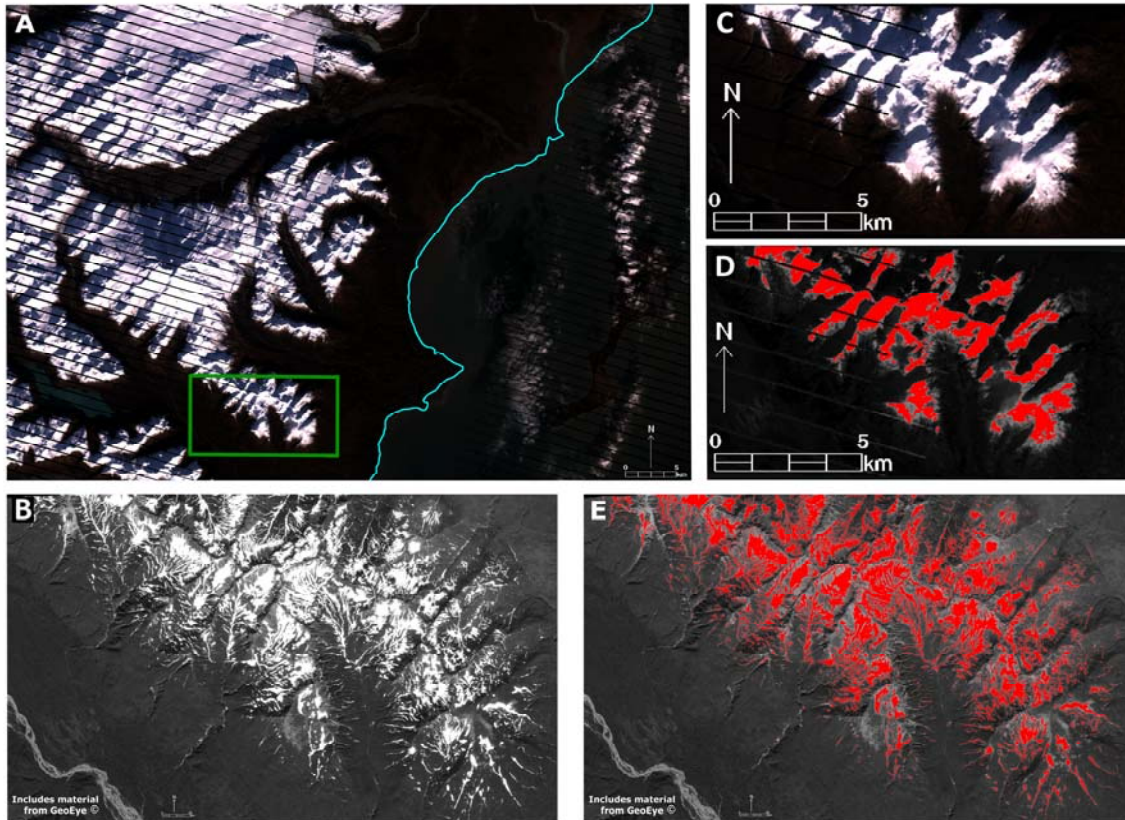


Figure 2.21. Validation of linear spectral unmixing method. (A) Landsat 7 ETM+ natural color image from October 20, 2006 of Redoubt volcano area with validation subset outlined in green, (B) IKONOS band 1 (blue - visible) image with 1m spatial resolution of validation subset, (C) Landsat natural color image of validation subset, (D) Landsat snow/ice map using 50% pixel percentage threshold (in red), (E) Snow/ice map produced using IKONOS band 1 (in red).

Table 2.1. Sensors used to map snow/ice cover at Redoubt and Pavlof volcanoes [VNIR = Visible and Near Infrared; SWIR = Shortwave Infrared; TIR = Thermal Infrared]

Sensor	Full name	Satellite(s)	Availability time range	Nadir Resolution	Scene availability	Bands
Landsat 5 TM	Thematic Mapper	Landsat 5	March 1, 1984 – June 5, 2013	30 m (bands 1 -5, 7) 120 m (band 6)	16 day repeat	7
ASTER	Advanced Spaceborne Thermal Emission and Reflection Radiometer	National Aeronautics and Space Administration (NASA) satellite Terra	December 1999 – present (SWIR bands no longer functional as of 2008)	15 m (VNIR) 30 m (SWIR) 90 m (TIR)	5 day repeat (VNIR) 16 day repeat (SWIR) 16 day repeat (TIR)	15 (including backward-looking band 3B)
Landsat 7 ETM+	Enhanced Thematic Mapper	Landsat 7	April 15, 1999 – present	30 m (bands 1-5, 7) 60 m (band 6) 15 m (band 8)	16 day repeat	8

Table 2.2. Method combinations used to map snow/ice cover with thresholding for Redoubt study area. [**volcano** = volcano subset, **DRV** = Drift River Valley subset, and **lobe** = glacial lobe subset; **PC** = principal component; **NDSI** = normalized difference snow index; **Band designations** refer to at-surface reflectance bands]

Image Date	Thresholding Method Used (Volcano Area)
June 4, 2000	Band 3 (DRV); PC1 (volcano)
June 16, 2001	PC1 (DRV); Band 3 (volcano)
July 2, 2001	Band 1 (DRV); NDSI (volcano)
July 5, 2002	Band 1 (DRV); NDSI (volcano)
July 31, 2003	NDSI (DRV); NDSI (volcano)
May 10, 2005	PC1 (DRV); NDSI (volcano)
June 26, 2005	Band 2 (DRV); NDSI (volcano)
July 5, 2005	NDSI (DRV); PC2 (volcano)
May 13, 2006	PC1 (DRV); Band 1 (volcano)
May 29, 2006	Band 3 (DRV); Band 2 (volcano)
June 29, 2006	NDSI*Band 1 (DRV); NDSI (volcano)
August 25, 2006	Band 1 (volcano)
September 25, 2006	NDSI (volcano)
April 30, 2007	PC2 (DRV); PC2 (volcano)
August 28, 2007	Band 1 (volcano)
September 21, 2007	PC1*NDSI*PC2 (volcano)
October 23, 2007	PC2 (DRV); NDSI (volcano)
May 10, 2008	PC1 (DRV); Band 3 (volcano)
June 18, 2008	PC1*NDSI (DRV); NDSI (volcano)
July 29, 2008	NDSI (DRV); Band 1 (volcano)
August 30, 2008	PC1*PC2 (volcano)
September 30, 2008	Band 1 (volcano)

Table 2.3. Method combinations used to map snow/ice cover with thresholding for Pavlof study area. [**NDSI** = normalized difference snow index; **PC** = principal component]

Image Date	Thresholding Method Used
May 10, 2003	PC2
July 6, 2004	PC1 * PC2
July 8, 2005	PC1
May 25, 2006	PC1
July 4, 2006	(NDSI*NDSI)*PC2
June 4, 2007	(PC1*PC1)*PC2 with NDSI
July 25, 2008	NDSI (high NDSI values associated with water in Pavlof Bay removed manually from pixel count)
August 2, 2008	PC1*PC2
May 16, 2009	PC1
June 10, 2009	PC2
July 3, 2009	PC2*NDSI
August 4, 2009	PC2
May 4, 2010	PC1
June 20, 2010	PC2*NDSI
August 8, 2010	PC2
September 25, 2010	PC2
May 31, 2011	PC2
July 10, 2011	PC2
August 11, 2011	PC1*PC2 with NDSI
June 17, 2012	(PC1*PC1)*PC2
July 19, 2012	PC1*PC2
August 20, 2012	NDSI*PC2

Table 2.4. Data for linear spectral unmixing iterations of Redoubt study area. RMS = root mean square.

Image date	Pre-adjustment snow/ice pixel amount	Pre-adjustment snow/ice percentage threshold used	Pre-adjustment mean RMS error	Pre-adjustment pixel amount over l	Post-adjustment snow/ice pixel amount	Post-adjustment snow/ice percentage threshold used	Post-adjustment mean RMS error	Post-adjustment pixel amount over l	Number of iterations required*
June 4, 2000	209,181	35%	0.013	3,846	198,744	50%	0.009	50	3
June 16, 2001	191,679	50%	0.012	21,255	185,905	50%	0.008	44	2
July 2, 2001	149,605	25%	0.013	1,375	138,466	45%	0.053	44	2
July 31, 2003	81,564	10%	0.003	2,766	75,779	10%	0.007	52	2
May 10, 2005	206,393	50%	0.004	116,296	207,329	40%	0.021	49	2
March 10, 2006	227,644	35%	0.002	88,207	200,074	25%	0.049	44	2
May 13, 2006	215,528	25%	0.008	118,472	209,986	25%	0.050	84	2
June 18, 2008	184,130	25%	0.017	13,215	182,979	25%	0.032	51	2
July 29, 2008	122,023	25%	0.008	3,045	121,295	25%	0.015	44	2
Sept. 30, 2008	71,291	10%	0.007	10,259	70,983	20%	0.026	44	3
March 18, 2009	227,694	50%	0.003	83,824	224,228	30%	0.070	26	3

* Second iteration amounts for: June 4, 2000 = 117 pixels; September 30, 2008 = 6,215 pixels; March 18, 2009 = 36,312 pixels

Table 2.5. Data for linear spectral unmixing iterations of Pavlov study area. RMS = root mean square

Image date	Pre- adjustment snow/ice pixel amount	Pre- adjustment snow/ice percentage threshold used	Pre- adjustment mean RMS error	Pre- adjustment pixel amount over 1	Post- adjustment snow/ice percentage threshold used	Post- adjustment mean RMS error	Post- adjustment pixel amount over 1	Number of iterations required*
July 6, 2004	36,631	35%	0.006	304	25%	0.002	57	2
July 8, 2005	53,704	30%	0.010	3,483	30%	0.008	68	3
May 25, 2006	86,328	30%	0.017	1,945	30%	0.019	52	2
July 4, 2006	55,791	10%	0.011	2,375	10%	0.011	75	2
June 4, 2007	70,727	30%	0.014	2,307	30%	0.016	55	3
Oct. 19, 2007	89,128	25%	0.008	8,822	25%	0.011	58	2
Aug. 2, 2008	40,472	15%	0.005	199	20%	0.001	43	2
Aug. 4, 2009	30,824	10%	0.005	92	10%	0.005	92	1
May 4, 2010	118,752	50% snow, 50% shadow	0.002	11,554	50% snow, 50% shadow	0.004	84	2
June 17, 2012	64,729	30%	0.012	1,648	30%	0.010	85	2
April 26, 2013	106,795	30%	0.022	1,691	25%	0.002	48	2

* Second iteration amounts for: July 8, 2005 = 161 pixels; June 4, 2007 = 166 pixels

References

- Abrams, M., Hook, S., and Ramachandran, B. 2004: ASTER User Handbook: Version 2, NASA Jet Propulsion Laboratory, California Institute of Technology
- Arendt, A.A., Echelmeyer, K.A., Harrison, W.D., Lingle, C.S., and Valentine, V.B. 2002: Rapid Wastage of Alaska Glaciers and Their Contribution to Rising Sea Level: *Science*, v. 297, n. 5580, 382 – 386.
- Begét, J.E. 2010: Characterizing pyroclastic-flow interactions with snow and water using environmental magnetism at Augustine Volcano, chapter 11 of Power, J.A., Coombs, M.L., Freymueller, J.T. eds., The 2006 Eruption of Augustine Volcano, Alaska: U.S. Geological Survey Professional Paper 1769, 269 - 283.
- Berthier, E., Schiefer, E., Clarke, G.K.C., Menounos, B., and Rémy, F. 2010: Contribution of Alaskan glaciers to sea-level rise derived from satellite imagery: *Nature Geoscience*, v. 3, 92 – 95.
- Bitz, C.M. and Battisti, D.S. 1999: Interannual to Decadal Variability in Climate and the Glacier Mass Balance in Washington, Western Canada, and Alaska: *Journal of Climate*, v. 12, Issue 11, 3181 – 3196.
- Bleick, H.A., Coombs, M.L., Cervelli, P.F., Bull, K.F., and Wessels, R.L. 2013: Volcano-ice interactions precursory to the 2009 eruption of Redoubt Volcano, Alaska: *Journal of Volcanology and Geothermal Research*, 373 - 388.
- Boresjö Bronge, L. and Bronge, C. 1999: Ice and snow-type classification in the Vestfold Hills, East Antarctica, using Landsat-TM data and ground radiometer measurements: *International Journal of Remote Sensing*, v. 20, n. 2, 225 – 240.
- Buurman, H., West, M.E., and Thompson, G. 2013: The seismicity of the 2009 Redoubt eruption: *Journal of Volcanology and Geothermal Research*, v. 259, 16 – 30.
- Chander, G., Markham, B.L., and Helder, D.L. 2009: Summary of current radiometric calibration coefficients for Landsat MSS, TM, ETM+, and EO-1 ALI sensors: *Remote Sensing of Environment*, v. 113, 893 – 903.
- Chavez Jr., P.S. 1988: An improved dark-object subtraction technique for atmospheric scattering correction of multispectral data: *Remote Sensing of Environment*, v. 24, 459 – 479.
- Cloutis, E.A. 1996: Review Article Hyperspectral geological remote sensing, evaluation of analytical techniques: *International Journal of Remote Sensing*, v. 17, Issue 12, 2215 – 2242.
- Cogley, J.G. 2010: A more complete version of the World Glacier Inventory: *Annals of Glaciology*, v. 50, no. 53, 32 – 38.
- Cuffey, K.M. and Paterson, W.S.B. 2010. The Physics of Glaciers, 4th Ed. Elsevier, Inc., Burlington, M.A.

- Dean, K.G., Dehn, J., Engle, K., Izbekov, P., Papp, K., and Patrick, M. 2002: Operational Satellite Monitoring of Volcanoes at the Alaska Volcano Observatory: *Advances in Environmental Monitoring and Modelling*, v. 1, no. 1, 70 – 97.
- Dehn, J., Dean, K., and Engle, K. 2000: Thermal monitoring of North Pacific volcanoes from space: *Geology*, v. 28, no. 8, 755-758.
- Dial, G., Bowen, H., Gerlach, F., Grodecki, J., and Oleszczuk, R. 2003: IKONOS satellite, imagery, and products: *Remote Sensing of Environment*, v. 88, 23 – 36.
- Dozier, J. 1989: Spectral signature of alpine snow cover from the landsat thematic mapper: *Remote Sensing of Environment*, v. 28, 9 – 22.
- Dozier, J. and Painter, T.H. 2004: Multispectral and Hyperspectral Remote Sensing of Alpine Snow Properties: *Annual Review of Earth and Planetary Sciences*, v. 32, 465-494.
- Driedger, C. 1981: Effect of ash thickness on snow ablation. In P. W. Lipman, & D. R. Mullineaux (Eds.), *The 1980 eruptions of Mt. St. Helens, Washington*, USGS professional paper, v. 1250, 757–760. Washington, DC: U.S. Geological Survey.
- Edwards, B., Magnússon, E., and Thordarson, T. 2012: Interactions between lava and snow/ice during the 2010 Fimmvörðuháls eruption, south-central Iceland: *Journal of Geophysical Research*, v.117, 1-21.
- EXELIS. (2014, January 28). *Linear Spectral unmixing*. Retrieved from <<http://www.exelisvis.com/docs/linearspectralunmixing.html#results>>
- Foppa, N., Wunderle, S., and Hauser, A. 2002: Spectral Unmixing of NOAA-AVHRR Data for Snow Cover Estimation: *Proceedings of EARSeL-LISSIG-Workshop: Observing our Cryosphere from Space, Bern, March 11 – 13, 2002*, 8 p.
- GLIMS, and NSIDC (comps.). 1999, updated 2013. *Global Land Ice Measurement from Space*. [Alaska]. Boulder, Colorado USA: National Snow and Ice Data Center. <<http://nsidc.org/glims/>>
- Gjermundsen, E.F., Mathieu, R., Käab, R., Chinn, T., Fitzharris, B., Hagen, J.O. 2011: Assessment of multispectral glacier mapping methods and derivation of glacier area changes, 1978-2002, in the central Southern Alps, New Zealand, from ASTER satellite data, field survey and existing inventory data: *Journal of Glaciology*, v. 57, no. 204, 667 – 683.
- Hall, D.K., Riggs, G.A., Salomonson, V.V., DiGirolamo, N.E., and Bayr, K.J. 2002: MODIS snow-cover products: *Remote Sensing of Environment*, v. 83, issues 1-2, 181-194.
- Jolliffe, I.T. 2002. *Principal Component Analysis*, 2nd Ed. Springer, New York, N.Y.
- Kennedy, G.C. and Waldron, H.H. 1955: Geology of Pavlof Volcano and Vicinity Alaska: Investigations of Alaskan Volcanoes: *Geological Survey Bulletin* 1028 – A.

- Klein, A.G. and Barnett A.C. 2003: Validation of daily MODIS snow cover maps of the Upper Rio Grande River Basin for the 2000-2001 snow year: *Remote Sensing of Environment*, v. 86, Issue 2, 162 – 176.
- König, M., Winter, J.G., and Isaksson, E. 2001: Measuring snow and glacier ice properties from satellite: *Reviews of Geophysics*, v. 39, Issue 1, 1 – 27.
- Kulkarni, A.V., Srinivasulu, J., Manjul, S.S., and Mathur, P. 2002: Field Based Spectral Reflectance Studies to Develop NDSI Method for Snow Cover Monitoring: *Journal of the Indian Society of Remote Sensing*, v. 30, n. 1&2, 73 – 80.
- Larsen, C.F., Motyka, R.J., Arendt, A.A., Echelmeyer, K.A., and Geissler, P.E. 2007: Glacier changes in southeast Alaska and northwest British Columbia and contribution to sea level rise: *Journal of Geophysical Research*, v. 112, Issue F1, 1 – 11.
- McNutt, S.R. 1987. Eruption characteristics and cycles at Pavlof volcano, Alaska, and their relation to regional earthquake activity: *Journal of Volcanology and Geothermal Research*, v. 31, 239 – 267.
- Paul, F. 2000: Evaluation of Different Methods for Glacier Mapping Using Landsat TM: *EARSeL eProceedings*, no. 1, 239 – 245.
- Pierson, T.C., Janda, R.J., Thouret, J.C., and Borrero, C.A. 1990: Perturbation and melting of snow and ice by the 13 November 1985 eruption of Nevado del Ruíz, Colombia, and consequent mobilization, flow and deposition of lahars: *Journal of Volcanology and Geothermal Research*, v. 41, issues 1-4, 17-66.
- Radić, V. and Hock, R. 2010: Regional and global volumes of glaciers derived from statistical upscaling of glacier inventory data: *Journal of Geophysical Research: Earth Surface*, v. 115, Issue F1, 10 p.
- Raup, B., Arendt, A., Armstrong, R., Barrett, A., Jodha Khalsa, S., and Racoviteanu, A. 2013: GLIMS and the RGI: Relationships present and future: *EGU General Assembly Conference Abstracts*, v. 15, p. 11831.
- Rivera, A., Bown, F., Mella, R., Wendt, J., Casassa, G., Acuña, C., Rignot, E., Clavero, J., and Brock, B. 2006: Ice volumetric changes on active volcanoes in southern Chile: *Annals of Glaciology*, v.43, 111-122.
- Schaefer, J. and Nye, C. 2008: The Alaska Volcano Observatory – 20 Years of Volcano Research, Monitoring, and Eruption Response: *Alaska GeoSurvey News*, v. 11, no. 1, 1 – 9.
- Shulski, M. and Wendler, G. 2007. The Climate of Alaska, University of Alaska Press, Fairbanks, A.K.
- Sidjak, R.W. and Wheate, R.D. 1999: Glacier mapping of the Illecillewaet icefield, British Columbia, Canada, using Landsat TM and digital elevation data: *International Journal of Remote Sensing*, v. 20, n. 2, 273 - 284.

- Smellie, J.L. 2006: The relative importance of supraglacial versus subglacial meltwater escape in basaltic subglacial tuya eruptions: An important unresolved conundrum: *Earth-Science Reviews*, v.74, 241 – 268.
- Trabant, D.C., Waitt, R.B., Major, J.J. 1994: Disruption of Drift glacier and origin of floods during the 1989-1990 eruptions of Redoubt Volcano, Alaska: *Journal of Volcanology and Geothermal Research*, v. 62, issues 1-4, 369-385.
- Trabant, D.C. and Hawkins, D.B. 1997: Glacier Ice-Volume Modeling and Glacier Volumes On Redoubt Volcano, Alaska: *U.S. Geological Survey Water-Resources Investigations Report 97-4187*.
- Van Der Meer, F. and De Jong, S.M. 2000: Improving the results of spectral unmixing of Landsat Thematic Mapper imagery by enhancing the orthogonality of end-members: *International Journal of Remote Sensing*, v. 21, no. 15, 2781 – 2797.
- Waitt, R.B., Gardner, C.A., Pierson, T.C., Major, J.J., and Neal, C.A. 1994: Unusual ice diamicts emplaced during the December 15, 1989 eruption of redoubt volcano, Alaska: *Journal of Volcanology and Geothermal Research*, v. 62, Issues 1 – 4, 409 – 428.
- Waythomas, C.F., Miller, T.P., Mangan, M.T. 2006. Preliminary volcano hazard assessment for the Emmons Lake Volcanic Center, Alaska. United States Geological Survey Scientific Investigations Report 2006 – 5248, 33 p.
- Waythomas, C.F., Pierson, T.C., Major, J.J., and Scott, W.E. 2013: Voluminous ice-rich and water-rich lahars generated during the 2009 eruption of Redoubt Volcano, Alaska: *Journal of Volcanology and Geothermal Research*, 389 - 413.
- Webley, P.W., Dehn, J., Lovick, J., Dean, K.G., Bailey, J.E., and Valcic, L. 2009: Near-real-time volcanic ash cloud detection: Experiences from the Alaska Volcano Observatory: *Journal of Volcanology and Geothermal Research*, v.186, Issues 1-2, 79-90.
- Werner, C.A., Doukas, M.P., and Kelly, P.J. 2011: Gas emissions from failed and actual eruptions from Cook Inlet Volcanoes, Alaska, 1989 – 2006: *Bulletin of Volcanology*, v. 73, 155 – 173.
- Wessels, R., Neal, C.A., Waythomas, C., Huggel, C., and Dean, K. 2007: Satellite measurement of glaciers on volcanoes in Alaska: Building an inventory of ice extent and hazards: *Abstract from the 103rd Annual Meeting of the Cordilleran Section of the Geological Society of America*
- Xiao, X., Shen, Z., and Qin, X. 2001: Assessing the potential of VEGETATION sensor data for mapping snow and ice cover: a Normalized Difference Snow and Ice Index: *International Journal of Remote Sensing*, v. 22, n. 13, 2479 - 2487.

Chapter 3 Observations of surficial snow/ice cover changes due to seasonal and eruptive influences on Redoubt and Pavlof volcanoes, Alaska using optical remote sensing²

Abstract

Alaska is a unique locality to study the juxtaposition of snow/ice cover and active volcanism. The snow/ice cover at Alaskan volcanoes is extremely varied. Glacial ice or perennial snow covers at least 30 of the historically active volcanoes in Alaska with all volcanoes being covered by some amount of seasonal snow for a period of time throughout the year. Seasonal snow can be a significant contributor to meltwater generated during an eruption. Therefore, the timing of an eruption will determine the extent of seasonal snow present at the volcano, with eruptions at the end of the ablation season interacting with less seasonal snow than during winter eruptions. The most drastic change to the spatial extent of seasonal snow cover at an Alaskan volcano will occur throughout the Alaskan summer months, from approximately May through the reappearance of fresh snow around the end of September or beginning of October. By examining the changing spatial extent of seasonal snow present at a volcano during multiple summers, the approximate boundaries of perennial snow and ice can be mapped as the snow/ice cover consistently present at the end of each ablation season. In this study, the snow/ice cover is mapped at Redoubt and Pavlof volcanoes using mostly cloud-free Landsat imagery throughout multiple summers. Snow/ice cover type is then delineated into areas of seasonal snow versus perennial snow and ice. Maps of snow/ice cover are then spatially linked to volcanic products produced during the 2009 eruption of

Redoubt and 2013 eruption of Pavlof, allowing for observations as to how the visible snow/ice cover varies during and after both eruptions.

3.1 Introduction

The intersection between active volcanism and underlying snow/ice cover is prevalent at many volcanoes worldwide (Major and Newhall, 1989). Glaciovolcanism is the study of how a volcano and glacier interact thermally, mechanically, and chemically (Walder 2000a, 2000b; Smellie, 2006). This interaction is complex and may be examined through a number of different paths ranging from how the glacier affects the volcano to how an active volcano and its products affect the glacier. The importance of glaciovolcanism does not lie solely in studying glacier clad volcanoes but volcanoes with seasonal or perennial snow/ice cover as well. While dramatic changes in the extent of snow/ice cover along a volcano's flanks can occur due to increased melting, smaller changes such as the addition of fresh snowfall during an eruption are also possible (Trabant et al., 1994). The hazards associated with melting of snow/ice cover can change drastically during an eruption as the deposition of new volcanic products can either accelerate melting or provide insulation from further melt (Driedger, 1981; Walder, 2000a, 2000b; Edwards et al., 2012). Mapping of the snow/ice cover present along the flank of a volcano and within the surrounding valley regions is beneficial during periods of both quiescence and eruption in order to better characterize the possible hazards

resulting from the interaction between active volcanism and snow/ice cover (Wessels et al., 2007).

3.1.1 Alaskan volcanoes

Alaska is a natural laboratory for studying the interaction between active volcanism and glacial ice or snow cover. Out of the 80 Alaskan volcanoes active within the Holocene, over 30 are covered to some extent by glacial ice or perennial snow (Wessels et al., 2007). During the winter and spring, Alaskan volcanoes will also be covered by seasonal snow. Throughout this study, we refer to the combined presence of glacial ice, perennial snow, and seasonal snow as snow/ice cover, with seasonal snow melting by the end of the local summer season and perennial snow classified as snow that remains after two consecutive local summer seasons (Watanabe, 1988). The majority of historically active Alaskan volcanoes are located along the 2,600 km-long Aleutian volcanic arc, bound to the east by Cook Inlet and stretching westward towards the Bering Sea (Miller and Chouet, 1994). A large percentage of Alaskan volcanoes are located within remote, sparsely populated regions, making ground-based monitoring these volcanoes a challenge. The Alaska Volcano Observatory (AVO) is tasked with monitoring Alaska's volcanoes and remote analysis of satellite imagery has become one of the most reliable ways to track both eruptive and background behaviors (Nye et al., 2002). Our study focuses on the snow/ice cover area at two Alaskan volcanoes: Redoubt and Pavlof (Figure 3.1).

3.2 Volcano – snow/ice interactions

Interactions between a volcano and its snow/ice cover range from short term interactions during an eruption to the long term interactions prevalent during quiescence. Volcano-snow/ice interactions can be complex and full characterization of these interactions is beyond the scope of our study. However, a summary of possible short and long term volcano-snow/ice interactions is addressed here.

3.2.1 Short term interactions

Short term volcano-snow/ice interactions are linked to the products and forces associated with an active eruption. These can be broken down even further into combined thermal-mechanical and solely thermal interactions (Walder, 2000a, 2000b). Common volcanic products with thermal-mechanical properties include pyroclastic density currents (PDCs) and ejected crater lake water (Major and Newhall, 1989; Walder, 2000a, 2000b). Previous studies have shown that interactions involving a combination of thermal and mechanical forces are necessary in order to efficiently melt enough snow/ice to form a lahar, or volcanic mud flow (Major and Newhall, 1989; Walder, 2000a, 2000b). PDCs, as hot gas-particle currents, are believed to be the most efficient at eroding and melting snow/ice (Walder, 2000b). A less common process, also efficient at melting snow/ice, is an eruption through a crater lake. High temperatures are possible at crater lakes found at the summit of thermally active volcanoes. For instance, Martínez et al. (2000) documented a maximum crater lake temperature of 70°C during a four year period

following an eruption at Poás volcano in Costa Rica. The release of hot crater lake water over the flanks of a volcano would have enough thermal and mechanical force to cause scouring of the snow/ice (Major and Newhall, 1989).

Simple heat transfer from more static volcanic products is possibly not enough to induce the melt necessary to form a lahar (Walder, 2000a, 2000b). Although ash may still be radiating heat when it is deposited on top of the snow/ice cover, the ash cools too rapidly and without enough mechanical force to cause sufficient melt (Major and Newhall, 1989). A lava flow emplaced horizontally on top of snow/ice is another example where melt is not generated within an appropriate time scale (Major and Newhall, 1989; Walder, 2000a, 2000b; Edwards et al., 2012). Wilson and Head (2007) suggest that although a lava flow conducts heat to the underlying snow/ice cover, the flow will lose heat rapidly to the atmosphere. Additionally, the base of the lava flow will quickly equilibrate to the melting point of ice, reducing the melt rate as the thermal gradient between the two materials rapidly decreases. Wilson and Head (2007) found that within the first 10 minutes of emplacement, a 1 m thick horizontal lava flow will melt underlying ice at an 85% greater rate than the rate melted by a 10 m thick flow. The insulating capabilities of the thicker flow results in a smaller decrease in the ice melt rate over time. After 4 hours of emplacement, the rate of ice melt beneath the 1 m thick horizontally emplaced flow will approach that of the 10 m thick flow (Wilson and Head, 2007). It takes approximately 20 hours for 90% melt to be achieved beneath the 1 m thick flow and 3 months for 90% melt beneath the 10 m thick flow (Wilson and Head, 2007). Meltwater heated at the flow-ice interface would need to be heated to a temperature of

80°C to effectively double the total volume of ice melted (Wilson and Head, 2007). However, basaltic lava flows on steep-sloped, ice-clad volcanoes can cause small-scale phreatomagmatic explosions from overpressured steam formed due to melting of the frozen substrate (see Belousov et al., 2011). In this situation, melting of the snow/ice causes a “pressurized bowl” of steam and meltwater that can explode if the overburden pressure of the advancing lava flow is small enough (Belousov et al., 2011). A steep-sloped flank will enhance the likelihood that this steam explosion will cause fragmentation of the lava flow front and mechanical mixing of the lava material with meltwater. A small pyroclastic density current can then form at the flow front, where further entrainment of enough meltwater can cause the production of lahars (Belousov et al., 2011). This idea is of particular importance to our study as Pavlof is one of the localities where this lava-ice interaction may occur (Belousov et al., 2011).

An additional interaction occurs in subglacial eruptions. During periods of increased thermal output, a glacier overlying a volcano will undergo increased basal melting (Björnsson, 2003). The surficial evidence of basal melting is the formation of an ice cauldron, an elliptical area of subsided ice that forms over the zone of increased heat output (Bleick et al., 2013). If enough meltwater is accumulated to form a subglacial lake, the basal water pressure can approach the overburden pressure of the overlying glacier (Björnsson, 2003). If the basal pressure exceeds the overburden pressure, the ice dam of the subglacial lake will float, allowing the meltwater to flood outward from the glacier (Björnsson, 2003). The gradual thermal erosion of subglacial conduits can also allow for eventual large-scale flooding of the subglacial lake without requiring basal pressure to

exceed overburden pressure (Björnsson, 2010). Flood events from a subglacial lake are commonly referred to as jökulhlaups, Icelandic for “glacial bursts”, and are a common occurrence at subglacial eruptions in Iceland (Björnsson, 2003; Eliasson et al., 2006; Dunning et al., 2013). Jökulhlaups can form due to increased hydrothermal output or may form due to the subglacial emplacement of hot volcanic materials during an eruption (Björnsson, 2003; Eliasson et al., 2006). Numerous jökulhlaups were observed during the 1966-1968 eruption of Redoubt volcano (Sturm et al., 1986).

3.2.2 Long term interactions

Long term interactions involving snow/ice cover can be present at both active and quiescent volcanic systems. Basal melting of snow/ice cover, for example, may occur during either eruptive or non-eruptive activities due to continuous geothermal activity common at many active volcanoes (Rivera et al., 2006). In order to quantify the influence of long-term basal melting of a glacier on an active volcano, Rivera et al. (2006) studied two glaciated volcanoes in Chile: Volcán Villarrica and Volcán Mocho. The two volcanoes are located within the same region and thus undergo similar weather patterns and climate. However, Villarrica has been consistently active since 1971 and Mocho has been in a period of quiescence since 1864 (Rivera et al., 2006). The glacier on Villarrica has experienced a greater amount of thinning than that on Mocho, suggesting that the higher level of consistent geothermal activity at recently active Villarrica played a large part in glacial melting over time (Rivera et al., 2006).

Another variable in the volcano-snow/ice system is the presence of ash cover. The interaction between ash cover and underlying snow/ice is dependent on the thickness of the ash layer (Driedger, 1981; Adhikary et al., 2002). Adhikary et al. (2002) studied the snow/ice melt generated beneath dust layers of varying thicknesses. They concluded that a thin layer of dust will decrease the albedo of the snow/ice surface, therefore increasing ablation due to a greater penetration of solar radiation. However, they also stated that a thicker dust layer will begin to thermally insulate the underlying snow/ice and will result in decreased melting. Additionally, Driedger (1981) found that during the 1980 eruption of Mount St. Helens volcano, the maximum ablation rate of snow/ice occurred under a 3 mm thick cover of ash, whereas a large drop in ablation occurred when the ash cover was more than 24 mm thick.

3.2.3 Lahar formation and hazards

Lahars are volcanic mud flows characterized by fine-grained sediments (mostly silt to clay sized) and a sediment load of generally greater than 60 volume percent (Pierson, 2005). Debris flows, though at times used interchangeably with lahars, are typically characterized by larger, sand-sized sediments (Pierson, 2005). Lahars form when volcanic debris becomes mobilized, typically by snow/ice meltwater, rainwater, or water expelled from a crater lake (Major and Newhall, 1989; Paguican et al., 2009). Lahars can have long reaching and devastating consequences, making them one of the greatest hazards for populations on and around snow/ice covered volcanoes (Major and Newhall, 1989; Kerle et al., 2003). A voluminous lahar can form, even during small

eruptions, if the appropriate conditions are present. One example is the 1985 eruption of Nevado del Ruíz volcano in Colombia. The eruption was of moderate size with a Volcano Explosivity Index (VEI) of 3 out of a maximum 7 (Major and Newhall, 1989). However, over $2 \times 10^7 \text{ m}^3$ of water was rapidly released from the volcano's ice cap and lahars flowed down five heavily populated river valleys. The combination of volcanic activity, extensive snow/ice cover, and poorly situated population areas led to a death toll of over 20,000 people (Pierson et al., 1990).

According to the AVO eruption database, 34 of the approximately 222 confirmed Alaskan eruptions within historical time (approximately between 1750 and 2013) have resulted in the formation of lahars (Alaska Volcano Observatory, 2014). We analyze the snow/ice cover at two different Alaskan volcanoes that have had lahar-producing eruptions due to melting of snow/ice: Redoubt volcano and Pavlof volcano (Figure 3.1). In our study, snow/ice cover area maps are generated for subsetting areas surrounding both of these volcanoes in order to spatially identify the surficial extent of seasonal snow, perennial snow, and glacial ice (Figures 3.2 and 3.3). With snow/ice area maps produced during quiescent time periods, we analyze the 2009 Redoubt eruption and 2013 Pavlof eruption, with a focus on linking the volcanic products spatially with underlying snow/ice cover type and analyzing how the spatial extent of snow/ice changes during and after an eruption.

3.2.4 Influence of snow/ice substrate type on lahar generation

While the type of volcanic product is important to lahar generation, more attention must be paid to identifying how the type of snow/ice cover can influence the efficiency of meltwater generation at an active volcano. Preliminary experimental attempts to analyze the movement of a hot grain flow over a snow layer on a sloped surface by Walder (2010) have shown that, when meltwater is allowed to escape without resistance from the base of the layer of snow, no slurry of meltwater and debris is formed. However, blockage of meltwater drainage causes instability and mobilization of the snow layer, resulting in slurry formation when mixed with the hot grains. Although this experimental design suffers from scaling issues, these concepts can increase the understanding of what happens when a pyroclastic density current flows over snow/ice cover during a real eruption. For instance, a layer of ice within a snowpack could block the drainage of meltwater resulting from the occurrence of a PDC and be a catalyst for lahar formation (Walder, 2010).

3.3 Background on Redoubt volcano

3.3.1 Setting of Redoubt volcano

Redoubt (Figure 3.2) is an andesitic to dacitic stratovolcano located on the western bank of Cook Inlet and approximately 175 km southwest of Anchorage, the largest city in Alaska. With a summit approximately 3,110 m asl, Redoubt is largely covered by glacial ice and perennial snow. The Drift glacier begins within the northern

rim of Redoubt's summit crater and widens along the northern flank of the volcano, ending in a piedmont lobe at the head of the Drift River valley (Bull and Buurman, 2013). The Drift River then flows east, confined mostly within braided channels of the Drift River valley before entering a broader, tidal flat region within the coastal plain of Cook Inlet (Waythomas et al., 2013). A seven-tank oil storage facility, the Drift River Oil Terminal (DROT), sits at the base of the Drift River valley, approximately 45 km east-northeast of the volcano (Miller and Chouet, 1994; Schaefer, 2012).

3.3.2 Recent eruptions at Redoubt volcano

Due to its location within Cook Inlet, Redoubt volcano is monitored by AVO with daily checks of satellite imagery, webcam imagery, and real-time seismic data (Bull and Buurman, 2013; Power et al., 2013). Additionally, periodic campaign geodetic surveys and airborne gas measurements are made in order to supplement daily monitoring efforts (Bull and Buurman, 2013). In the past fifty years (1963 – 2013), Redoubt has had three eruptions, all explosive in nature with a VEI of 3 (Waythomas et al., 2013). The most recent eruption occurred over a 4-month time span in 2009 beginning with a small phreatic eruption on March 15. The explosive phase of the eruption was characterized by 19 discrete explosive events between March 22, 2009 and April 4, 2009, producing at least five pyroclastic density currents and over 20 separate lahars (Waythomas et al., 2013).

Lahars inundated the largest cumulative areas on March 23 and April 4, 2009, inundating a total cumulative area of 100 km² and 125 km² respectively. While the two

significant lahars on March 23 were formed when an explosive eruption blasted through the summit snow and ice, the larger lahar on April 4 was formed when pyroclastic density currents swept down the Drift Glacier (Waythomas et al., 2013). Effusive activity dominated after April 4, 2009 with the slow extrusion of a summit lava dome that reached a volume of $72 \times 10^6 \text{ m}^3$ by the end of the eruption on July 1, 2009 (Diefenbach et al., 2013).

3.3.3 Eruption effects on Drift Glacier

With the active vent located underneath summit glacial ice, the 1989 eruption of Redoubt volcano resulted in destruction of approximately $113 \text{ to } 121 \times 10^6 \text{ m}^3$ of perennial snow and ice (Trabant et al., 1994). Throughout the largest explosive events over the course of three months (from December 14, 1989 to March 14, 1990), the head of the Drift Glacier was completely removed and flooding of the Drift River channel occurred up to 40 km away from the volcano (Miller and Chouet, 1994; Trabant et al., 1994). Although the majority of snow/ice lost during the 1989-1990 eruption was removed from the Drift Glacier and the area immediately downstream from the glacier, the seasonal snow present within the Drift River valley contributed $35 \times 10^6 \text{ m}^3$ of meltwater (Trabant et al., 1994). The lahars that formed during the 1989 – 1990 eruption are believed to be due to hot volcanic flows moving over the snow/ice surface, rather than from meltwater stored underneath the glacier (Trabant et al., 1994). Also observed in the 1989 – 1990 eruption was the deposition of a very unusual flow within the Drift River valley. This was composed of clasts of glacier ice and smaller pieces of rock debris that

are supported in a matrix of ice and snow grains, coarse ash, and frozen pore water (Waite et al., 1994; Waythomas et al., 2013).

Snow and ice lost from the Drift Glacier in the 2009 eruption was estimated to be along the same magnitude as that lost in 1989-1990. During the explosive phase of the eruption (March 22 - April 4, 2009), a total ice volume of $1 - 2.5 \times 10^8 \text{ m}^3$ was removed from the glacier (Waythomas et al., 2013). The volume lost during the explosive phase of the 2009 eruption was approximately equivalent to a decrease in the Drift Glacier's volume by 10 – 25%, while the volume lost in 1989-1990 was closer to 30% of the total glacier (Waythomas et al., 2013). In addition to snow/ice lost during the explosive phase of the eruption, there was an eight month precursory period with noticeably increased melting of snow/ice at the volcano's summit from July 2008 through the first explosive eruption on March 22, 2009 (Bleick et al., 2013). Melt features observed during this precursory phase included ice cauldrons, general ice subsidence, steam holes, and an increase in glacial crevasses (Bleick et al., 2013).

3.3.4 Lahar hazards at Redoubt volcano

One of the characteristics that makes Redoubt volcano unique within a context of Alaskan volcanoes is that there is an oil terminal less than 45 km downstream from its summit. Located on the coastal plain at the base of the Drift River valley, the Drift River Oil Terminal has the capacity to hold over one million barrels of oil produced from the western coast of Cook Inlet (Schaefer, 2012). This facility also maintains buried pipeline that extends northwest under the Drift River and Drift River valley (Waythomas et al.,

2013). During the 1989-1990 explosive eruption of Redoubt volcano, the DROT was heavily inundated by lahars, causing the precautionary removal of 6 million gallons of crude oil and the evacuation of facility personnel (Bull and Buurman, 2013). In 2009, operations were suspended and personnel evacuated after the first set of explosive, lahar-producing eruptions on March 23. Lahars flooded the terminal with mud and debris reaching as much as 1.5 meters up exterior building walls and covering the nearby terminal airstrip (Schaefer, 2012). These March 23 lahars contained a significant proportion of ice, believed to be derived from the summit crater, the Drift Glacier, and the seasonal snow and frozen Drift River within the valley (Waythomas, 2014). After the largest lahar on April 4, all facility personnel were evacuated and contingency plans were made to remove the remaining crude oil stored at the terminal (Schaefer, 2012).

3.4 Background on Pavlof volcano

3.4.1 Setting of Pavlof volcano

Pavlof volcano (Figure 3.3) is a mostly basaltic stratovolcano located 965 km west of Anchorage on the Alaska Peninsula. The summit of Pavlof is approximately 2,518 m asl and the flanks of the volcano are largely covered by glacial ice and perennial snow (Roach et al., 2001). In addition, there may be as much as 2 km³ of debris-covered glacial ice along Pavlof's flanks (Waythomas et al., 2006). Pavlof is one of six stratovolcanoes located within the Emmons Lake volcanic complex and has erupted at least forty times since 1790, making it the most historically active volcano in Alaska

(Waythomas et al., 2006). Previously erupted pyroclastic materials, lahars, and lava flows extend to low-lying areas on both the eastern and western flanks of the volcano. To the east of the summit, Holocene-age lava flows have been emplaced within 10 km of the summit while extensive historical lahar deposits can be found up to the coastline of Pavlof Bay, nearly 12.5 km east of the summit (Waythomas et al., 2006). The western flank of the volcano is characterized by Holocene-age lava flows within approximately 6 km of the summit, scattered pyroclastic deposits, and extensive historical-age lahar deposits (Waythomas et al., 2006).

3.4.2 Recent eruptions at Pavlof volcano

The eruptions at Pavlof have typically been VEI 3 or smaller and have lasted from several days to a couple of months (McNutt, 1987). Shorter duration eruptions have typically been magmatic in nature with longer eruptions having a more phreatic-phreatomagmatic component (McNutt, 1987). Eruptions from Pavlof have predominately included episodes of Strombolian fountaining that occur between varying lengths of repose periods (Roach et al., 2001). This Strombolian activity often produces a spatter rim along the summit vent with spatter-fed lava flows traveling a limited distance down the flank of the volcano (Waythomas et al., 2006). If this spatter rim collapses, trapped hot ash and gases can be released and form pyroclastic density currents that could travel 5 – 10 km down the flank of the volcano (Waythomas et al., 2006). A larger ash-producing event from Pavlof could result in a collapse of the ash column, forming pyroclastic density currents that could move further into low-lying valleys and drainages

(Waythomas et al., 2006). The last three eruptions at Pavlof (1996, 2007, and 2013) have all included periods of Strombolian fountaining at the summit which produced spatter-fed lava flows (Roach et al., 2001; Waythomas et al., 2008; Alaska Volcano Observatory, 2014). Lahars were also formed during each of these three recent eruptions at Pavlof. In 1996, collapse of the spatter rim at the summit formed pyroclastic density currents that melted the underlying snow/ice cover and produced lahars in the drainages to the north of the volcano (Waythomas et al., 2006). The 2007 lahars traveled down the southern flank of the volcano towards Pavlof Bay and resulted from hot avalanches due to the collapsing fronts of spatter-fed lava flows (Waythomas et al., 2008).

3.4.3 Lahar hazards at Pavlof volcano

Lahars have been a byproduct of many eruptions at Pavlof, evidenced by the Holocene and historical lahar deposits contained within the main drainages surrounding the volcano (Waythomas et al., 2006). The most likely eruption scenario leading to lahar formation at Pavlof is pyroclastic density currents sweeping down the snow and ice covered flanks of the volcano, causing some ratio of meltwater and loose debris to form (Waythomas et al., 2006). Unlike Redoubt volcano, a lack of infrastructure within the area means that the ground-based hazard of lahars at Pavlof is low. However, lahars could pose a hazard to any visitors in the low areas or drainages surrounding Pavlof (Waythomas et al., 2006). The orientation of lava flows and lahars from Pavlof is determined by the location of the active vent. For instance, in 1996 and 2013, the active vent was located on the north-facing flank of the volcano while the eruption in 2007 was

characterized by a vent on the southern flank (Waythomas et al., 2006, 2008). It is also possible for activity to occur from multiple summit vents, causing lava flows, pyroclastic density currents, and lahars to form down more than one flank during an eruption (Waythomas et al., 2008).

3.5 Methods

We produced three different products for both Redoubt and Pavlof volcanoes. Product 1 consists of individual snow/ice cover area maps of eleven images for Redoubt volcano and thirteen images for Pavlof volcano. The eleven images of the Redoubt subset were acquired prior to the 2009 eruption between the months of May and September. The thirteen images used to study the snow/ice cover on Pavlof volcano were acquired prior to the 2013 eruption and span the months April through August, and October. Product 2 consists of snow/ice area maps summarizing the snow/ice that is consistently present at each volcano during at least two different years throughout the Alaskan summer months. Product 3 includes composite maps of the eruptive products produced during the 2009 eruption of Redoubt and 2013 Pavlof eruption. The map of these volcanic products will be combined with the snow/ice cover information obtained from Products 1 and 2. We do not study the detailed formation process for these volcanic products. Instead, we correlate the distribution of these products with the snow/ice cover maps in order to assess the predictive capability of quiescent snow/ice cover maps for future eruptions. Where

possible, Product 3 will compare the visible snow/ice cover area after the eruption with the snow/ice cover expected from the snow/ice cover summary maps.

3.5.1 Sensors used to create Products 1, 2, and 3

In satellite remote sensing, there is a trade-off between high spatial resolution and high temporal resolution. Many global coverage maps of snow/ice used for daily monitoring purposes use the visible bands of lower spatial resolution sensors such as the NOAA Advanced Very High Resolution Radiometer (AVHRR) with a 1.1 km spatial resolution at nadir and the NASA Moderate-Resolution Imaging Spectroradiometer (MODIS) sensor with a 250 – 1 km spatial resolution at nadir (Hall et al., 1998; Xiao et al., 2001). These low spatial resolution sensors are also used for monitoring volcanic activity due to the multiple repeat passes they make per day (Dean et al., 2004). Multiple repeat passes per day are particularly necessary to monitor activity in Alaska, as heavy cloud cover can commonly block views of the volcano (Dehn et al., 2002). However, high spatial resolution is sacrificed for this daily access to data. The purposes of this study are not to monitor the daily changes at Redoubt and Pavlof volcanoes but to map the snow/ice cover over a range of years and pair that information with the spatial distribution of eruptive products from the most recent eruptions of both volcanoes. While the use of MODIS or AVHRR may work effectively for large ice sheets such as those in Greenland, the ability to detect smaller snow/ice covered areas will be diminished with these low spatial resolution sensors (König et al., 2001). The coarse spatial resolution of the AVHRR and MODIS sensors is sufficient to identify the presence of ash plumes and

elevated surface temperatures at an active volcano (Webley et al., 2013). However, while AVHRR and MODIS can detect the presence of lava or other hot deposits along the flank of the volcano (Dehn et al., 2000), they do not have the spatial resolution necessary to adequately map the finer spatial distribution of these deposits (Dehn et al., 2002). For the purposes of this study, six high spatial resolution sensors will be used to map the snow/ice cover and eruptive deposits at Redoubt and Pavlof volcanoes (Table 3.1).

3.5.2 Methods used to produce Product 1: individual snow/ice cover maps

The methods we use to map the snow/ice cover at individual images for both Redoubt and Pavlof volcano are discussed in Rahilly et al. (in review). The group of images for each volcano are subsetting to the same spatial area in order to compare the snow/ice cover percentages across image dates. Additionally, only images that are mostly-cloud free are used so that snow/ice cover pixels are not obscured by cloud cover.

The subset for Redoubt includes both the volcano and the Drift River valley from the headwaters at the base of the volcano to the delta region along the coast of Cook Inlet (Figure 3.2). The Pavlof subset (Figure 3.3) is a rectangular area approximately 145 km² in size and stretches from the coast of Pavlof Bay southeast of the volcano past the historical-aged lava flows and lahars to the northwest of the volcano. Inspired by the study by Rivera et al. (2006), the snow/ice cover was also mapped for a Pavlof Sister subset of similar spatial extent (Figure 3.3). Pavlof Sister is a 2,142 m asl stratovolcano located east of Pavlof volcano. Pavlof Sister is also covered by snow and ice, however, this volcano has never had an eruption within historical time (Waythomas et al., 2006).

Similar to the study comparing Villarrica and Mocho volcanoes in Chile (Rivera et al., 2006), Pavlof and Pavlof Sister can be assumed to be within the same climate regime but have a widely different eruptive history (Waythomas et al., 2006). Snow/ice cover area within the Pavlof subset is compared directly to the area of snow/ice cover within the Pavlof Sister subset. This allows for analysis of how the ratio between Pavlof and Pavlof Sister snow/ice cover area varies throughout the Alaskan summer melt season.

A variety of methods can be used to map the snow/ice cover present in each image, however, the most efficient and effective method was shown to be use of a linear spectral unmixing analysis (Rahilly et al., in review). The resulting snow/ice maps for each individual image (Product 1) produced using the linear spectral unmixing analysis method include percentages of snow/ice present along with root mean square (RMS) error information for each pixel in the image. Total snow/ice cover area can then be compared across images for each volcano. Additionally, within Product 1, is an analysis of the reappearance of seasonal snow after the end of the ablation season, referred to as the first fresh snowfall. A range of dates for the first fresh snowfall were approximated for multiple years using available satellite views of the two volcanoes. If possible, exact dates of the first fresh snowfall could be found for Redoubt volcano using the AVO webcam “Juergen’s Hut”, located approximately 11 km north of the volcano (Bull and Buurman, 2013).

3.5.3 Methods used to produce Product 2: snow/ice cover summary maps

Many previous efforts to map snow/ice cover have focused on examining a single satellite image acquired at the end of the ablation season, in August in the northern

hemisphere and February in the southern hemisphere (Boresjö Bronge and Bronge, 1999; Sidjak and Wheate, 1999; Xiao et al., 2001). In these studies, the purpose of using images acquired at the end of the ablation season is to remove the influence of seasonal snow. However, the purpose of our study is to create a product useful for hazard analysis at active volcanoes and therefore, snow/ice cover maps must be made from multiple months and over a number of years (Wessels et al., 2007). The reason for this is that seasonal and perennial snow can also be contributors of hazardous melt water during an eruption, as was observed in the 1989-1990 eruption of Redoubt volcano (Trabant et al., 1994). Mapping the spatial and temporal variability of snow/ice during the Alaskan ablation season (approximately May to August) results in a record of: 1.) average seasonal snow melt trends in the Redoubt and Pavlof areas during the ablation season; 2.) when the areas of interest are free of seasonal snow/ice; and 3.) the limit between glacial ice/perennial snow and seasonal snow.

The individual image snow/ice cover maps from Product 1 are intersected to make snow/ice cover summary maps throughout the Alaskan melt season. The snow/ice present in each individual image will be intersected in order to map the snow/ice that is consistently present during at least two different years for that month. For Redoubt volcano, the monthly snow/ice area maps will be from May through September while Pavlof volcano will have summary maps from April through August and October. Images from consecutive years were not available for each month, however, the intersected snow/ice consistently present during two different years at the end of the ablation season

should represent an estimation of the spatial extent of perennial snow and ice (Watanabe, 1988).

The images we selected have only patchy clouds covering less than 30% of the snow/ice pixels, meaning that the majority of the area of interest is cloud free. This feature was an important factor for image selection in order to create the most accurate map of the snow/ice cover actually present on the ground. Although limited in spatial extent, the possible differing cloud cover among images must be recognized. We achieved this by manually mapping the areas of snow/ice believed to be under patches of cloud cover by examining nearby snow/ice regions and utilizing band ratioing and image stretching to enhance the image contrast in order to see snow under thin cloud cover. Another extraneous feature that can vary strongly between images is the presence of stripes in Landsat 7 ETM+ images acquired after the satellite's scan line corrector (SLC) failed on May 31, 2003 (Maxwell et al., 2007). Stripes in the snow/ice cover area in Landsat 7 SLC-off images were manually filled, visually interpreting and expanding the surrounding snow/ice to make a close-approximation of the pixels that would be mapped within these striped areas.

3.5.4 Methods used to produce Product 3: composite maps of eruptive deposits and snow/ice cover

The last objective for this study is to spatially map the volcanic products generated in the 2009 Redoubt and 2013 Pavlof eruptions with underlying snow/ice cover type within the subset of each volcano. While an in depth analysis of the mechanisms for

deposit emplacement is beyond the scope of this study, Product 3 will serve as an example of how the maps created in Products 1 and 2 can be used to analyze an active eruption within a snow/ice cover focus. By spatially correlating the type of volcanic deposit and general type of snow/ice cover, we set the stage for future analysis of the role snow/ice morphology may play in lahar generation (Walder, 2010).

All sensors previously summarized in Table 3.1 were used to map the volcanic products present on the flanks of both volcanoes throughout the eruptions. Similar to the mapping of snow/ice cover, the methods of principal component analysis (PCA) and linear spectral unmixing analyses will be used to identify the volcanic products. Additionally, when available, web camera images from the AVO database, Volcano Activity Notices and Weekly Summaries issued by AVO, ash advisories, and pilot reports will be used to supplement optical satellite imagery. Although direct field-based observations are beyond the scope of this study, field-based geologic maps and observations are used as ground reference for delineation of volcanic products (Bull and Buurman, 2013; Waythomas et al., 2013).

3.6 Results and discussion

3.6.1 Product 1: individual snow/ice cover maps of Redoubt subset

The individual images selected for the Redoubt subset were acquired between the months of May and September in order to track the melt of seasonal snow during the Alaskan summer months. The snow/ice cover area of eleven individual images for the

Redoubt subset is shown in Figure 3.4. The often heavy cloud cover along the Alaskan coast makes the acquisition of completely cloud-free imagery a challenge. In order to obtain at least two images per month from May to September, estimation of snow/ice area under cloud cover was necessary in four out of eleven of the images analyzed. Snow/ice under clouds in these images is estimated using visual interpretation and accounts for less than 30% of the total snow/ice cover within the image. As this method introduces an aspect of analyst interpretation, the area of snow/ice estimated under cloud cover is indicated in Figure 3.4 by the blue portions of the data bars for the four images where this technique was necessary.

Analysis of images from the same month reveals a reduction in snow/ice cover area from the beginning to the end of the month, as expected with further time into the ablation season before the reappearance of fresh seasonal snow. Another expected conclusion revealed by Figure 3.4 is a variance between years. For example, the two images from August were taken at around the same time in the month yet the snow/ice area in 2008 was larger than that of the previous year by approximately 22 km^2 . A similar variance exists in the two September images, with the snow/ice area in 2008 approximately 26 km^2 larger than that in September of 2007. Despite these variations, the overall trend of seasonal snow melt from May to September remains consistent between years. Near-daily temperature data for the Redoubt area is available using the University of Alaska Fairbanks Geophysical Institute's extensive database of AVHRR temperature data. As prescribed by the methods in Dehn et al. (2000), the daily maximum band 3 (mid-infrared) temperature in nighttime, cloud free images was acquired over a 11 year

period from 2000 – 2011 for a 1,936 km² area surrounding Redoubt volcano. Seasonal variations in these temperatures can be seen, as well as extended periods of elevated temperatures representing volcanic activity (Dehn et al., 2000). An approximation of the temperature trends for this area over 11 years shows that there are no significant outlying years that were drastically warmer or colder, although note that there are fewer images available from 2000 to approximately 2005 (Figure 3.5).

The purpose of mapping the snow/ice cover in these images is to identify the seasonal pattern of snow cover within the Redoubt volcano subset (Figure 3.6). Satellite imagery from the Landsat and ASTER sensors was analyzed from 1999 through 2013 during the months of August through November to find clear views that could act as endmembers between which the first fresh snowfall occurred. With Redoubt volcano, daily images from AVO's "Juergen's Hut" webcam could be viewed starting in 2009 for identification of the exact date of the first fresh snowfall of the season. Between 1999 and 2013, all estimated first snow dates for the Redoubt subset occurred within the months of September (Julian Days 244-245 through 273-274) or October (Julian Days 274-275 through 304-305).

3.6.2 Product 2: snow/ice cover summary maps of Redoubt subset

For the Redoubt volcano subset, snow/ice cover summary maps are generated using the individual images from Product 1. The intersected snow/ice cover area per month represents the snow/ice consistently present across at least two years in that month and allows an observation of the overall trend of seasonal snow melt from May through

September (Figure 3.7). A very clear decrease in the amount of snow/ice within the Redoubt subset can be seen through September, right before the average reappearance of seasonal snow (Figure 3.6).

The average snow/ice area decrease occurring between months can be quantified by performing a percent variance calculation (Table 3.2). The decrease in surface area of snow/ice is consistent from May to June and June to July, with the area shrinking by approximately 22 to 23% each month with a total decrease in area of 44 km² and 37 km², respectively. The most drastic amount of melt in the Redoubt subset occurs between July and August, when the snow/ice area is decreased by 55% with a total area decrease of 67 km². Between August and September, approximately 31% of the remaining snow/ice area is further diminished with a decrease of 17 km².

Product 2 consists of both a quantitative and qualitative analysis of the snow/ice cover area summarized in each month for the Redoubt subset. Snow/ice cover summary maps for each month from May to September (Figures 3.8 and 3.9) illustrate the variations in seasonal snow cover within the Redoubt subset. For descriptive purposes, the Redoubt subset can be broken down into three separate regions: the Drift River valley, the piedmont lobe of the Drift Glacier, and the flanks and summit of the volcano (Figure 3.8A). These three regions are used to further analyze the snow/ice cover area for each month summary map. By May, the seasonal snow within the lower delta region of the Drift River valley has disappeared (Figure 3.8B) while the average snow/ice cover in June is limited to the upper headwater region of the Drift River (Figure 3.8C). The most interesting characteristic of the snow/ice cover area in the Redoubt subset can be seen

during the later months of the Alaskan summer (Figure 3.9). Beginning in July, the spatial limit of snow/ice cover can be seen regressing up in elevation towards the summit of the volcano, surpassing the outer reaches of the Drift Glacier piedmont lobe and perennial snow and ice along the volcano's flanks as reported by Bleick et al. (2013) (Figure 3.9A). The region of visible snow/ice then continues to move upwards in elevation towards the flanks and summit of the volcano in both August (Figure 3.9B) and September (Figure 3.9C). Observations of the piedmont lobe after both the 1966 - 1968 and 1989/1990 eruptions of Redoubt have shown that the piedmont lobe glacial ice was covered by extensive debris cover (Sturm et al., 1986; Trabant and Meyer, 1992). After the 1966 – 1968 jökulhlaups, the piedmont lobe glacial ice was observed to be covered by up to 5 m of sand and ash (Sturm et al., 1986). Additionally, Trabant and Meyer (1992) suggest that ash cover will affect the glaciers surrounding Redoubt volcano for several decades after the 1989-1990 eruption. In our study, this ash and debris cover is visible after the majority of seasonal snow/ice is removed from the Drift River valley and piedmont lobe area beginning in July (Figure 3.9A). The appearance of the Drift glacier and piedmont lobe after the 2009 eruption is further examined in Product 3.

The appearance of the debris covered piedmont lobe and flanks of the volcano can further be observed in imagery from the “Juergen’s Hut” webcam 11 km to the north of Redoubt (Bull and Buurman, 2013). AVO maintains a database of archived images from this webcam from 2009 to present with views of the volcano's summit, upper flanks, and the southern-half of the piedmont lobe. Figure 3.10 is a summary of webcam images acquired from May to September of 2012. Webcam images from this year were chosen to

be temporally removed from lingering influences of the 2009 eruption. Steaming can be seen at the summit in multiple webcam views (Figures 3.10A, 3.10B, 3.10D, and 3.10E), however this steaming is not necessarily anomalous and has appeared in multiple cloud-free webcam views of the summit in each year from 2009 through the present. Although the entire Redoubt study area cannot be seen, the webcam views in Figure 3.10 are remarkably consistent with the snow/ice cover summary maps produced for May through September. For instance, by the July webcam image, the majority of the visible snow/ice cover has extended up the flanks of the volcano, with only small patches of snow/ice visible within the piedmont lobe (Figure 3.10C). This is exactly what was observed beginning with the July snow/ice cover summary map and more extensively in the August and September summary maps (Figures 3.9A, 3.9B, and 3.9C). By the August and September webcam images, the visible snow/ice has moved up onto the flanks of the volcano (Figures 3.10D and 3.10E). The area of snow/ice cover in these images appear to be similar but the influence of shadow in September appears to be greater as the sun appears lower in the sky during the early Alaskan fall. A greater influence of shadow on the flanks of the volcano could have possibly caused the decrease in snow/ice area observed from August to September in summary maps. This is because extensive shadow consistently decreases the effectiveness of snow/ice mapping using the linear spectral unmixing method (Rahilly et al., in review).

3.6.3 Product 3: composite maps of eruptive deposits and snow/ice cover of Redoubt subset

The 2009 eruption of Redoubt volcano and the deposits that resulted from it have been extensively studied by previous researchers (Schaefer, 2012; Bull and Buurman, 2013; Wallace et al., 2013; Waythomas et al., 2013; Webley et al., 2013). Seven images acquired before, during, and after the eruption (approximately March 15 – April 4, 2009) have been analyzed for snow/ice cover changes and deposits emplaced at Redoubt volcano (Table 3.3). Our study does not analyze every deposit produced during the eruption, but will focus on the deposits visible in satellite imagery between March 26 and April 4.

In order to fully analyze the snow/ice cover and deposits present in the imagery available directly before, during, and after the eruption, a summary of the events that occurred between image acquisitions is needed. Table 3.3 further summarizes the main deposits and fresh snow fall occurring between images. A daily supply of high spatial resolution, cloud-free imagery is not available for this eruption and therefore the deposits and snow/ice cover observed within an image are often the products of multiple events. For our study, the most pivotal pieces of information needed between two image dates are the deposit types produced and whether fresh snow has fallen. Analysis of snowfall events was completed using imagery from the AVO's "Juergen's Hut" webcam and was often observed as fresh snowflakes on the camera lens. This method is limited, however, in that snowfall occurring overnight cannot be observed, although new snow deposits on older deposits can provide information on unobserved snowfall events.

The first part of analysis to generate Product 3 is to record the snow/ice present within the Redoubt subset as close to the start of the eruption as possible. This can be performed using the Landsat 7 image acquired on March 18, 2009 (Table 3.3). The events that occurred around the acquisition date of this image include a phreatic eruption on March 15 that produced an ash-bearing plume that propagated southeast from the volcano with a maximum height of approximately 4 km above the summit (Wallace et al., 2013, Webley et al., 2013). Ash was deposited to the south of the volcano for a distance of about 1.5 km (Bull and Buurman, 2013). A hole in the glacier was formed as a result of the phreatic explosion and meltwater flowed down the Drift Glacier gorge (Bleick et al., 2013). Fresh snow fall was then observed in webcam imagery from March 16 and possibly again on March 17. The March 18 Landsat image is a local-winter image and therefore the surficial covering of seasonal snow does not allow for discriminating between glacial ice, perennial snow, and seasonal snow. However, the snow/ice cover at Redoubt has been extensively studied in Products 1 and 2. These are then used to estimate the surficial extent of perennial snow and ice underneath a covering of surficial snow in the March 18 image (Figure 3.11). Here, the snow/ice cover underneath the surficial cover of seasonal snow has been approximated. The greatest area of snow/ice cover in the March 18 image is seasonal snow over Drift River valley alluvium or bare rock. Using Product 2, the snow/ice cover present at the end of the ablation season is approximated as the extent of perennial snow and glacial ice. The maximum extent of perennial snow and ice is less than that mapped by previous researchers (Trabant and Hawkins, 1997; Bleick et al., 2013). As seen in the snow/ice cover maps for Redoubt in Product 2, although the

piedmont lobe has been mapped as glacial ice by previous studies (Trabant and Hawkins, 1997; Bleick et al., 2013; Bull and Buurman, 2013; Waythomas et al., 2013), it was not mapped within the visible snow/ice cover area beginning in July. The difference between the perennial snow and glacial ice mapped by Bleick et al. (2013) and that mapped by our study is outlined as debris-covered perennial snow and ice in Figure 3.11. The total area of this debris-covered snow/ice is approximately 59 km². Finally, areas of exposed rock within the March 18 image have been mapped.

Figure 3.11 is an example of how the snow/ice cover maps created in Product 2 can be modified for the closest images to the start of the eruption. Examples of how the exposed snow/ice can change during an eruption are shown for Redoubt volcano in Figures 3.12 through 3.15 with the lahar deposits produced from March 26 through April 4, 2009. Three cloud-free images were acquired on March 26, April 1, and April 4. Unfortunately, cloud-free imagery between March 18 and March 26 are not available.

The image acquired on March 26 is mostly cloudy (Figure 3.12A). By performing a principal component analysis (PCA) in order to highlight the spectral variances within this image, we can distinguish and manually map the lahar deposit underneath the thinner cloud cover (Figure 3.12B). This was possible for approximately half the Drift River valley, as the lower delta area of the river is covered by a thick blanket of clouds. Nine lahars were recorded, mostly using seismic data, on March 22, March 23, and March 24 (Table 3.3) (Bull and Buurman, 2013). An additional four lahars were recorded before the Landsat image was acquired on March 26. Out of the 13 lahars that occurred prior to image acquisition, the lahars on March 23 and March 26 were the largest. The lahars on

March 23 are believed to have eroded portions of the valley floor and the flows followed the main Drift River channel (Waythomas et al., 2013). Fresh snowfall on March 25 (Table 3.3) and the absence of imagery between March 18 and March 26 make it difficult to determine which lahar deposits came from which day. The visible lahar channels in this March 26 image cover an area of approximately 16.4 km^2 , however this does not include the lahar channels hidden beneath cloud cover in the lower Drift River valley (Table 3.4).

Approximately 20 lahars occurred between March 26 and the acquisition of the ALI image on April 1 (Table 3.3). Fresh snow occurred at least on March 27 and again by March 30, where fresh snow was seen in webcam imagery covering lahar deposits in the upper Drift River valley (Figures 3.13A and 3.13B). Additionally, tephra fall occurred over the Redoubt subset on March 27 and March 28, resulting in grey, ash covered snow visible in the ALI image from April 1 (Figure 3.13C). A total area of approximately 16.6 km^2 of lahar channels were manually delineated using a PCA image (Table 3.4). The lahars from individual days between March 26 and April 1 could not be uniquely identified (Figure 3.13D) but it is clear that the March 30 fresh snow fall did not decrease the visibility of the lahar channels in the PCA image.

Large lahars on April 4 were formed as a result of collapse of the lava dome at the summit of the volcano that sent hot pyroclastic density currents over the Drift Glacier (Waythomas et al., 2013). The lahar covers the entire width of the Drift River valley with dark lahar deposits in the natural color image from April 4 (Figure 3.14A). However, a PCA of the lahar deposits reveals numerous braided channels that cover an area of

approximately 23.3 km² throughout the entire valley (Figure 3.14A insert and Table 3.4). If the lahars that occurred on April 4 propagated down the Drift River valley through this network of braided channels (Figure 3.14B), the valley lahar deposits may assist in identifying areas of maximum erosional and depositional forces. Similar to braided river systems, the channels represent areas of erosion while the bars, or areas between the channels, represent overbank depositional environments of finer grained sediments (Procter et al., 2010).

An in-depth analysis of the mechanisms for lahar formation during the 2009 eruption of Redoubt are beyond the scope of this study. However, we ask how the deposits within the valley early in the eruption influence the percentage of deposits that flow over snow/ice later in the eruption? For instance, by comparing the lahar channels from April 4 with those channels already in the valley from March 26 through April 1, it is possible to determine the percentage of lahars that flowed down previous lahar channels filled with old deposits and the amount of lahar mud that traveled through newly-made channels (Figure 3.15). This is significant, especially within the highly erosive channel areas, because previous deposits will affect how well any underlying snow/ice cover will be insulated against melt from fresh deposits with elevated temperatures (see Edwards et al., 2012). The majority of lahar channels were created on April 4 with only approximately 38% of the total lahar channel area (8.8 km²) intersecting channels from March 26 through April 1 (Table 3.4). An additional factor to consider is that the area around Redoubt volcano was covered by ashfall during multiple explosive events with many of the ashfall deposits interbedded in between layers of fresh

snowfall (Wallace et al., 2013). Therefore, the remaining 62% of the channels, or an area of approximately 14.5 km^2 , were created through seasonal snow interbedded with ash layers of varied thicknesses. Further work is required to determine how this interbedding affects the melting properties of seasonal snow. This percentage of reused channels to newly formed channels is similar to the channels observed in the April 1 ALI image, where 30% of the lahar channels (5 km^2) followed the same path as those mapped in the March 26 image (Table 3.4). These numbers are an approximation due to the lack of imagery taken close enough to the March 23 and 24 lahars. However, the large lahars on March 23 were observed by other researchers to follow the main Drift River channel (Waythomas et al., 2013). This channel became choked with lahar mud and caused future channels to be diverted elsewhere, although there was some intersection between the April 4 lahar channels and the main Drift River channel (Figure 3.15).

In order to create a map that would be useful for further analysis into the role snow/ice cover type plays in an eruption, the lahar channels observed on March 26, April 1, and April 4 are spatially linked to the underlying snow/ice cover type. The high spatial resolution imagery available for the 2009 eruption presents some major limitations to fully mapping the deposits with snow/ice cover. The area along the immediate flanks of the volcano is largely outside the image area for both the April 1 and April 4 ALI images (Figures 3.13 and 3.14). While the summit and flanks of the volcano are partly observable in the March 26 image, the lower half of the Drift River valley is completely obscured by thick clouds (Figure 3.12). When spatially mapping the lahar channels with underlying snow/ice cover, the majority of channels propagated over seasonal snow

within the Drift River valley (Table 3.4). The lahar channels observable on March 26 intersected only approximately 3.6 km^2 of the piedmont lobe glacial ice. However, the majority of the pyroclastic density currents were localized within the summit and flanks of the volcano, being largely funneled down the Drift Glacier gorge (Bull and Buurman et al., 2013). The majority of the lahars at Redoubt are formed when pyroclastic density currents erode glacial ice and seasonal snow is further entrained within the lahars as they move down the valley (Trabant et al., 1994; Waythomas et al., 2013). Our study presents a number of additional questions related to this process of seasonal snow melt. Could the channels mapped in our study be the localized areas where the seasonal snow in the Drift River valley is eroded and entrained in the lahars? How would the lahar volumes be different during an eruption after June, when the seasonal snow in the valley is at a minimum?

Finally, the snow/ice cover present within the Redoubt subset in the months and years after the eruption can be compared to the monthly summary maps made in Product 2 (Figure 3.16). The three mostly cloud-free images available close after the eruption were from May 13, July 8, and September 26, 2009. The visible snow/ice cover from May 13 is almost non-existent, with ash and other deposits covering the majority of snow/ice within the valley and along the flanks of the volcano (Bull and Buurman, 2013; Wallace et al., 2013; Waythomas et al., 2013). Multiple fresh snowfall events occurred after the end of the explosive eruption on April 4. However, by the time the image was acquired on May 13 most of this superficial fresh snowfall had melted, once again revealing the ash covered flanks of the volcano (Figure 3.17).

This is also the case for the image from July 8, however with fresh snow present at the summit of the volcano after an episode of fresh snow on May 19, 2009 as seen in webcam imagery. By September 26, extensive fresh snow can be seen along the flanks of the volcano. The first fresh snowfall date in 2009 was earlier than average, as reflected by the higher than average snow/ice area when compared to the September summary snow/ice area. Two additional images from 1 – 2 years after the eruption were also examined in order to identify if the eruption had a longer lasting influence on the spatial extent of snow/ice cover. Both the image from July 11, 2010 and the image from August 15, 2011 contained a smaller area of snow/ice cover than usual for their respective months (Figure 3.16).

3.6.4 Product 1: individual snow/ice cover maps of Pavlof subset

The thirteen individual snow/ice cover maps of the Pavlof and Pavlof Sister subsets reveal a similar variation in snow/ice area from the beginning to the end of the month and between years as that observed at Redoubt (Figure 3.18). Only two out of the thirteen Pavlof subset images (July 6, 2004 and April 15, 2006) required an estimation of snow/ice area under cloud cover. As can be seen by the dramatic increase in snow/ice area between the August and October images, the image from October 19, 2007 was acquired after the first appearance of fresh snow. In fact, this was the first cloud-free satellite image after the local summer where fresh snow could be seen, setting the upper range for first fresh snowfall date (Figure 3.19). Unlike Redoubt volcano, there is no webcam set up with a view sufficient for identification of the exact first fresh snowfall

date at Pavlof volcano. Therefore, the ranges obtained from available cloud-free high resolution satellite imagery are used to approximate the first snow date as the median date between two endmember images. Additionally, note from Figure 3.19 that the largest gap in first snow dates is from 2001 through 2004, when there was a lack of cloud-free images acquired. Like Redoubt, seasonal and yearly temperature trends for the area surrounding Pavlof volcano were analyzed using AVHRR band 3 mid-infrared data from 2005 through 2013. These temperatures have an overall consistent yearly trend for this area, although 2005 appears to have been a slightly colder than average year (Figure 3.20).

The snow/ice area of the Pavlof subset can be analyzed from a different perspective by comparing it to the snow/ice area of the adjacent Pavlof Sister volcano (Figure 3.18). Both volcano subsets were acquired from the same image so that conditions such as solar elevation, satellite zenith, and atmospheric conditions are constant. Cloud cover did vary between the two subsets but to a limited extent. Only four of the thirteen Pavlof Sister images required estimation of snow/ice under cloud cover. However, the snow/ice area estimated under these conditions accounts for less than approximately 7% of the overall snow/ice cover area for each image of both Pavlof and Pavlof Sister.

From May through August, the snow/ice area within the Pavlof subset is consistently greater than that of Pavlof Sister (Table 3.5). Similar to observations of the Pavlof subset, there is a general decrease of snow/ice area at Pavlof Sister from the beginning to the end of each month during the ablation season months (the April through

August images). Variances between different years can also be seen, and the overall trend in these variances remains consistent with that seen at Pavlof volcano. For instance, the smallest snow/ice area seen in July at Pavlof is from the image acquired on July 6, 2004 and the largest snow/ice area is from July 4, 2006. This trend for July is the same for images of the Pavlof Sister subset.

This is a good indicator that both Pavlof and Pavlof Sister are influenced by the same regional climate and therefore the snow/ice cover may be compared without climatic influence as a variable, as prescribed by the methods established by Rivera et al. (2006). The percent variances reported in Table 3.5 show the greatest average difference between the snow/ice cover at the Pavlof and Pavlof Sister subsets occurs during the month of July. In the July 4, 2006 image there is approximately 75% more snow/ice area, equivalent to 15 km^2 , within the Pavlof subset than in the Pavlof Sister subset.

A variation in the overall trend observed during the Alaskan summer months can be seen at the edges of the ablation season in April and October. The images from April 2013 and October 2007 are timely in that both were acquired approximately one month before or after a major eruption at Pavlof volcano (Figure 3.18). The April 26 image was acquired before the beginning of the 2013 eruption on May 13 and the October 19 image was acquire after the end of the 2007 eruption on September 13, 2007. On April 26, the Pavlof Sister subset contained a greater area of snow/ice than the Pavlof subset. On October 19, the snow/ice area at Pavlof Sister was approaching the same value as that at Pavlof. At first glance, this may appear to suggest that the decrease in snow/ice area at Pavlof during these times was due to an increase in heat output at the volcano during a

period of elevated eruptive activity. However, further analysis of additional imagery from April 15, 2006 and October 21, 2008 show consistently larger snow/ice area within the Pavlof Sister subset during these times at the edges of the ablation season, suggesting that this effect is not volcanological in origin but related to the disappearance and reappearance of seasonal snow along the northwestern regions of both subsets (Figure 3.21). Here, a large variation in topography exists between the Pavlof and Pavlof Sister subsets. While over half the area of the northwestern edge of the Pavlof subset consists of the Cathedral Valley, this same region in the Pavlof Sister subset contains many high elevations that contribute to the later disappearance of seasonal snow in April (Figures 3.21A and 3.21B) and the earlier reappearance of fresh snow in October (Figures 3.21C and 3.21D).

3.6.5 Product 2: snow/ice cover summary maps of Pavlof subset

The monthly snow/ice cover area for the Pavlof subset was once again compared to that of the Pavlof Sister subset for the months of April through August and October. The overall trend of snow/ice variance seen in the individual images of Product 1 (Figure 3.18) can also be seen in Product 2 (Figure 3.22). From May through August, the Pavlof subset has a larger area of snow/ice cover than the Pavlof Sister subset. However, as observed in Product 1, seasonal snow disappears later from the Pavlof Sister subset in April and reappears earlier in October than from the Pavlof subset. Quantification of the snow/ice cover area changes in both subsets can be accomplished with calculation of the percent variance between months (Table 3.6). The largest decrease in snow/ice cover area

occurs within both the Pavlof and Pavlof Sister subsets between June and July.

Additionally, the reappearance of seasonal snow can be seen by the large percentage increase in snow/ice cover area in both subsets by October.

Snow/ice cover summary maps were also made for both the Pavlof and Pavlof Sister subsets (Figures 3.23 and 3.24). The small percent monthly decrease in snow/ice area for both volcano subsets between April and June can be qualitatively observed in the snow/ice cover summary maps for these months (Figure 3.23). Similar to the individual snow/ice cover images, in April the snow/ice cover can still be observed within the high elevation regions in the northwest end of the Pavlof Sister subset (Figure 3.23A). By May (Figure 3.23B) and June (Figure 3.23C), one of the largest differences between the two snow/ice cover areas can be seen along the northern edge of the Pavlof Sister subset (outlined by the yellow box in Figure 3.23B). This area is a drainage valley with headwaters from the summit of both Pavlof and Pavlof Sister that eventually empty into Divide Lake, approximately 10 km northwest of Pavlof Sister volcano. In fact, all of the smaller snow/ice-free areas of both volcanoes during May and June coincide with the location of drainages. In July (Figure 3.24A) and August (Figure 3.24B), the seasonal snow has nearly completely disappeared in all areas beyond the steep-sided slopes of the volcanoes. Previous researchers state that there may be as much as 2 km³ of debris-covered glacial ice along Pavlof's flanks (Waythomas et al., 2006). The July and August snow/ice cover summary maps for Pavlof illustrate the extent of some of this debris cover (yellow circled areas in Figures 3.24A and 3.24B). The extensive snow/ice free region directly northwest and southeast of the summit is heavily influenced by the August 2,

2008 image, where debris covers an area of approximately 2.5 km² at the summit. A similar region without snow/ice is not seen at Pavlof Sister, therefore this is neither a feature caused by the solar zenith of the image nor the shadows formed by the summit peak. The influence of heavy shadows from the summit due to a low solar zenith angle is seen as similarly shaped and sized regions without mapped snow/ice in the October summary maps of both the Pavlof and Pavlof Sister subsets (Figure 3.24C). The August 2008 image was acquired less than a year after the 2007 eruption of Pavlof. The summit debris cover could be remnant deposits from this 2007 eruption. In their field studies at Pavlof nearly 60 years ago, Kennedy and Waldron (1955) reported that a large proportion of volcanic ash was entrained in the glacier ice at the volcano, leaving a thin layer of ash that covers much of the glacier when melt water redistributes it in the summer. This suggests a possible method of emplacement for the debris cover seen in this August 2008 image. By the August 4, 2009 image, this same area is largely covered by snow. Whether this is due to a larger amount of seasonal snow in 2009 than 2008 is unknown. However, further analysis is needed using more cloud-free August imagery to examine if this debris cover is present in other years. No cloud-free images exist of the Pavlof summit at the end of the 2013 local summer. Further work is required to analyze any available cloud-free views of the summit in July and August 2014 in order to see whether the deposits from the 2013 Pavlof eruption contribute to debris cover on the perennial snow and ice.

The August map for the Pavlof subset represent the maximum removal of seasonal snow at the end of the ablation season (Sidjak and Wheate, 1999; Boresjö Bronge and Bronge, 1999; Xiao et al., 2001). The snow/ice present in both of these maps

can then be concluded to be the maximum extent of perennial snow and glacial ice present along the flanks of these volcanoes.

3.6.6 Product 3: composite maps of eruptive deposits and snow/ice cover of Pavlof subset

The 2013 eruption of Pavlof volcano lasted approximately 2 months from May 13 until the volcano returned to background levels of activity at the end of July 2013 (Alaska Volcano Observatory). Six satellite images were used to study the deposits and changing snow/ice cover throughout the 2013 eruption (Table 3.7). The main events from the 2013 Pavlof eruption are summarized around the available satellite imagery in Table 3.7 with the main deposit types produced being tephra fall, lava flow(s), possible pyroclastic density currents, and lahar(s) within the drainages northwest of the volcano. The eruption can be broken down into two phases: 1.) the activity from May 13 to May 19, 2013; and 2.) the activity from June 4 – June 28, 2013.

The significant high resolution satellite images available during the eruption are summarized in Figure 3.25 and show the main deposits present along the flanks of the volcano and the northwestern drainages throughout the 2013 activity. The multi-spectral Hyperion image acquired on May 16 (Figure 3.25A) shows two to three flows down the northwest flank of the volcano. The more northern flow has a maximum brightness temperature of 509°C and is likely a lava flow while the adjacent flow to the south has a maximum brightness temperature of approximately 380°C (Figure 3.25B). This southern flow may possibly be an older lava flow or a pyroclastic density current that has cooled. A low temperature flow with some proximal steaming was observed along the lower

reaches of the volcano's flank and may be meltwater generated from the deposits closer to the summit (Kaufman and Webley, 2013 personal communication). By May 19, 2013, extensive lahar deposits can be seen northwest of the volcano in a drainage that empties into the upper Cathedral Valley (Figure 3.25C). The thermal infrared bands for this image also show elevated surface temperatures with saturated pixels underneath the ash plume at the summit (Figure 3.25C insert). These saturated pixels represent the temperatures that are higher than the sensitivity level of the instrument (Ramsey and Dehn, 2004), a brightness temperature of approximately 370 K for ASTER TIR bands (Morissette et al., 2005). These saturated pixels represent temperatures greater than 100°C and outline the lava flow present along the northwest flank of the volcano on May 19 (Ramsey, 2013 personal communication). By acquisition of the ALI image on June 11, 2013, significant ash cover had occurred over both the flanks of Pavlof and Pavlof Sister volcanoes (Figures 3.25D, 3.25E, 3.25F). However, ash-free snow is present at the summit of Pavlof Sister volcano, meaning that fresh snowfall must have fallen at some point between the return of eruptive activity on June 4 and the ALI image on June 11. The Landsat 8 image acquired on June 28, 2013 (Figure 3.25G) appears to show a variation in the lahar deposits present within the northwestern drainage, suggesting the possible occurrence of more lahar(s) between June 4 and June 28. Further lava flows are present along the flank in this image as well as more southerly flows of unknown morphology on the flank. A flow with temperatures elevated above background is observable under cloud cover in the ASTER TIR night image from June 29, 2013 (Figure 3.25G insert). On both June 11 and June 28, Pavlof Sister volcano has a larger area of visible snow/ice cover than at Pavlof.

It is likely that the majority of snow/ice cover at both volcanoes is covered by ash. A summary of the major ash directions from May 13 through June 28 can be seen in Figure 3.26.

The deposits from Figure 3.25 are delineated and draped over maps of the snow/ice cover estimated to be in the Pavlof and Pavlof Sister subsets during the 2013 eruption (Figures 3.27 and 3.28). The closest cloud-free individual image prior to the beginning of the eruption was acquired on April 26, nearly three weeks before the first explosive event on May 13. For this reason, the snow/ice monthly summary map for May will be used to approximate the seasonal snow cover when the May volcanic deposits were produced (Figure 3.23B). Deposits produced during the second phase of the eruption are mapped onto the June monthly snow/ice cover summary map (Figure 3.23C). For both maps, the maximum extent of perennial snow and ice at the end of the ablation season is mapped using the August snow/ice cover summary map (Figure 3.24B). Due to cloud cover, it is not possible to fully map the extent of all the flows produced during the 2013 eruption. However, the deposits that are able to be mapped can be spatially linked to the underlying snow/ice cover (Figures 3.27 and 3.28).

The majority of the lava flows and possible pyroclastic density current flows propagated over the debris-covered snow/ice area discussed earlier within the context of the August snow/ice summary map. In the May 16 image, an area of only 0.03 km^2 intersected with perennial snow and ice, comprising only 15% of the total 0.2 km^2 flow area (Figure 3.27 insert and Table 3.8). A larger portion of the possibly cooled lava or pyroclastic density current from this May 16 image propagated over perennial snow/ice.

The lahar flow(s) mapped in the May 19 ASTER image cover an area of approximately 4.3 km². The lahar(s) flowed over 3.5 km² of seasonal snow within the valley northwest of Pavlof, with the remaining 0.7 km² flowing through snow-free drainages into the Cathedral Valley. Approximately 30% of the lava flow area observed in June 28 flowed over perennial snow and ice, an area equivalent to 0.1 km² (Figure 3.28 and Table 3.8). Similar to the analysis performed on the lahar channels at Redoubt volcano, the area of flows that propagated over older deposits was calculated. Only 0.7%, or 0.002 km², of the total lava flow area measured on June 28 flowed over lava flows mapped on May 16.

The unknown deposits towards the southwest that were mapped on June 28 intersected a 0.09 km² area of perennial snow and ice. Further analysis and field observations are required to more fully characterize these flows. The spatial extent of the June lahars coincided largely with the extent of the lahars produced in May as one-third, or 0.5 km² of the June lahar location coincides with the May lahar (Table 3.8). It is unclear whether this 0.5 km² area is composed of remnant May lahar deposits or new lahars from June. Both sets of lahars followed closely with the the main drainages northwest of Pavlof volcano and enter into both the Pavlof and Pavlof Sister subsets, as defined by our study (Figures 3.27 and 3.28). It is unclear when the lahars observed on June 28 were produced. If we once again consider the fact that lahars at Pavlof can be formed from pressurized steam explosions that cause fragmentation of lava flow fronts (Belousov et al., 2011), it is probable that the lahars mapped in our study were formed by this mechanism. Clearly defined lava flows with evidence of meltwater with associated steam plumes directly northwest of the flow propagation were observed in the May

eruptive activity (Kaufman, 2013 personal communication) and flows with elevated surface temperatures above background can be observed in nighttime ASTER imagery through the beginning of July. This means that the lahars observed on June 28 could have been produced at any time between June 5 and June 28 (Alaska Volcano Observatory, 2014). If the June lahars were produced during the renewal of eruptive activity on June 5, the area of seasonal snow within the valley northwest of the volcano would match closely with the seasonal snow estimated by the June monthly summary map (Figure 3.23C). However, Product 2 showed that there is a large decrease in the seasonal snow area between June and July. If the lahars were produced towards the end of June, there would be a much smaller area of seasonal snow that would approach the seasonal snow area mapped in the July summary map (Figure 3.24A). It is unclear whether the June lahars were smaller than those in May due to less available seasonal snow, different eruptive activity, or a combination of these two variables. However, the 2013 Pavlof eruption is an extremely interesting case study as it occurred during the period when seasonal snow is in flux (Figures 3.23 and 3.24).

3.7 Conclusion

The primary goal of this study was to track how the snow/ice cover area varies at both Redoubt and Pavlof volcanoes throughout the Alaskan summer months. Snow/ice cover was mapped for eleven individual images of the Redoubt subset and thirteen individual images of the Pavlof subset. By studying these individual images during the

ablation season, we defined the typical seasonal cycle of the snowpack extent. On average, seasonal snow disappears completely from the Drift River valley northeast of Redoubt volcano by July. The disappearance of seasonal snow by this point in the summer extends south past the furthest extent of the Drift Glacier piedmont lobe, revealing glacial ice covered by debris that could include ash from the previous 1966 – 1968 and 1989/90 eruptions (Sturm et al., 1986; Trabant and Meyer, 1992). The presence of debris and ash cover over glacial ice at Redoubt is significant because, depending on thickness, ash or debris cover can either increase or insulate against melting (Driedger, 1981).

Monthly summary maps of snow/ice cover area within the Redoubt subset show a decrease of approximately 44 km² of snow/ice area between May and June and a 37 km² decrease between June and July. However, there is a 55% decrease in remaining snow/ice cover area between July and August, equivalent to approximately 67 km² snow/ice. This could have large implications for the lahar hazards present within the Drift River valley depending on timing of a future eruption. Seasonal snow within the Drift River valley has been a significant contributor of meltwater during previous eruptions at Redoubt. Therefore, the contribution of seasonal snow to meltwater would be vastly different between an eruption before July and one between July and the first appearance of fresh snow in September or October.

There was a dramatic decrease in the observed snow/ice cover area within the Redoubt subset in the months following the 2009 eruption when compared to that expected from the monthly summary snow/ice amounts. In both May and July of 2009,

the snow/ice cover area was less than 5 km². The reappearance of fresh seasonal snow on approximately September 24, 2009 was actually earlier than in the two previous years, when it first snowed around the beginning of October. July and August images acquired one and two years after the end of the eruption showed a smaller snow/ice cover area than expected by the summary maps for these months.

An in-depth analysis of the deposits produced during the 2009 Redoubt eruption is beyond the scope of this study. However, only 38% of the lahar channels used from March 26 through April 1 were reused by the April 4 lahar. Cloud-free imagery needed to study the channels utilized by the March 22-24 lahars was not available.

We analyzed snow/ice cover area within the Pavlof subset against a subset of Pavlof Sister. At the boundaries of the Alaskan ablation season, in April and October, the area covered by seasonal snow within the Pavlof Sister subset is greater due to a high elevation region along the northwestern corner of the subset, approximately 15 km northwest of the Pavlof Sister summit. However, from May through August, there is a larger area of snow/ice cover within the Pavlof subset. This could be due to the influence of larger river drainages within the Pavlof Sister subset, where the seasonal snow tends to melt the fastest.

Monthly summaries of snow/ice cover area show a similar overall trend in the disappearance of seasonal snow between the Pavlof and Pavlof Sister subsets. For both subsets, a greater percentage of snow/ice area is lost between April and May than between May and June. However, the greatest decrease in snow/ice area occurs in both the Pavlof and Pavlof Sister subsets between June and July.

The majority of the flows produced during the 2013 eruption of Pavlof did not intersect regions of perennial snow and ice but instead were underlain by seasonal snow cover on suspected debris-covered ice. This could have implications for melt generation as debris cover can help to insulate glacial ice (Driedger, 1981). Returning to the question of whether snow/ice substrate type has an influence on the efficiency of meltwater propagation, an additional consideration is that the lava flows in the 2013 Pavlof eruption were localized along the northwestern flank of the volcano, an area partly characterized by debris-covered perennial snow and ice. Would there be a difference in meltwater generation if the lava flows were focused towards the more extensive perennial snow and ice along the southwestern flank? Does debris cover on or within a glacier or snowpack effect the flow of meltwater? Due to a lack of cloud-free imagery, a direct comparison could not be made between the snow/ice area expected and measured during the 2013 Pavlof eruption. However, visual interpretations of the summit areas of both Pavlof and Pavlof Sister volcanoes show substantial ash-covered snow regions.

Future research will use the spatial connection between volcanic deposits and underlying snow/ice cover in order to quantify whether type of snow/ice cover influences the likelihood of lahar generation. Redoubt and Pavlof are both volcanoes with substantial glacial cover and long river drainages at their base. The eruptions of volcanoes with little to no ice cover can also be studied to better understand the role of snow/ice cover type in hazard generation.

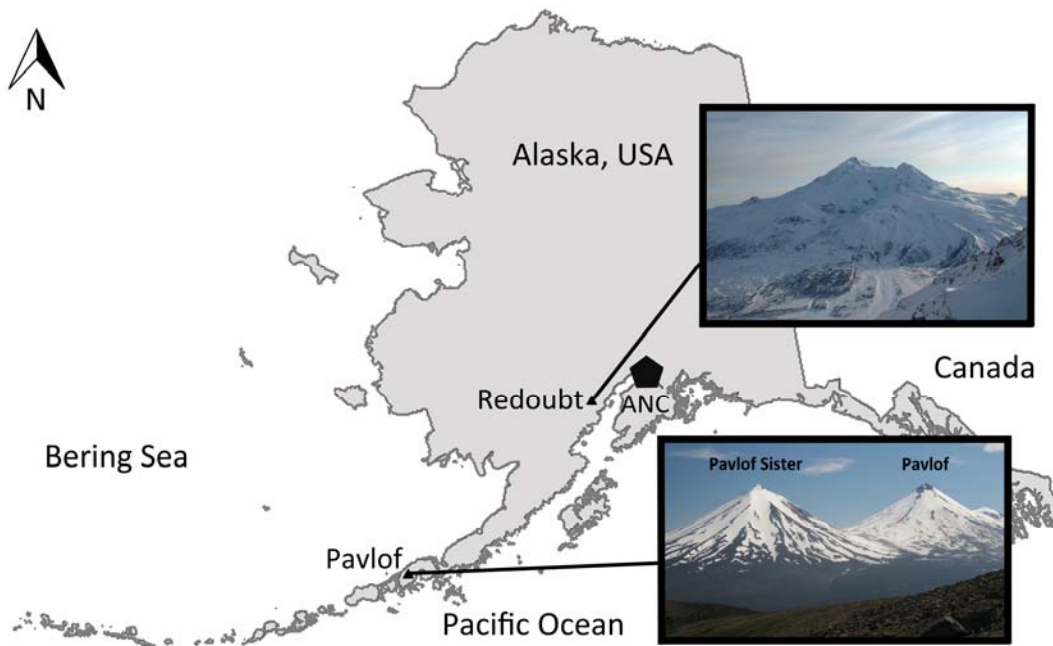


Figure 3.1. Location map of Redoubt and Pavlof volcanoes within Alaska. Note the location of Anchorage, Alaska (ANC) at the pentagon shape. Photograph of Redoubt volcano courtesy of G. McGimsey (United States Geological Survey Alaska Volcano Observatory) and the photograph of Pavlof and Pavlof Sister volcanoes courtesy of C. Waythomas (United States Geological Survey Alaska Volcano Observatory). Base outline of Alaska courtesy the Alaska Volcano Observatory and the United States Geological Survey.

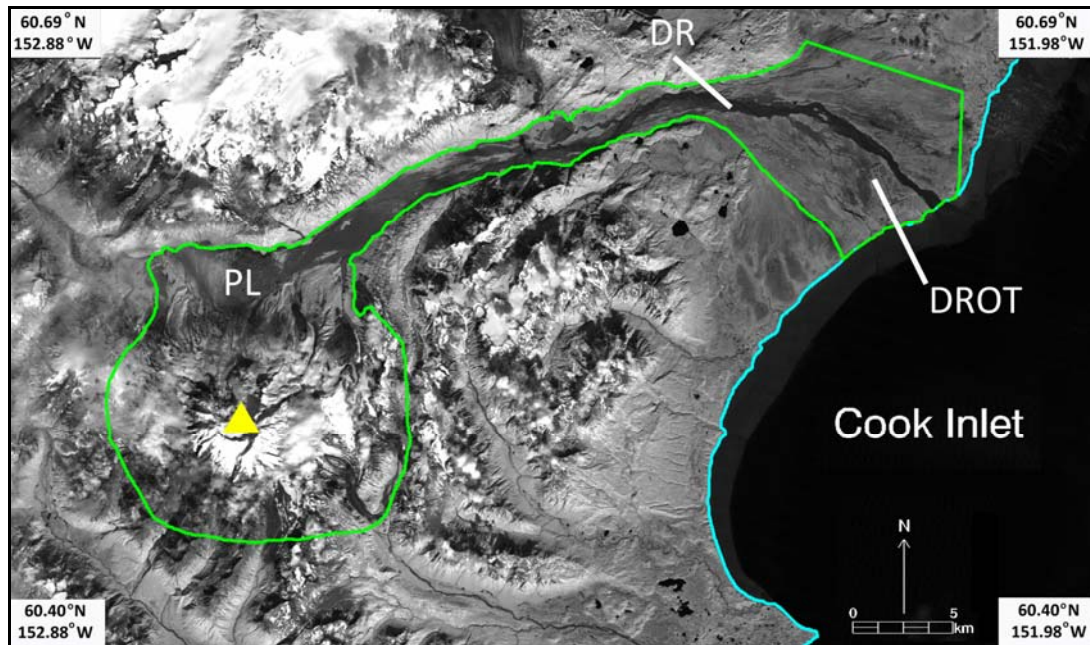


Figure 3.2. Spatial extent of the Redoubt subset. Outline of the subset (in green) used to study all images of Redoubt volcano. The summit of Redoubt is located at the yellow triangle and the coastline with Cook Inlet is outlined in cyan. PL is the location of the Drift Glacier piedmont lobe, DR is the main channel of the Drift River, DROT is the Drift River Oil Terminal.

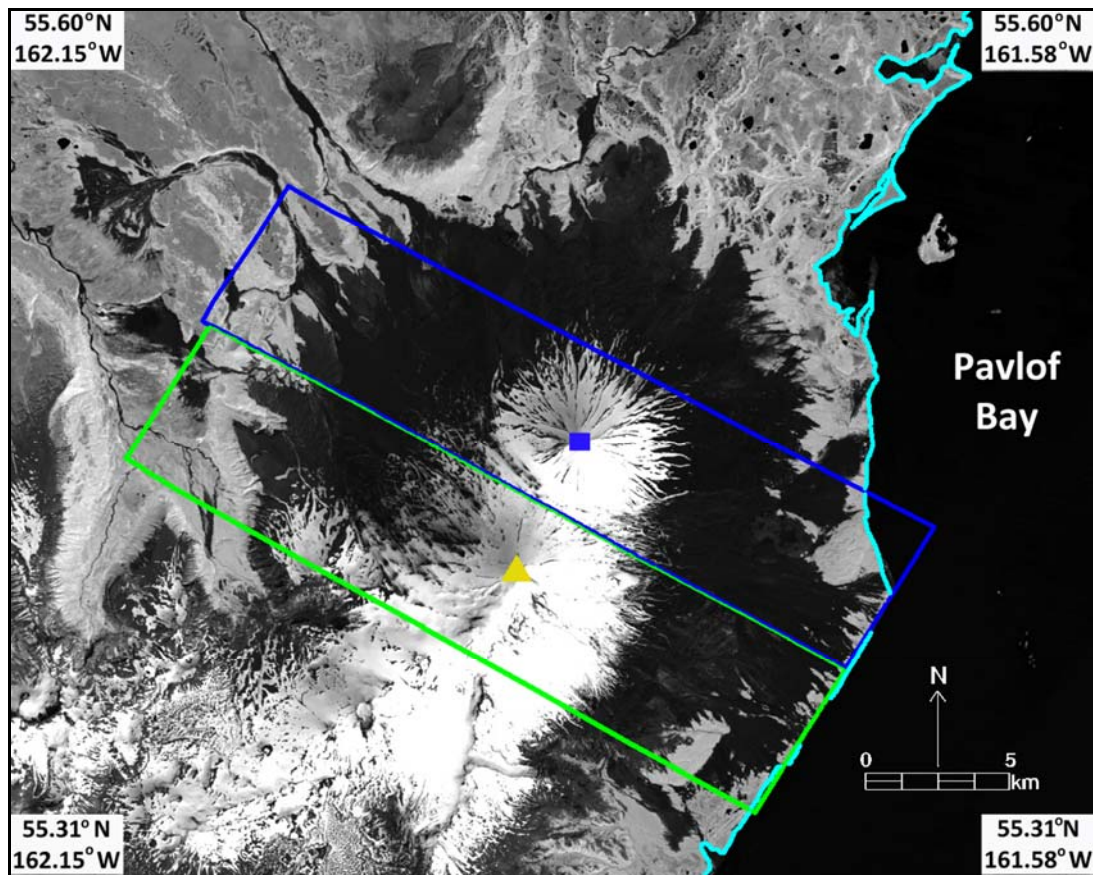


Figure 3.3. Spatial extent of the Pavlof and Pavlof Sister subsets. Outline of the Pavlof subset (outlined in green) and Pavlof Sister subset (outlined in blue). The summit of Pavlof is located at the yellow triangle and the summit of Pavlof Sister is located at the blue square. The coastline with Pavlof Bay is outlined in cyan.

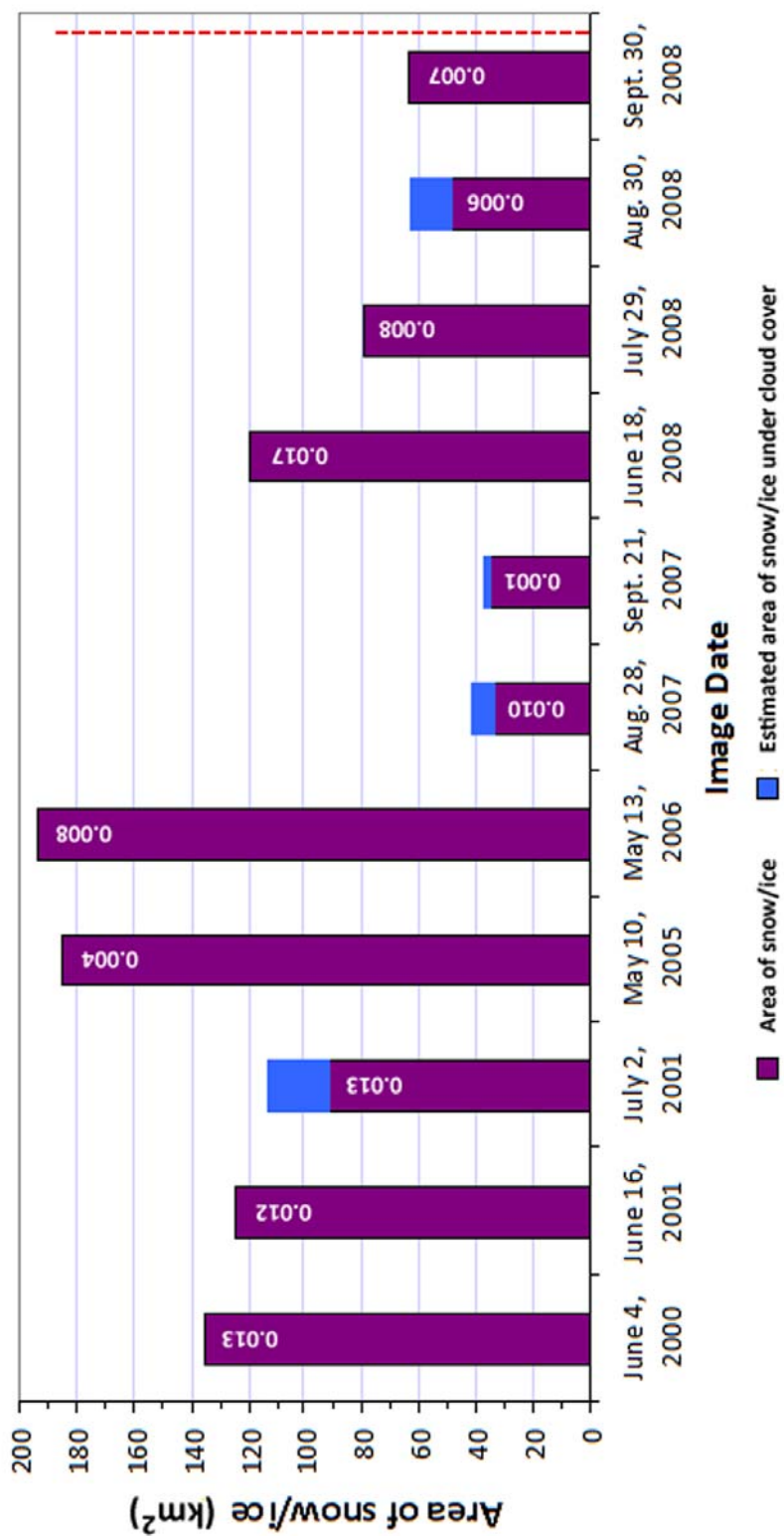


Figure 3.4. Snow/ice area of individual Redoubt images. Area of snow/ice in individual Redoubt subset images exposed without cloud cover (in purple) and estimated under cloud cover (in blue) with RMS error values noted on data bars. Red dotted line indicates the beginning of the 2009 eruption on March 15, 2009.

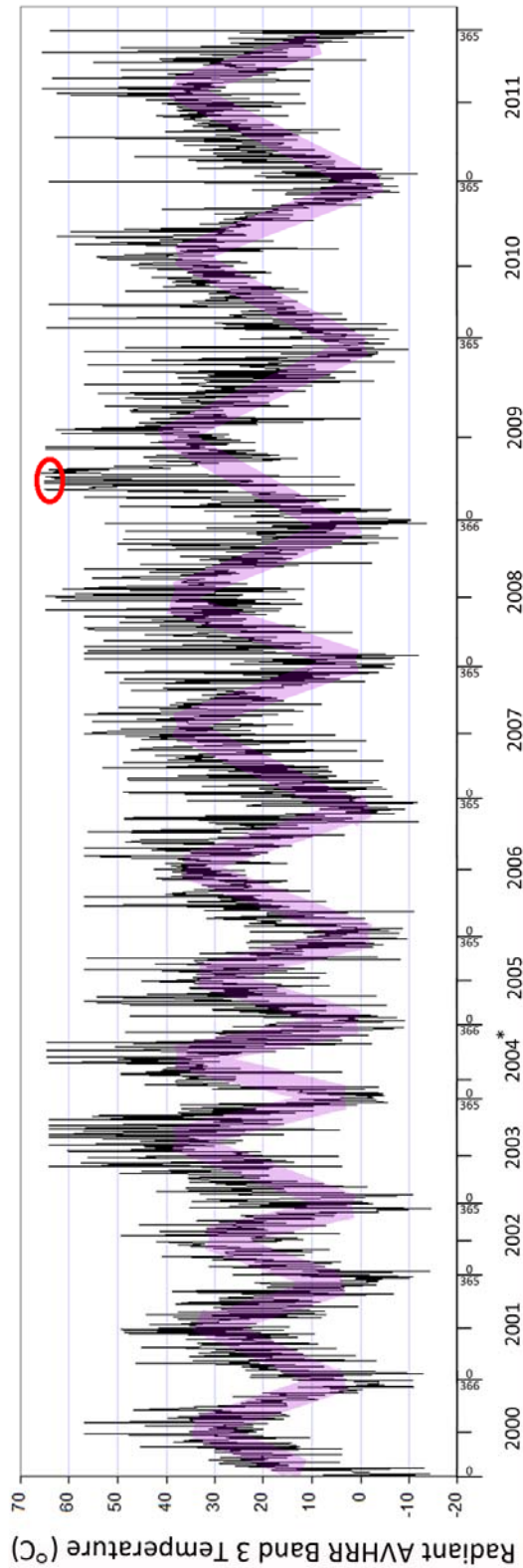


Figure 3.5. Daily maximum radiant AVHRR band 3 temperatures for the Redoubt area. Only nighttime, low satellite zenith angle (below 40°), and cloud-free images were analyzed. Purple line is a visual approximation of the seasonal trends in temperature from 2000 – 2011. The red circle outlines the extended period of high band 3 temperatures, indicative of the eruption from March 15 – April 4, 2009. Data courtesy of the University of Alaska Fairbanks Geophysical Institute.

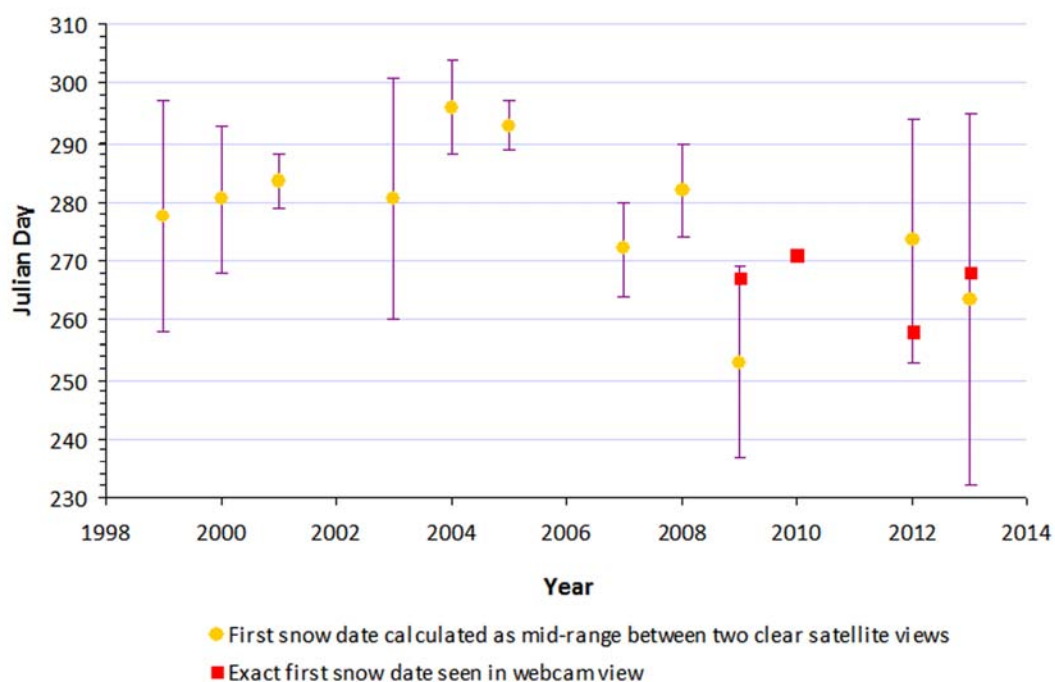


Figure 3.6. Range of dates for the first appearance of seasonal snow after the ablation season for the Redoubt subset with dates approximated as the median between two satellite view endmembers (yellow circles), exact dates seen in Juergen's Hut webcam imagery (red squares), and the range between satellite endmember views (purple bars). The range of Julian Days for the month of August are days 213 – 243 (214 – 244 for leap year); for the month of September are days 244 – 273 (245 – 274 for leap year); for the month of October are days 274 – 304 (275 – 305 for leap year); and for the month of November are days 305 – 334 (306 – 335 for leap year).

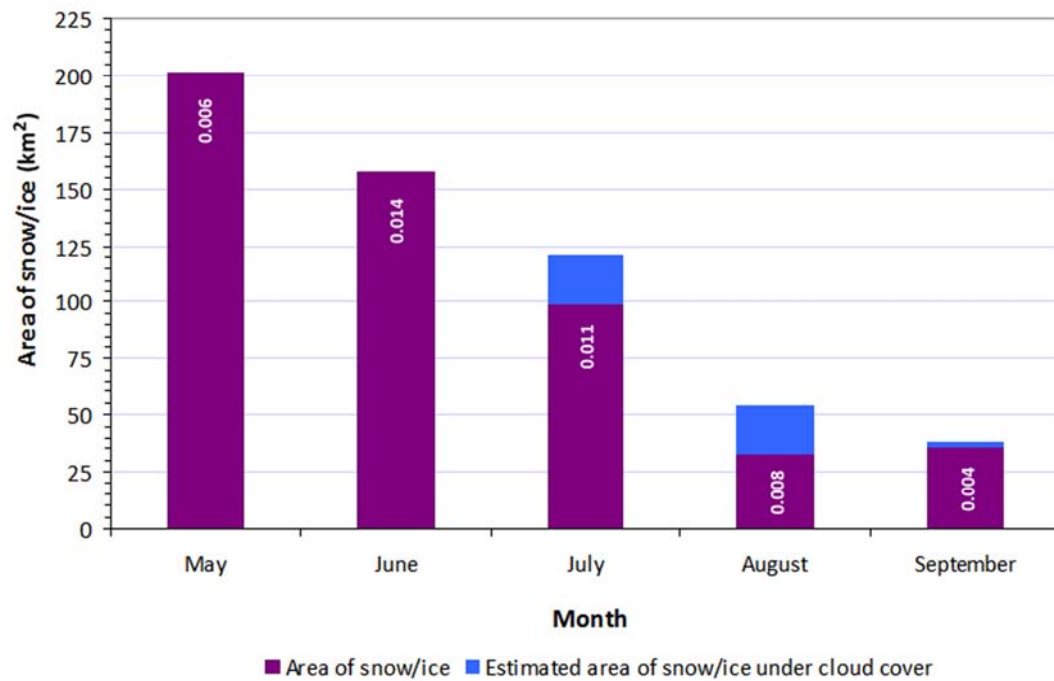


Figure 3.7. Snow/ice area mapped in the Redoubt monthly summary images. Snow/ice area consistently present in May through September (in purple) with estimated snow/ice area under cloud cover (in blue) and RMS error values noted on data bars.

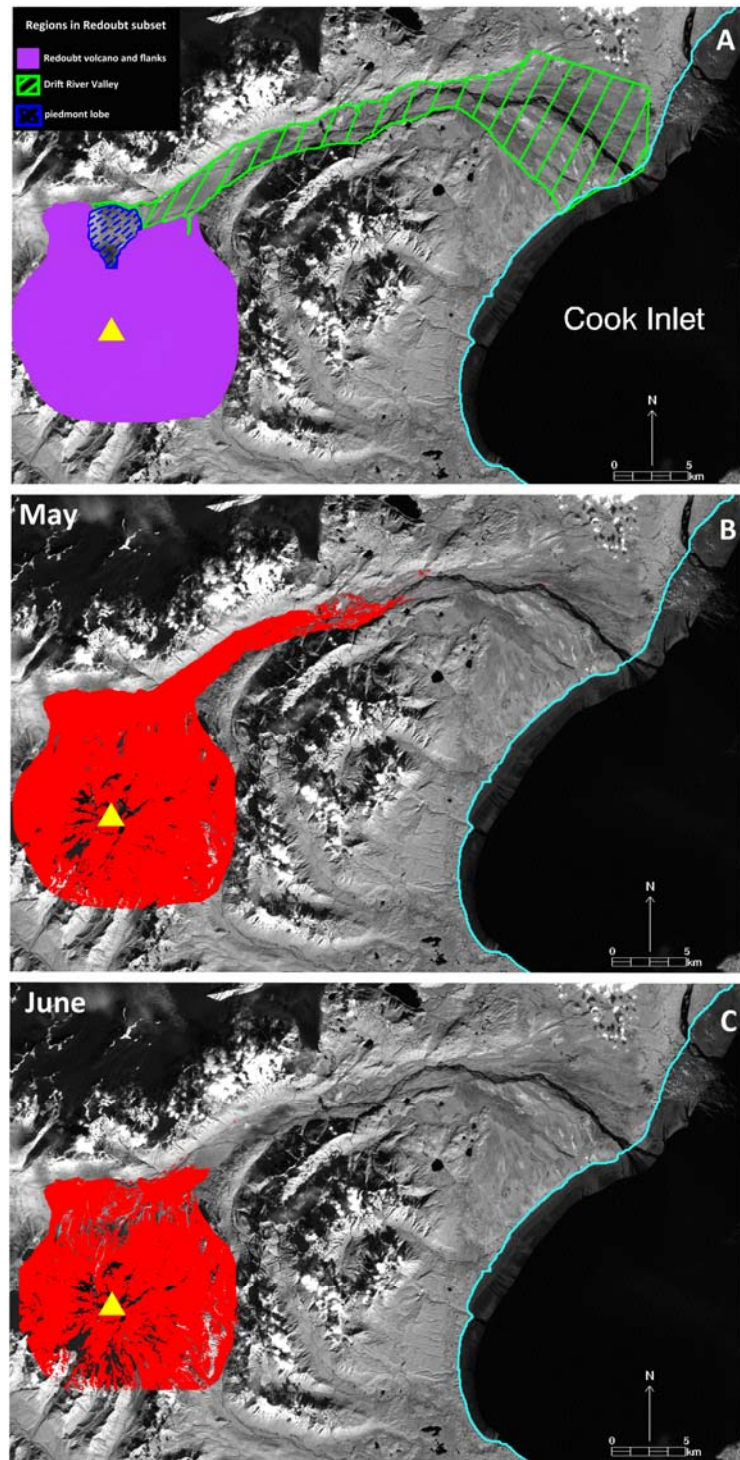


Figure 3.8. May and June monthly snow/ice summary maps for Redoubt. (A) Location of regions within the Redoubt subset. Snow/ice cover area (in red) for May (B), and June (C). Yellow triangles in all images denote the summit of Redoubt volcano and the cyan outline marks the coastline with Cook Inlet.

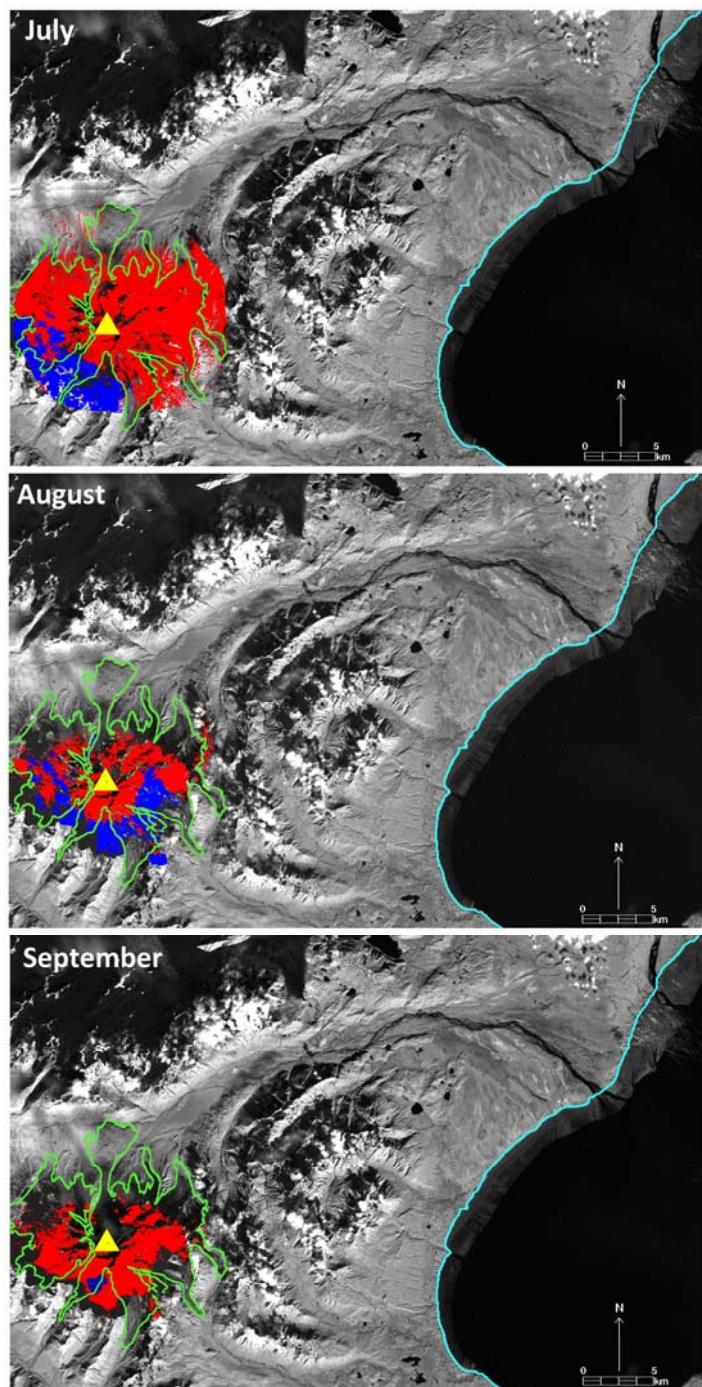


Figure 3.9. July, August, and September monthly snow/ice summary maps for Redoubt. Snow/ice cover area (in red), snow/ice estimated under cloud cover (in blue), and maximum extent of perennial snow and ice as reported in Bleick et al. (2013) (outlined in green) for July (A), August (B), and September (C). Yellow triangles in all images denote the summit of Redoubt volcano and the cyan outline marks the coastline with Cook Inlet.

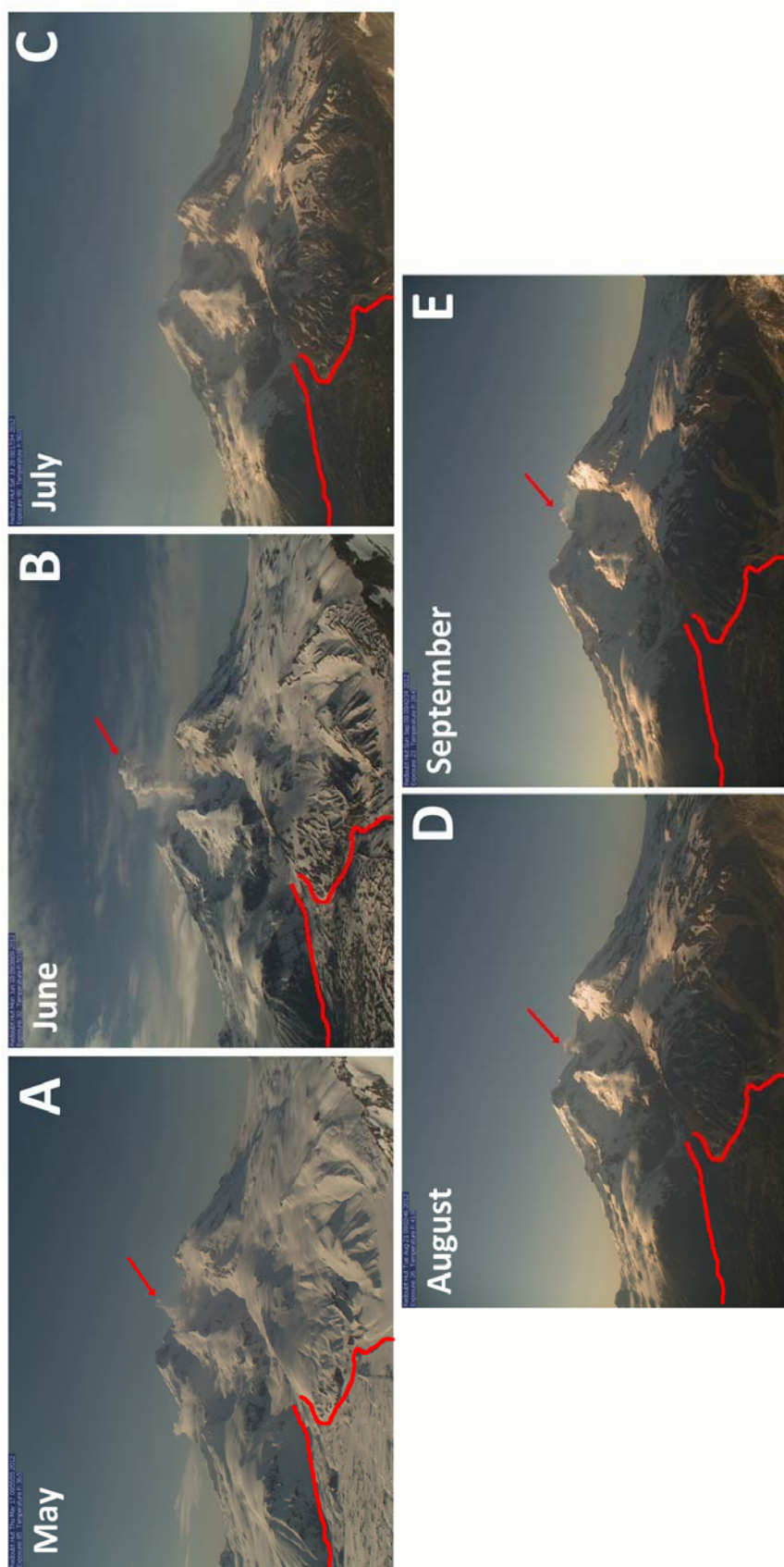


Figure 3.10. Summary of webcam imagery of Redoubt volcano from May – September. Webcam imagery looking south-southwest (SSW) from the Alaska Volcano Observatory’s “Juergen’s Hut” webcam 11 km north of the summit of Redoubt volcano. Images are used here to summarize the changing snow/ice cover at the volcano within the view of the webcam on (A) May 17, 2012 at 09:55 Alaska Daylight Time (AKDT), (B) June 18, 2012 at 09:38 AKDT, (C) July 28, 2012 at 08:17 AKDT, (D) August 21, 2012 at 09:02 AKDT, and (E) September 9, 2012 at 09:42 AKDT. The portion of the Drift Glacier piedmont lobe visible is outlined in red and visible steam plumes are indicated by red arrows. All images are courtesy of the Alaska Volcano Observatory and the United States Geological Survey.

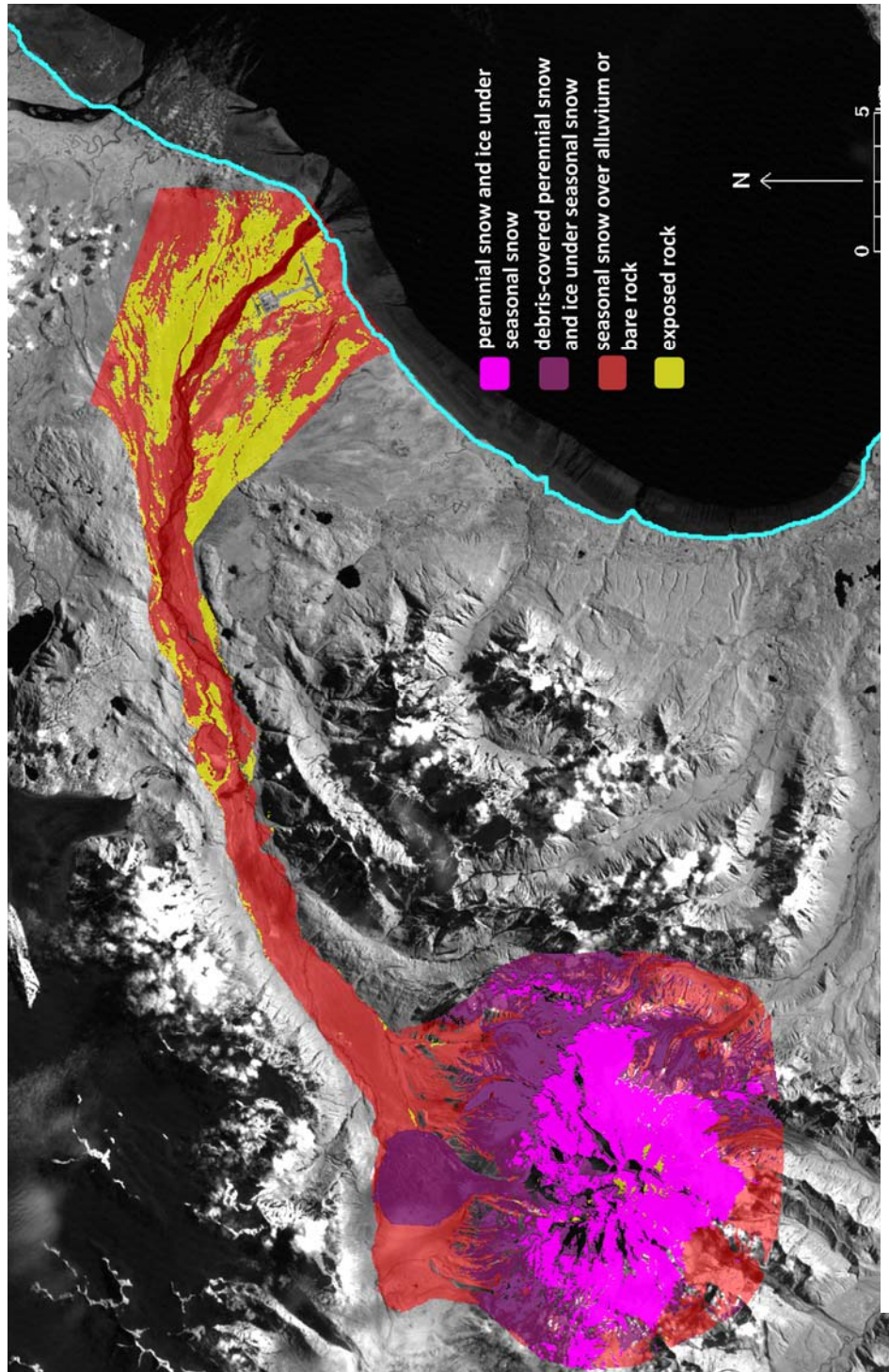


Figure 3.11. Snow/ice cover mapped within the Redoubt subset on March 18, the last available cloud-free image before the beginning of the major explosive eruptive phase during the 2009 eruption of Redoubt (March 22 – April 4, 2009). The region included is the same Redoubt subset used in Products 1 and 2. The coastline with Cook Inlet is outlined in cyan.

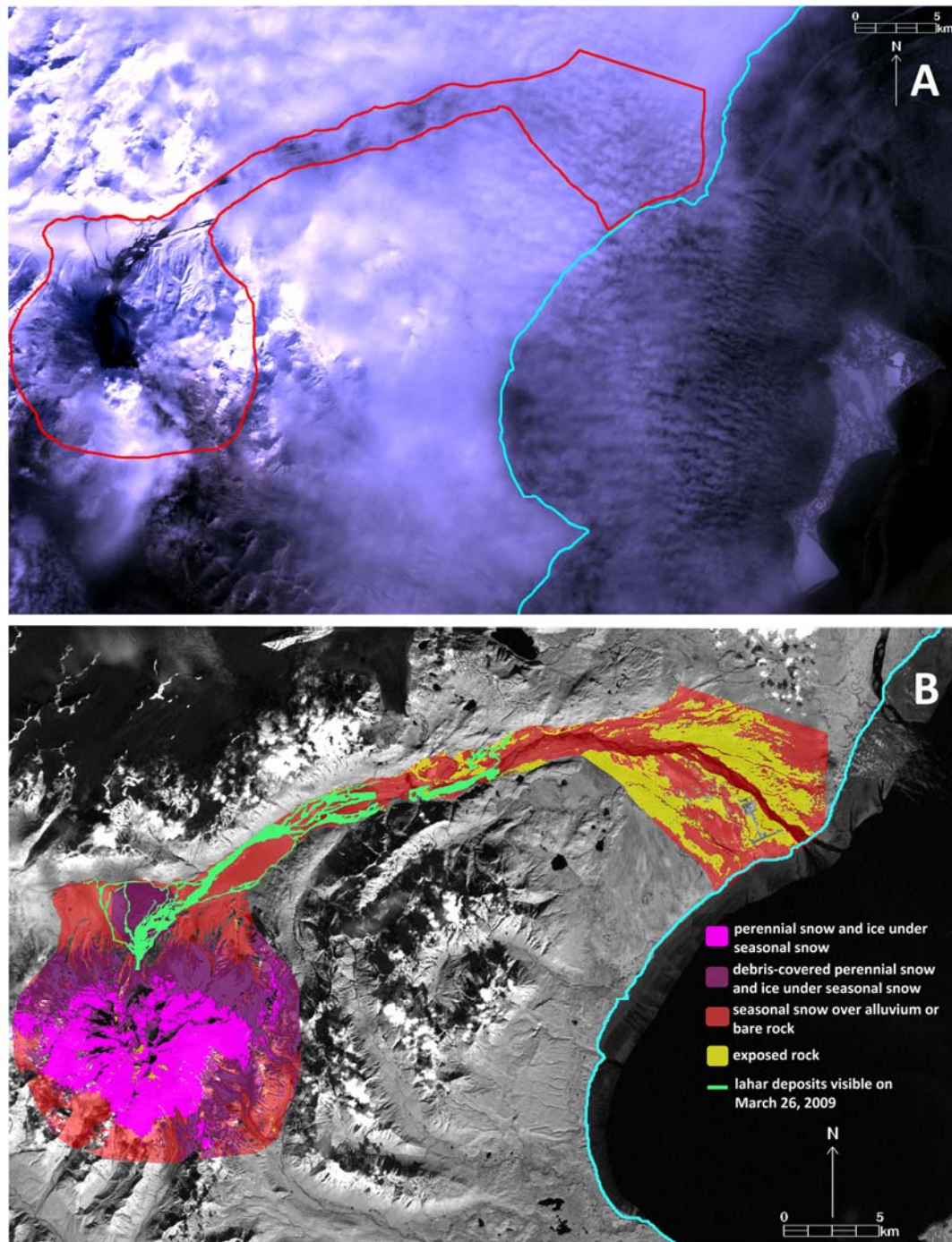


Figure 3.12. Lahar channels visible at Redoubt volcano on March 26, 2009. (A) Landsat 5 TM natural color image showing the dark-colored March 26 lahar deposits underneath patches of thick cloud cover in the Drift River valley. The Redoubt volcano subset is outlined in red, (B) Snow/ice cover map made for March 18 (Figure 3.11) with the lahar channels visible on March 26. The coastline with Cook Inlet is outlined in cyan.

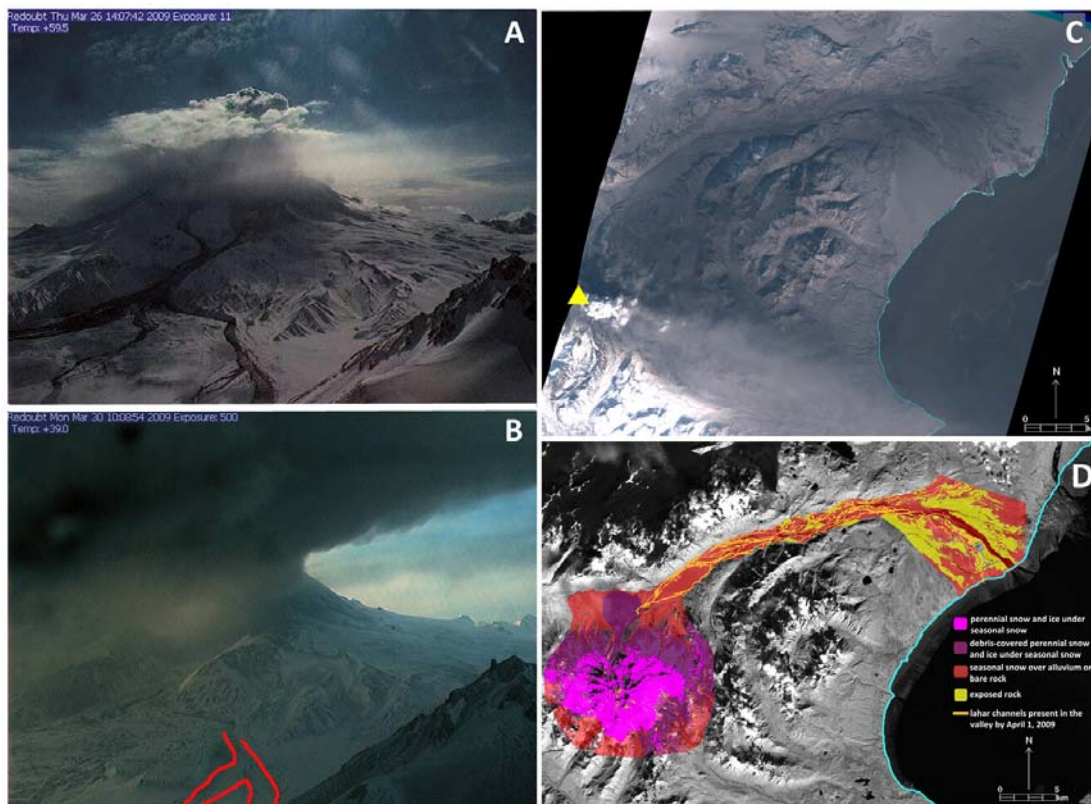


Figure 3.13. Lahar channels visible at Redoubt volcano on April 1, 2009. (A) Image from Juergen's Hut webcam acquired on March 26 at 14:07 AKDT showing dark lahar deposits over snow. View is looking SSW, (B) Image from Juergen's Hut webcam acquired on March 30 at 10:08 AKDT showing fresh snow over previous lahar deposits (example area outlined in red). View is looking SSW, (C) ALI natural color image showing the lahar deposits present within the Drift River valley by April 1. An extensive covering of ash can be seen as the brownish-black deposit present over most of the image. The coastline with Cook Inlet is outlined in cyan, (D) Snow/ice cover map made for March 18 (Figure 3.11) with the lahar deposits visible by April 1. The coastline with Cook Inlet is outlined in cyan. Juergen's Hut images courtesy of the Alaska Volcano Observatory and the United States Geological Survey.

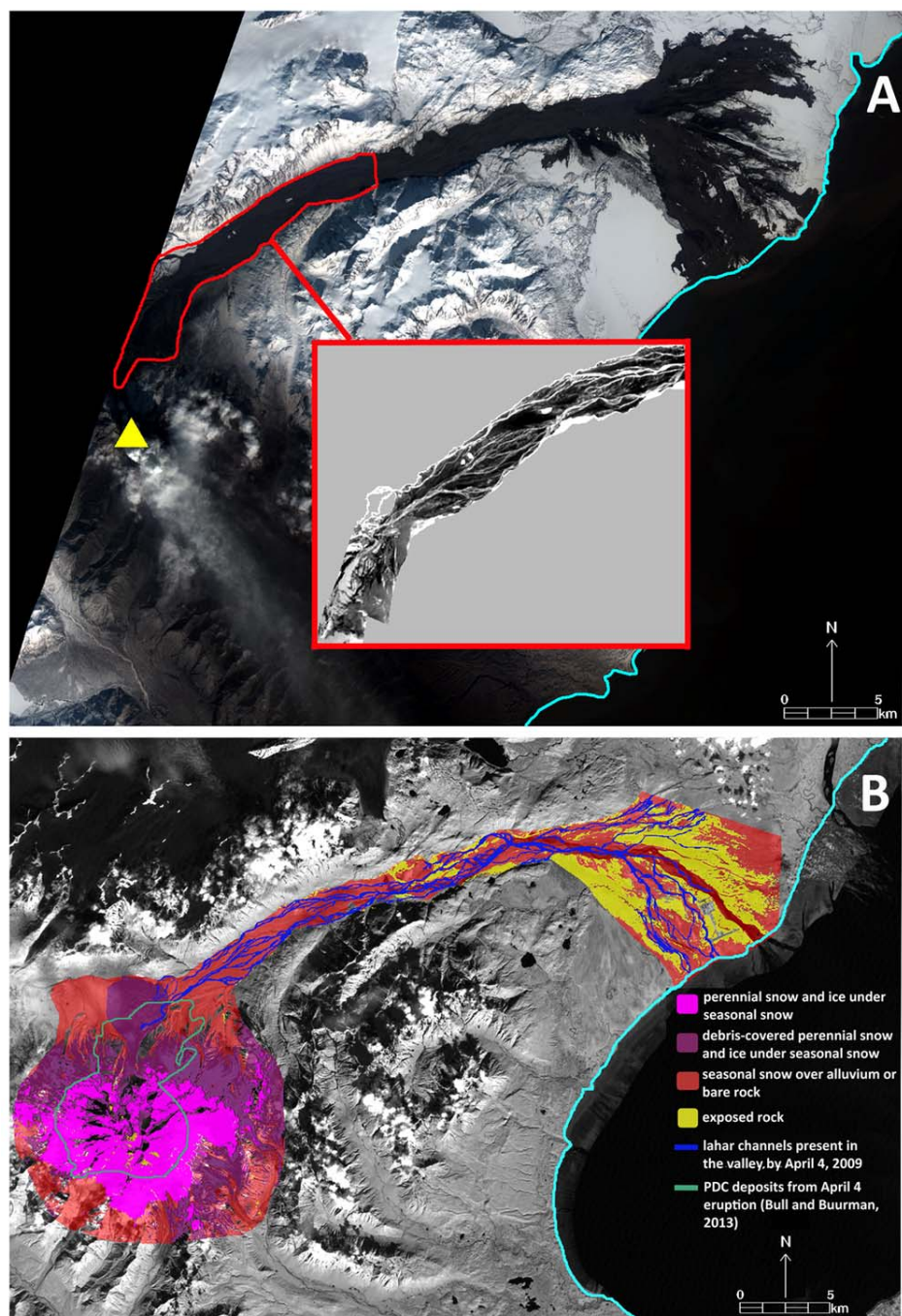


Figure 3.14. Lahar channels present at Redoubt volcano on April 4, 2009. (A) ALI natural color image showing the lahar deposits present within the Drift River valley on April 4. The extensive lahar deposit can be seen as the brownish-black deposit covering the Drift River valley. The braided lahar channels present extensively within the valley can be seen in the first principal component image (insert), (B) Snow/ice cover map made for March 18 (Figure 3.11) with the lahar channels identified on April 4. The coastline with Cook Inlet is outlined in cyan.

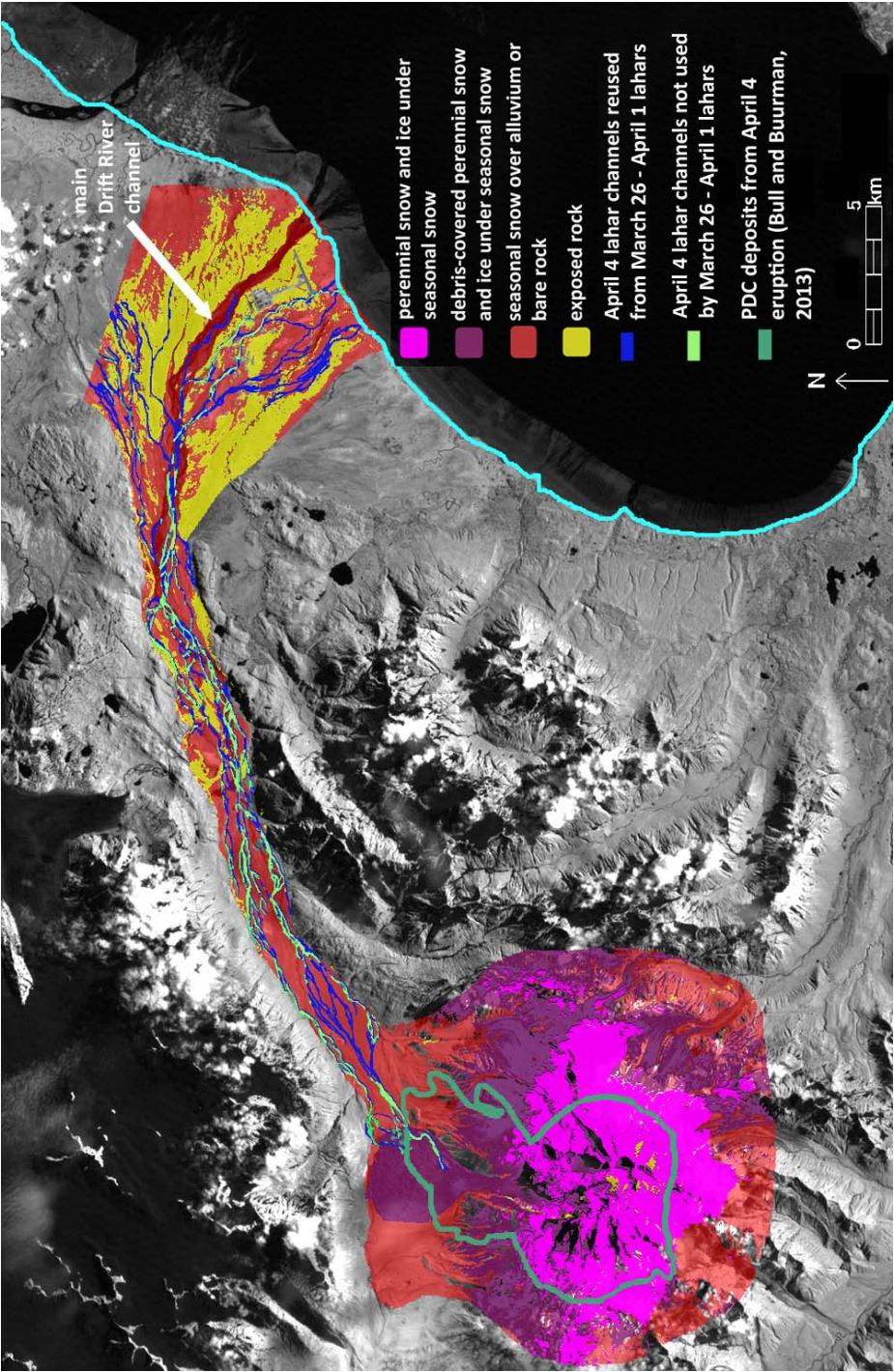


Figure 3.15. Lahar channels on April 4 that were reused from the March 26 – April 1 lahars mapped over the snow/ice cover map made for March 18 (Figure 3.11). The pyroclastic density current deposits produced on April 4 are outlined in dark green and were delineated by Bull and Buurman (2013). The coastline with Cook Inlet is outlined in cyan.



Figure 3.16. Analysis of visible snow/ice area after the 2009 Redoubt eruption. Area of snow/ice cover in monthly summary images (labeled in black) and select individual images (labeled in red) of the Redoubt subset exposed without cloud cover (in purple) and estimated under cloud cover (in blue) with RMS error values noted on data bars.

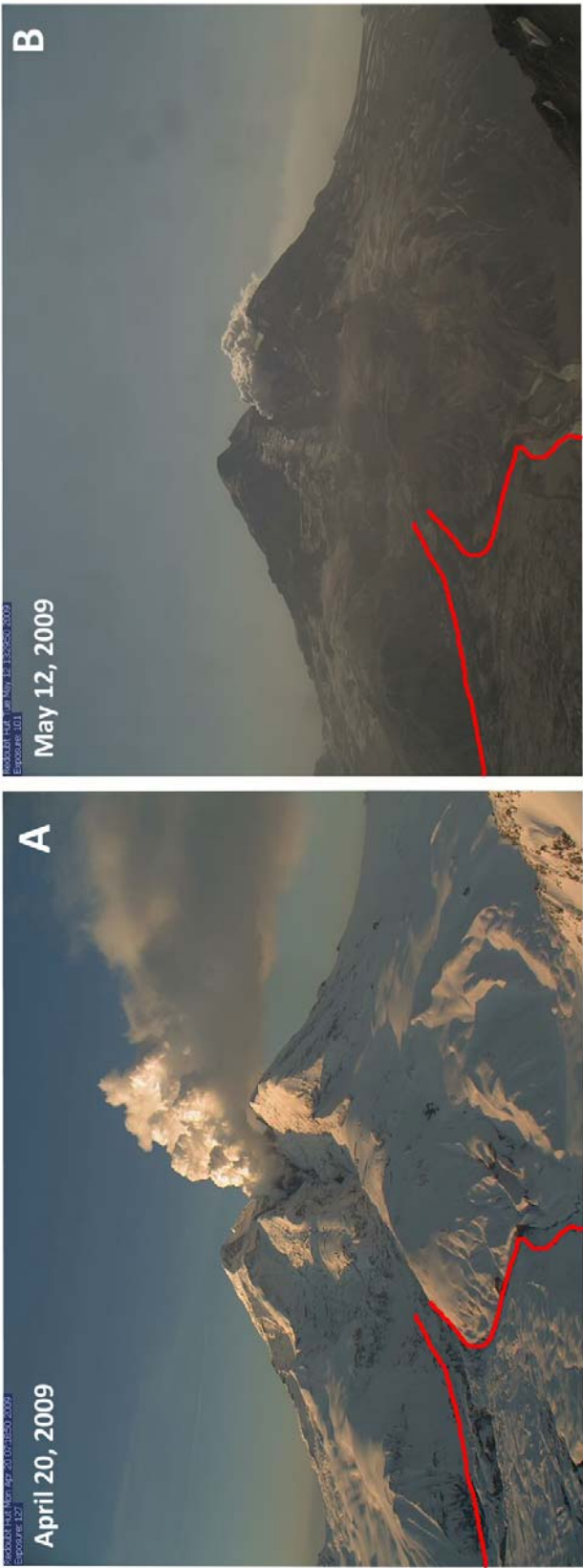


Figure 3.17. Webcam imagery of Redoubt volcano on April 20 and May 12, 2009. Images looking SSW at the flanks of Redoubt volcano from AVO's Juergen's Hut webcam, located 11 km north of the summit. (A) Image acquired on April 20, 2009 at 07:19 AKDT showing extensive surficial snow cover over the deposits from the explosive eruption ending on May 12, 2009 at 13:30 AKDT showing ash covered snow/ice at the volcano, suggesting melt of the surficial snow that fell in the weeks following April 4. The portion of the Drift Glacier piedmont lobe visible is outlined in red. Both images are courtesy of the Alaska Volcano Observatory and the United States Geological Survey.



Figure 3.18. Snow/ice area of individual Pavlof and Pavlof Sister images. Area of snow/ice in individual Pavlof subset images exposed without cloud cover (in purple), in Pavlof Sister subset images exposed without cloud cover (in yellow), and estimated under cloud cover (in blue) with RMS error values noted on data bars. Red dotted line number 1 is the timing of the 2007 Pavlof eruption from August 15 – September 13, 2007. Red dotted line number 2 is the timing of the 2013 Pavlof eruption from May 13, 2013 to July 26, 2013.

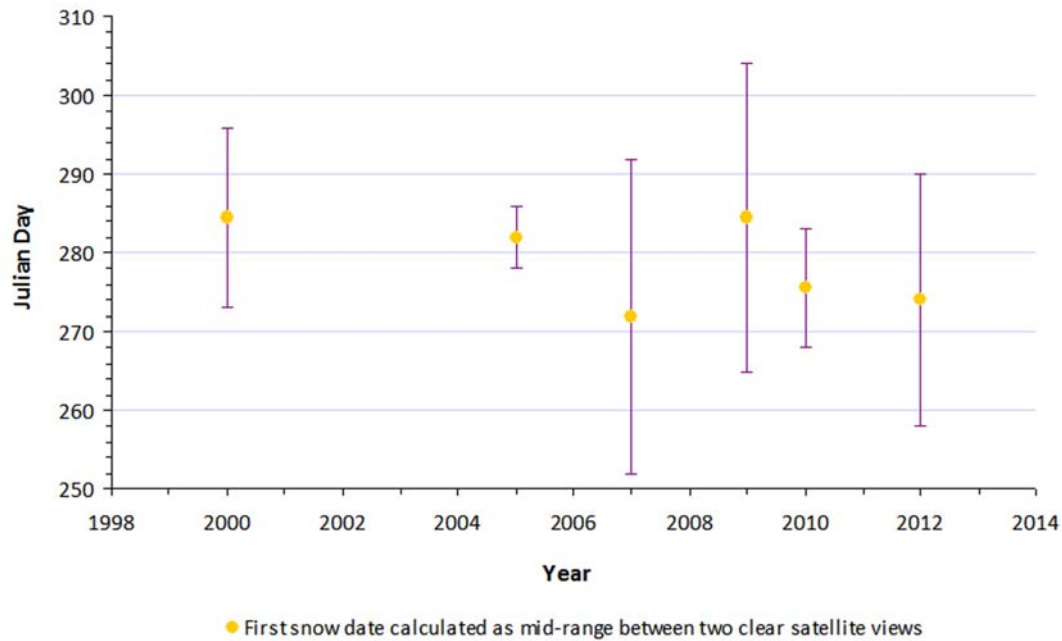


Figure 3.19. Range of dates for the first appearance of seasonal snow after the ablation season for the Pavlof subset with dates approximated as the median between two satellite view endmembers (yellow circles) and the range between satellite endmember views (purple bars). The range of Julian Days for the month of August are days 213 – 243 (214 – 244 for leap year); for the month of September are days 244 – 273 (245 – 274 for leap year); for the month of October are days 274 – 304 (275 – 305 for leap year); and for the month of November are days 305 – 334 (306 – 335 for leap year).

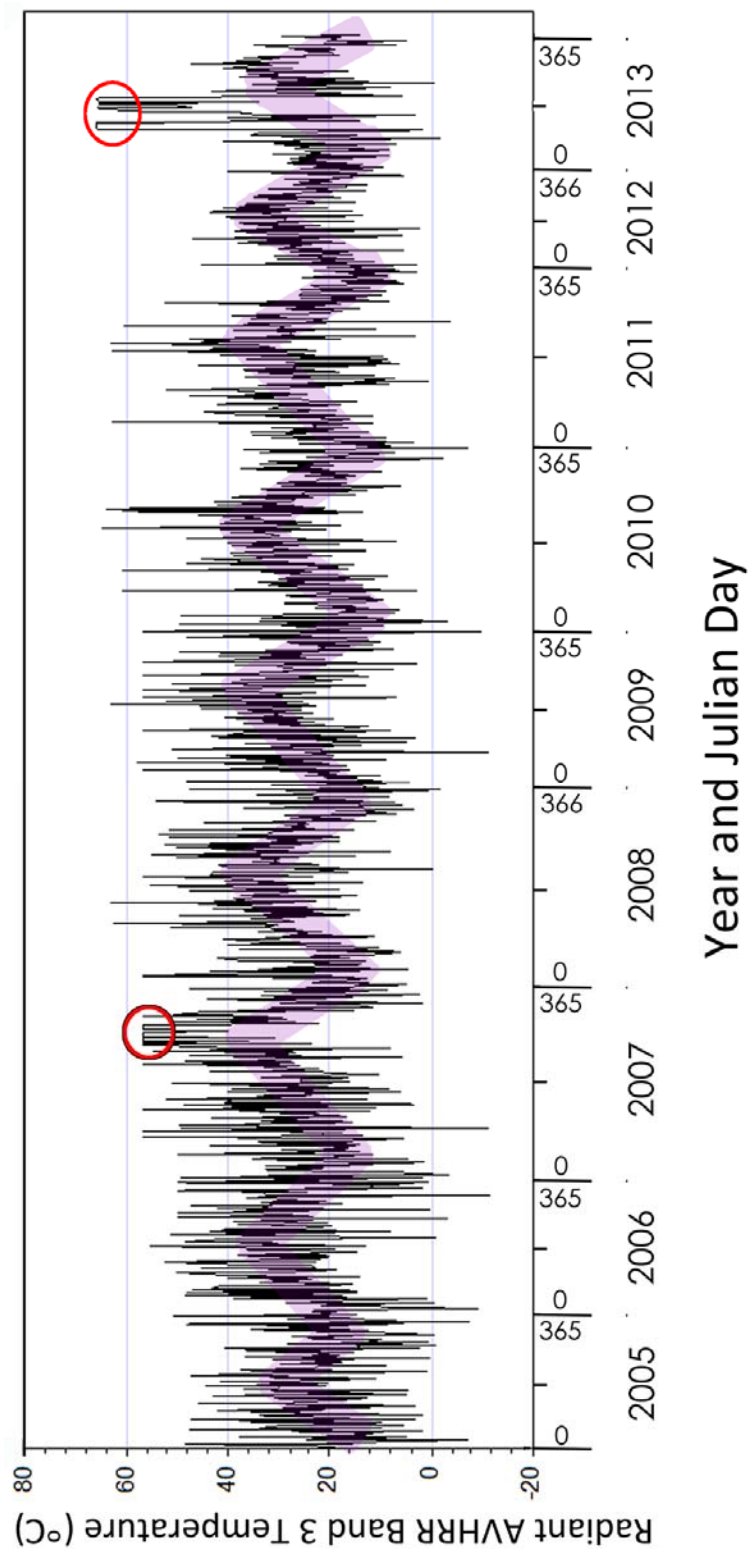


Figure 3.20. Daily maximum radiant AVHRR band 3 temperatures for the Pavlof area. Only nighttime, low satellite zenith angle (below 40°), and cloud-free images were analyzed. Purple line is a visual approximation of the seasonal trends in temperature from 2005 – 2013. The red circles outline the extended periods of high band 3 temperatures, indicative of the eruptions from August 15 – September 13, 2007 and May 13 – July 26, 2013. Data courtesy of the University of Alaska Fairbanks Geophysical Institute.

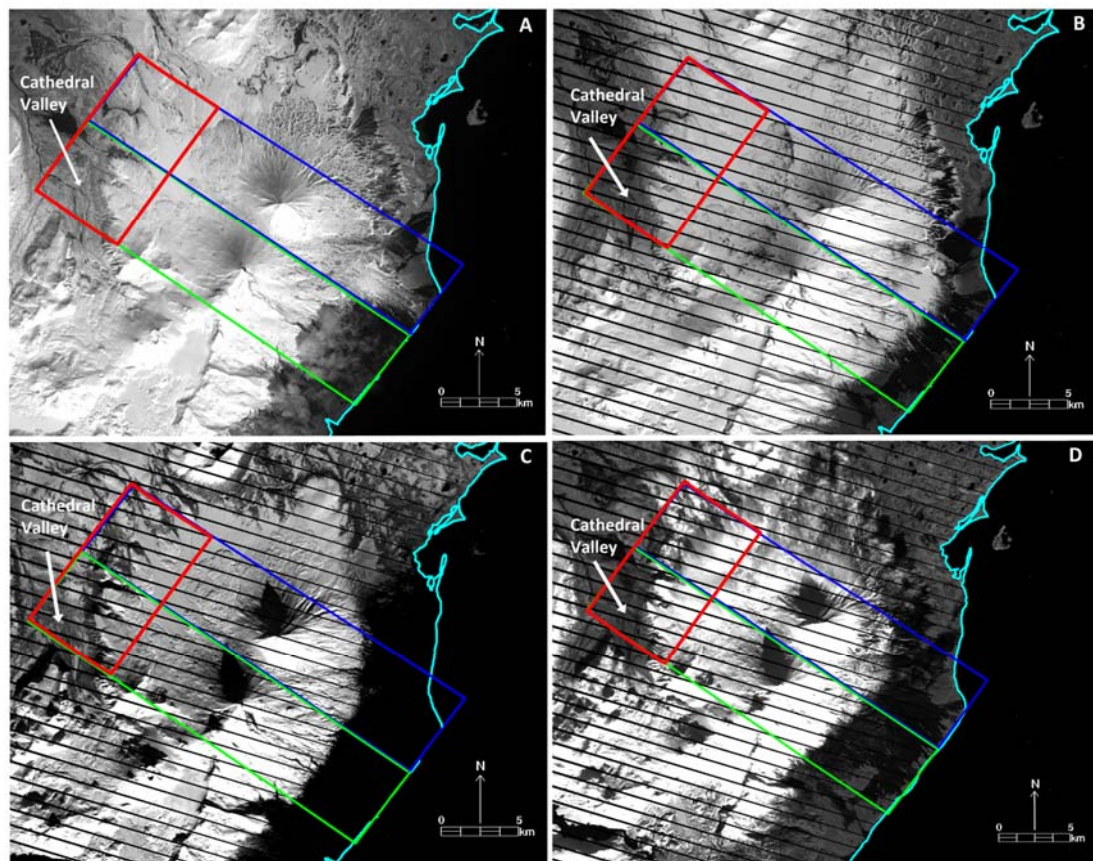


Figure 3.21. April and October images of the Pavlof and Pavlof Sister subsets. (A) Landsat 5 TM grayscale image of the Pavlof subset (outlined in green) and Pavlof Sister subset (outlined in blue) on April 15, 2006, (B) Landsat 7 ETM+ grayscale image of the Pavlof subset (outlined in green) and Pavlof Sister subset (outlined in blue) on April 25, 2013, (C) Landsat 7 ETM+ grayscale image of the Pavlof subset (outlined in green) and Pavlof Sister subset (outlined in blue) on October 19, 2007, and (D) Landsat 7 ETM+ grayscale image of the Pavlof subset (outlined in green) and Pavlof Sister subset (outlined in blue) on October 21, 2008. The April images show the late disappearance of seasonal snow in the higher elevation region within the northwestern corner (outlined in red box) of the Pavlof Subset while the October image shows the early reappearance of seasonal snow in this same region. This is due to the inclusion of the Cathedral River Valley within the Pavlof subset. The coastline in each image is outlined in cyan and snow is denoted by bright white pixels.

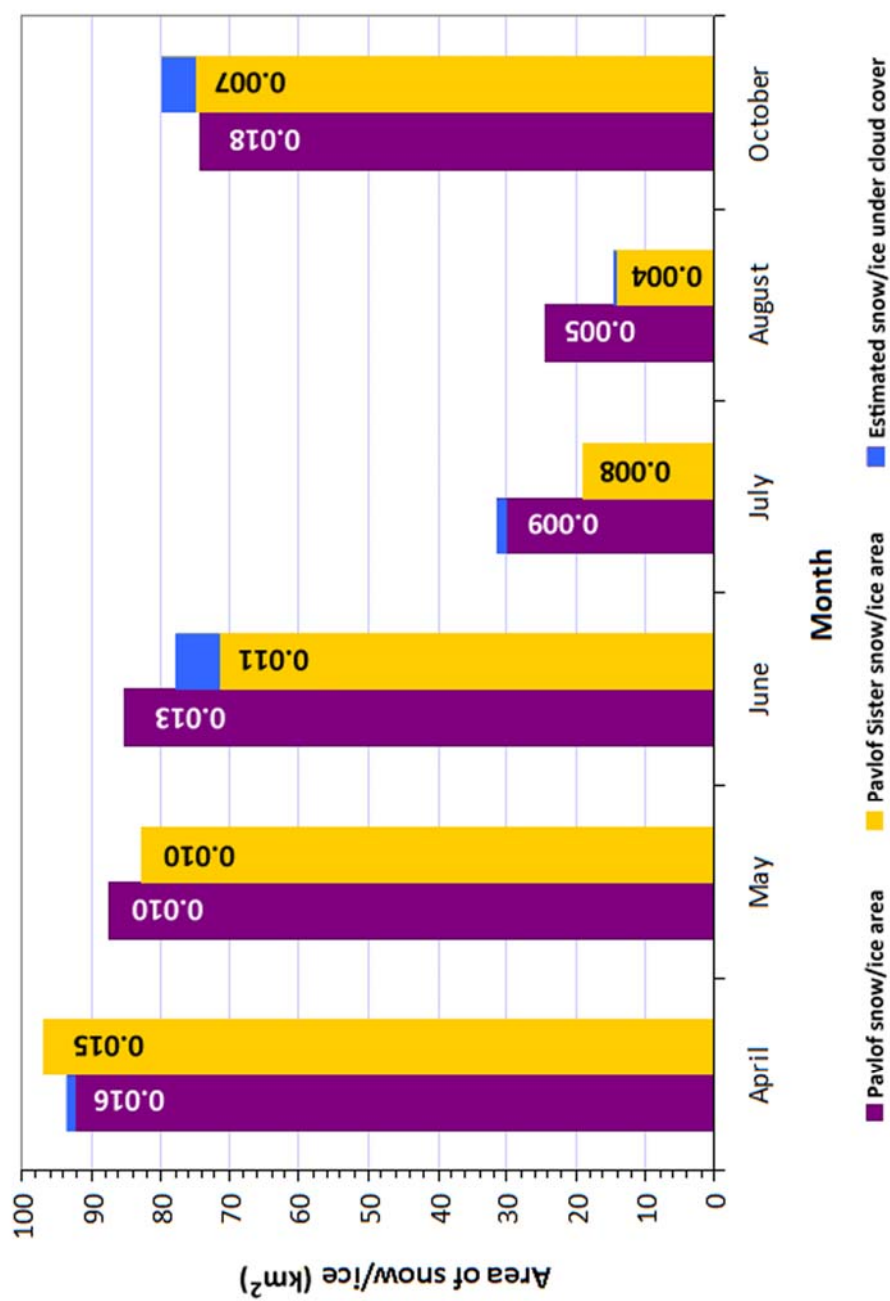


Figure 3.22. Snow/ice area mapped in the Pavlof and Pavlof Sister monthly summary images. Average snow/ice area within the Pavlof subset images (in purple) and Pavlof Sister subset (in yellow) for April through August and October with estimated snow/ice area under cloud cover (in blue) and RMS error values noted on data bars.

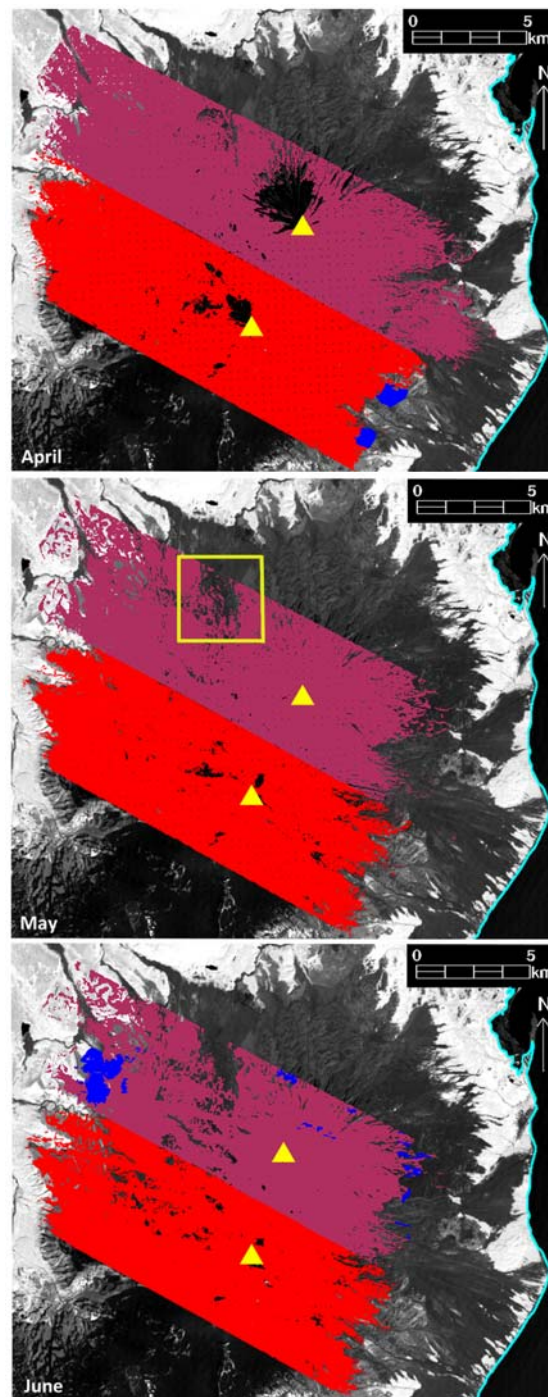


Figure 3.23. April, May, and June monthly snow/ice summary maps for Pavlof and Pavlof Sister subsets. Snow/ice cover area summary map of Pavlof subset (in red) and Pavlof Sister subset (in maroon) with snow/ice estimated under cloud cover (in blue) for April (A), May with extensive area of snow removal in yellow box (B), and June (C). Yellow triangles in all images denote the summit of the volcanoes and the cyan outline marks the coastline with Pavlof Bay.

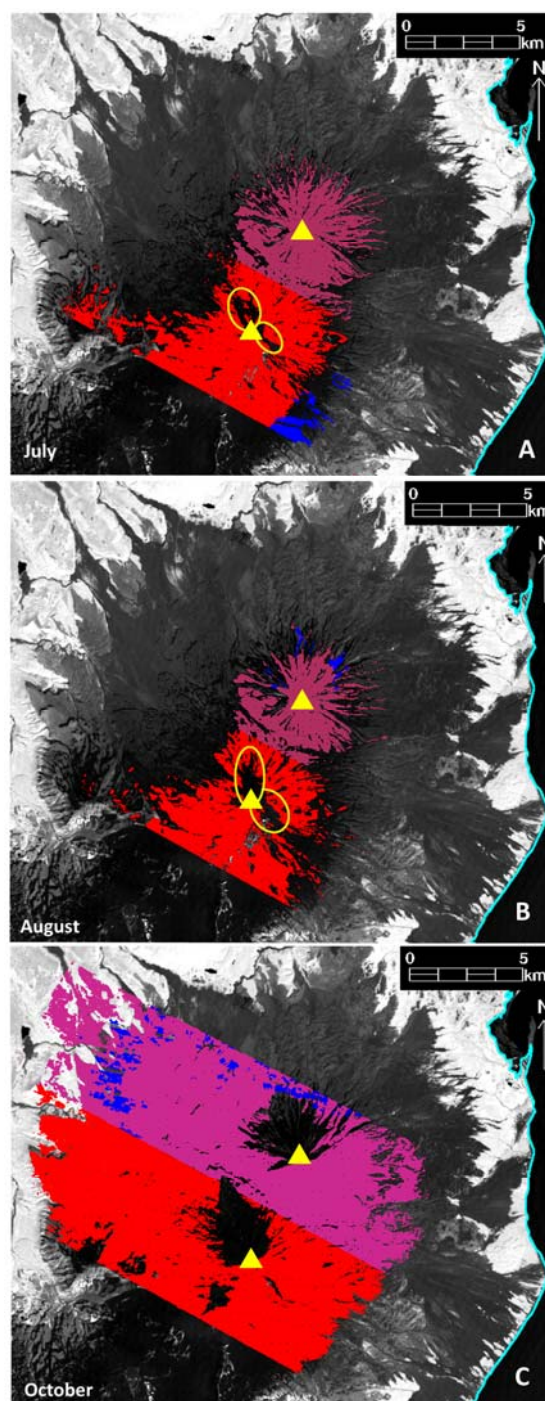


Figure 3.24. July, August, and October monthly snow/ice summary maps for Pavlof and Pavlof Sister subsets. Snow/ice cover area summary map of Pavlof subset (in red) and Pavlof Sister subset (in maroon) with snow/ice estimated under cloud cover (in blue) for July with possible debris cover area in yellow circles (A), August with possible debris cover area in yellow circles (B), and October (C). Yellow triangles in all images denote the summit of the volcanoes and the cyan outline marks the coastline with Pavlof Bay.

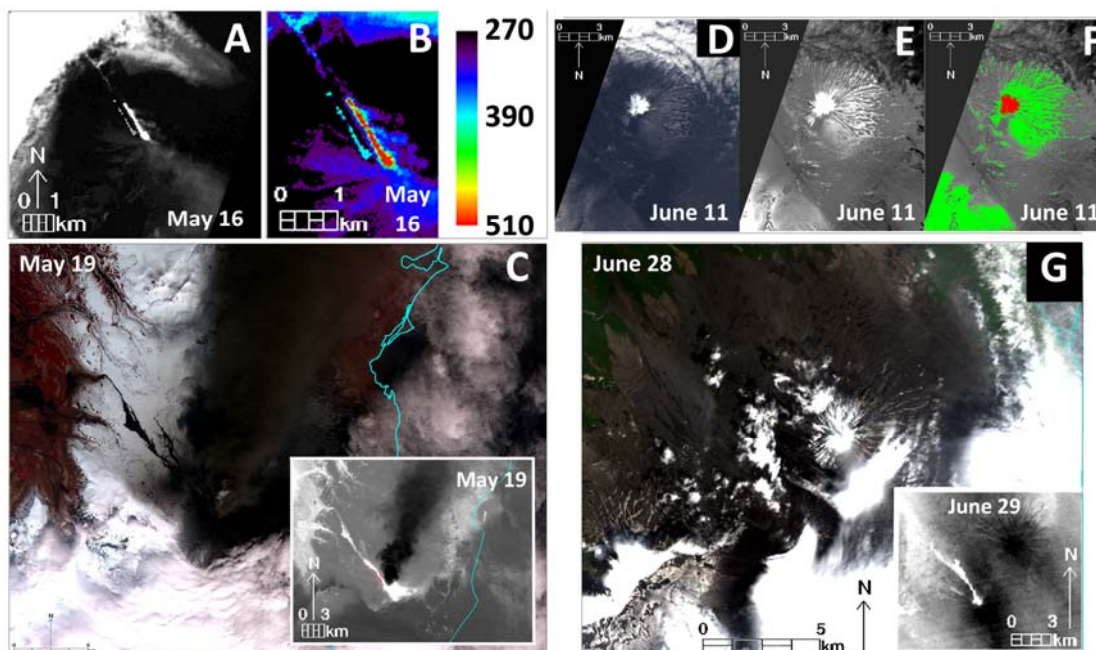


Figure 3.25. Images showing significant deposits from May 16 – June 28 in the 2013 Pavlof eruption. The summit of Pavlof volcano in all images is denoted by the yellow square and the Pavlof Sister volcano summit is located at the blue circle. (A) Hyperion band 150 greyscale image from May 16 showing elevated temperature of flows down the flank of Pavlof volcano; (B) Hyperion band 150 color-scaled brightness temperature image with red pixels having the highest brightness temperature (in Celsius); (C) ASTER VNIR natural color image from May 19. Dark deposit flowing northwest from underneath the dark plume at the summit are lahar flow(s) on snow. A May 19 ASTER TIR image is shown in insert with saturated lava flow pixels delineated in red; (D) ALI natural color image from June 11 showing bright white, fresh snow at Pavlof Sister summit and ash-covered snow at Pavlof volcano summit; (E) Linear spectral unmixing image showing snow pixels in bright white and ash-covered snow as medium to dark grey; (F) Linear spectral unmixing image with green regions mapped as ash covered snow and red regions mapped as fresh snow; (G) Enhanced natural color Landsat 8 OLI image from June 28 showing the variance between snow/ice area on Pavlof and Pavlof Sister. The insert is an ASTER TIR night image acquired on June 29, 2013 with temperatures elevated above background underneath cloud cover down the NW flank of Pavlof volcano.

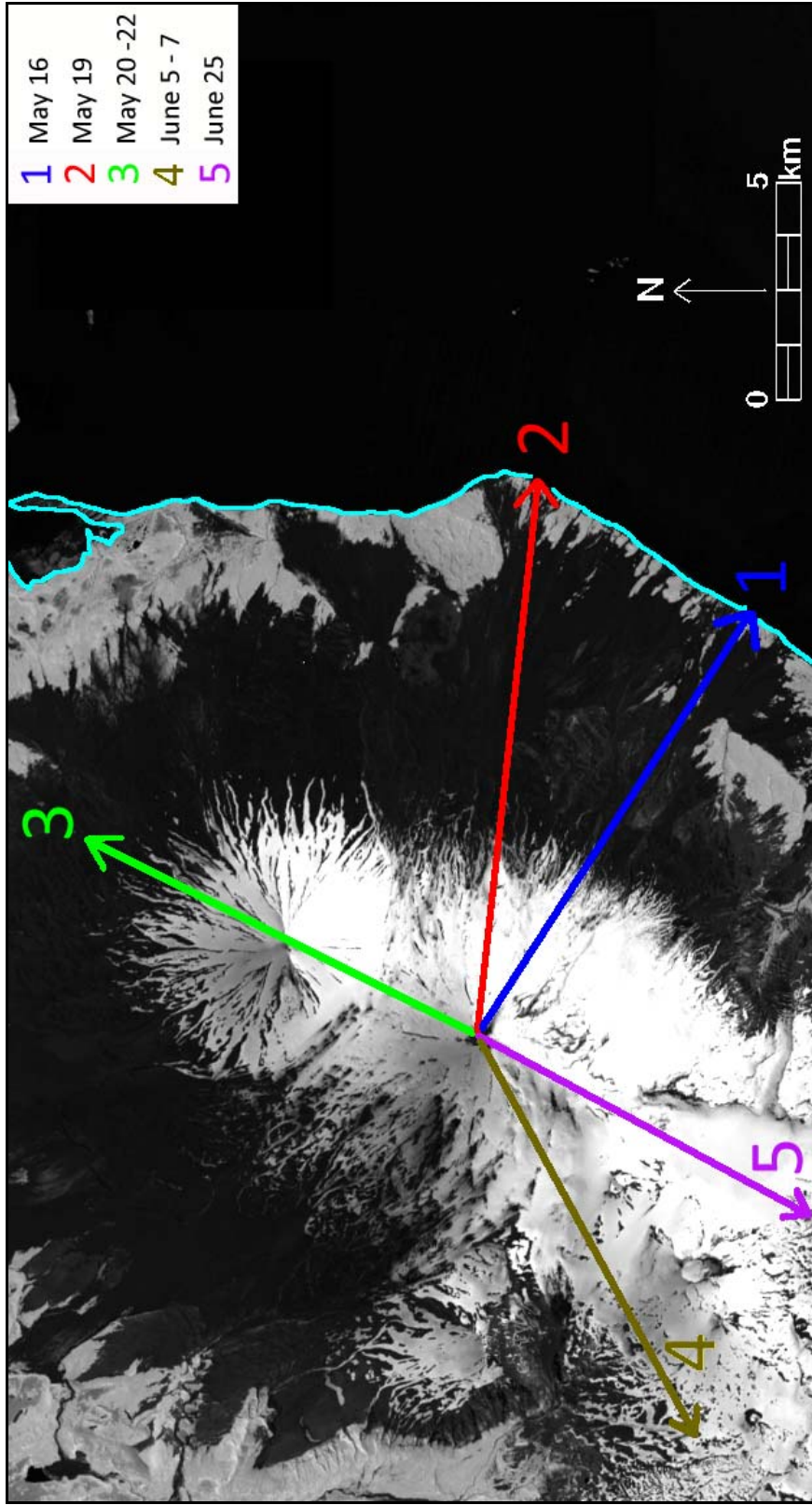


Figure 3.26. Propagation direction of major ash emissions between May 16 – June 25 in the 2013 Pavlof eruption. Coastline with Pavlof Bay is outlined in cyan and base image is a Landsat 5 TM image from July 8, 2005. Data from public weekly updates from the United States Geological Survey Alaska Volcano Observatory, pilot reports, and unpublished Alaska Volcano Observatory data.

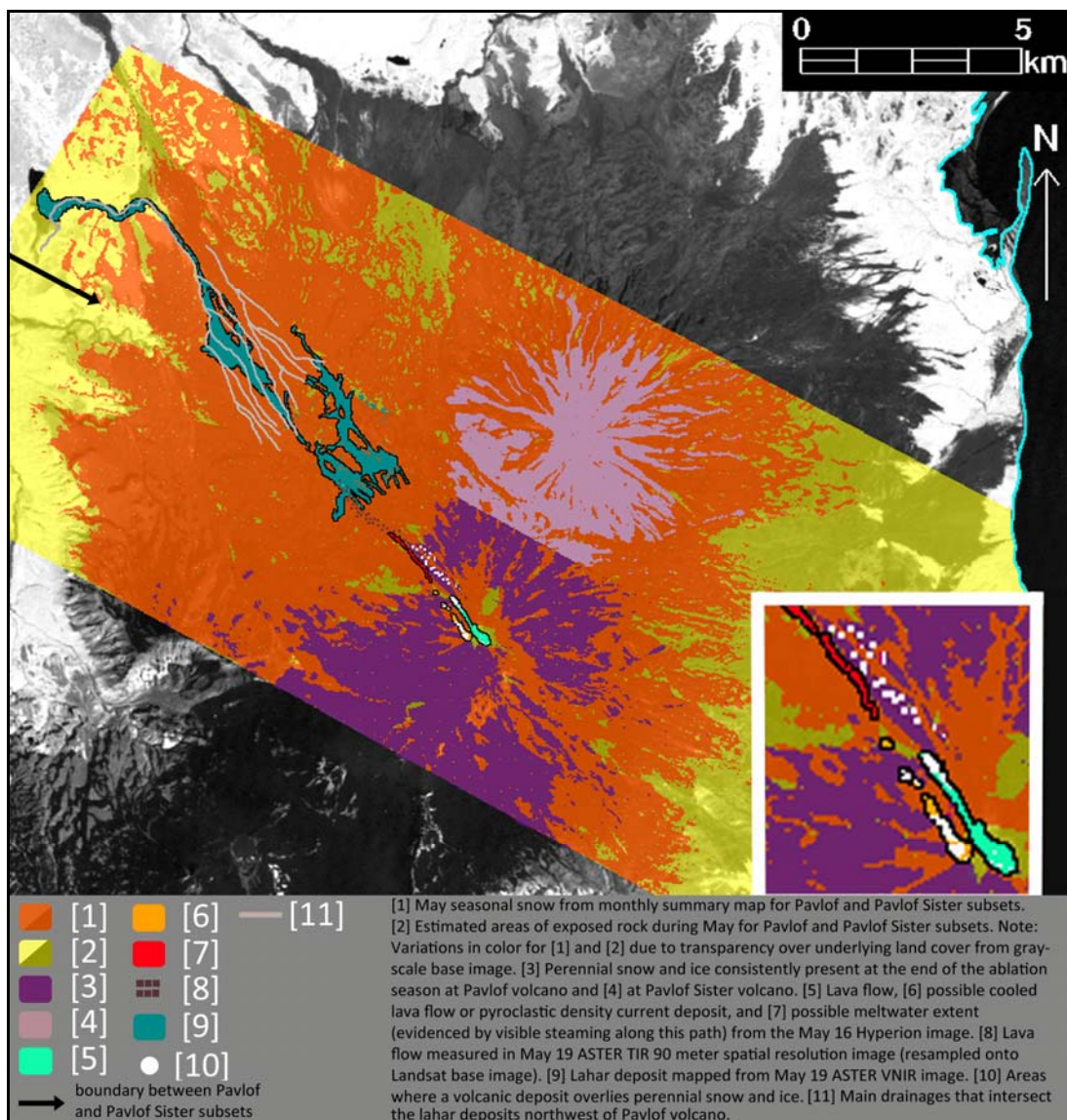


Figure 3.27. Snow/ice cover and deposit maps for the May 13 – May 19 2013 Pavlof eruption. Coastline with Pavlof Bay is outlined in cyan and base image is a grayscale Landsat 5 TM image acquired on July 8, 2005.

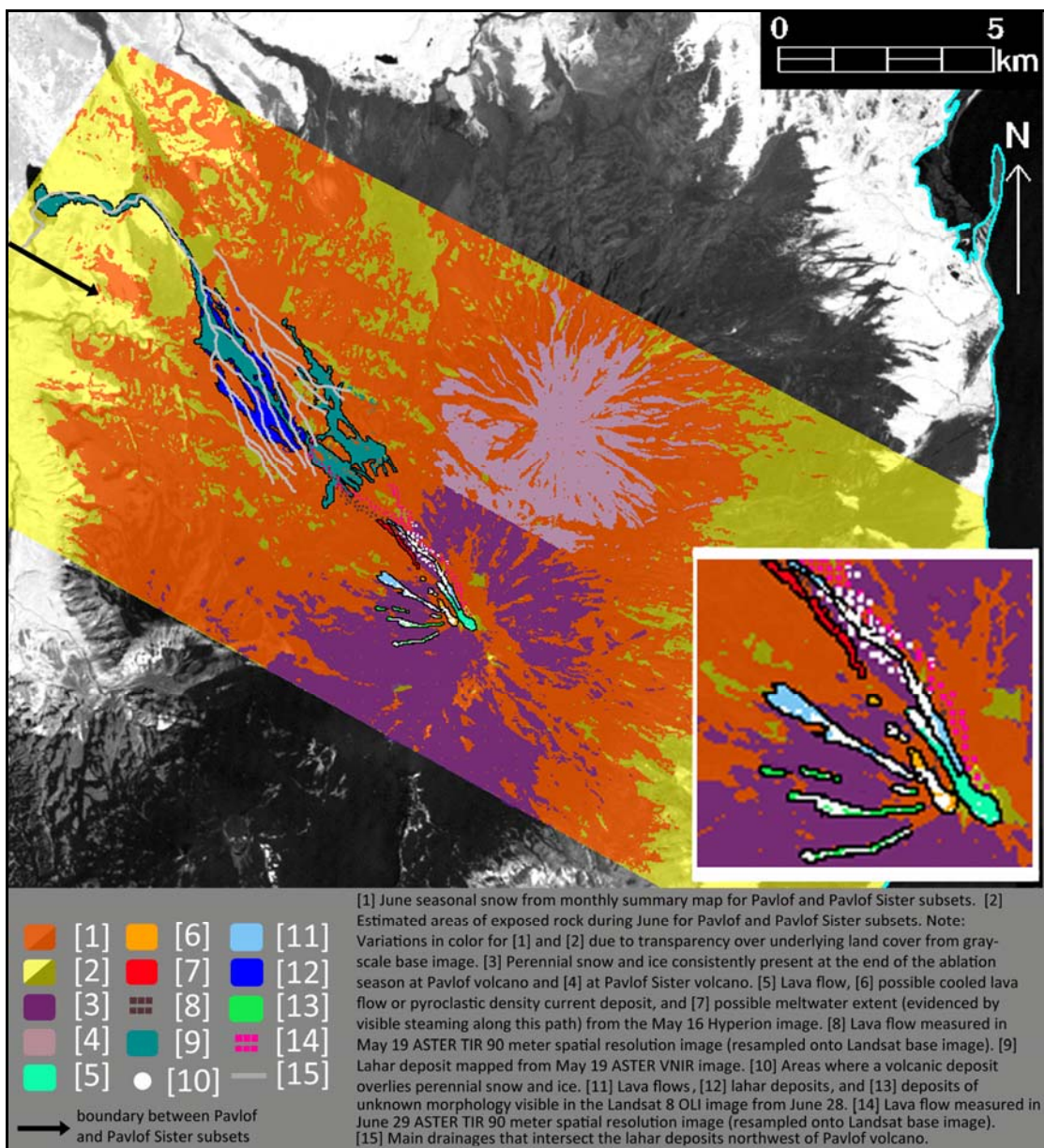


Figure 3.28. Snow/ice cover and deposit maps for the May 13 – May 19 and June 4 – 29 2013 Pavlof eruption. Coastline with Pavlof Bay is outlined in cyan and base image is a grayscale Landsat 5 TM image acquired on July 8, 2005.

Table 3.1. Sensors used to map the snow/ice cover area and eruptive products at Redoubt and Pavlof volcanoes. [VNIR = Visible and Near Infrared; SWIR = Short Wave Infrared; TIR = Thermal Infrared]

Sensor	Full name	Satellite(s)	Availability time range	Nadir Resolution	Scene availability	Bands
Landsat 5 TM	Thematic Mapper (TM)	Landsat 5	March 1, 1984 – June 5, 2013	30 m (VNIR and SWIR) 120 m (TIR)	16 day repeat	7
ASTER	Advanced Spaceborne Thermal Emission and Reflection Radiometer (ASTER)	NASA satellite Terra	December 1999 – present (SWIR bands no longer functional as of 2008)	15 m (VNIR) 30 m (SWIR) 90 m (TIR)	5 day repeat (VNIR) 16 day repeat (SWIR) 16 day repeat (TIR)	15 (with backward-looking band 3B)
Landsat 7 ETM+	Enhanced Thematic Mapper (ETM)	Landsat 7	April 15, 1999 – present	30 m (VNIR and SWIR) 60 m (TIR) 15 m (panchromatic)	16 day repeat	8
ALI	Advanced Land Imager (ALI)	Earth Observing 1 (EO-1)	November 21, 2000 – present	30 m (multispectral bands) 10 m (panchromatic bands)	On-demand scene acquisition	10
Hyperion	Hyperion	Earth Observing 1 (EO-1)	November 21, 2000 - present	30 m	On-demand scene acquisition	220
Landsat 8 OLI/TIRS	Operation Land Imager (OLI) and Thermal Infrared Sensor (TIRS)	Landsat 8	February 11, 2013 – present	30 m (OLI VNIR and SWIR) 15 m (OLI panchromatic) 100 m resampled to 30 m (TIR)	16 day repeat	11

Table 3.2. Percent variance and total difference between monthly summaries of snow/ice area at the Redoubt subset, with negative values indicating a decrease in area.

Months	Percent variance in snow/ice cover area at Redoubt subset	Change in snow/ice area (km ²) at Redoubt subset
May to June	-21.8%	-44.0
June to July	-23.4%	-36.8
July to August	-55.1%	-66.5
August to September	-31.1%	-16.9

Table 3.3. Summary of main 2009 eruptive events and deposits at Redoubt produced between image endmembers used to study the eruption. [*L7* = Landsat 7 Enhanced Thematic Mapper (ETM+); *L5* = Landsat 5 Thematic Mapper (TM); *ALI* = Advanced Land Imager; DROT = Drift River Oil Terminal; PDC = pyroclastic density current].

Image sensor, date, and time *	Events occurring between image dates**
March 15 - March 18 [<i>L7</i>] (before 21:10:35 UTC)	<ul style="list-style-type: none"> • Phreatic event producing tephra fall SE of the volcano on March 15 • Fresh snow on March 16
March 18 (after 21:10:35 UTC) - March 26 [<i>L5</i>] (before 21:07:11 UTC)	<ul style="list-style-type: none"> • 2 explosive events with ash emission NNE on March 22 • 3 lahars that reached the DROT, 4 explosive events with ash emission NNE, NNW, and WNW on March 23 • 4 lahars and 2 possible PDCs on March 24 • Fresh snow on March 25 • 4 lahars (2 reached DROT), 1 probable PDC, 2 explosive events with ash emissions ESE and E before image acquisition on March 26
March 26 (after 21:07:11 UTC) – April 1 [<i>ALI</i>] (before 20:58:32 UTC)	<ul style="list-style-type: none"> • 1 explosive event with ash emission E after image acquisition on March 26 • 4 lahars, 1 PDC, 5 explosive events with ash emissions ENE, N, and NNE on March 27 • Fresh snow on March 27 after deposition of volcanic products • 9 lahars, 4 possible PDCs, 4 explosive events with ash emissions N, ENE, and NE on March 28 • 5 lahars, 1 possible PDC, 1 episode of tephra fall on March 29 • 2 possible lahars on March 30 • Webcam image on March 30 shows lahar deposits with covering of snow
April 1 (after 20:58:32 UTC) – April 4, 2009 [<i>ALI</i>] (before 21:15:10 UTC)	<ul style="list-style-type: none"> • Fresh snow on April 2, 2009 • Possible fresh snow on April 3, 2009 • Largest lahar of eruption that reached DROT, explosive event with ash emission SE, and dome collapse on April 4, 2009.
April 4, 2009 (after 21:15:10 UTC) – May 13, 2009 [<i>L5</i>] (before 21:08:08 UTC)	<ul style="list-style-type: none"> • Multiple instances of fresh snow in webcam
May 13, 2009 (after 21:08:08 UTC) – July 8, 2009 [<i>L7</i>] (before 21:38:00 UTC)	<ul style="list-style-type: none"> • Fresh snow on May 19, 2009
July 8, 2009 (after 21:38:00 UTC) – Sept. 26, 2009 [<i>L7</i>] (before 21:10:32 UTC)	<ul style="list-style-type: none"> • Fresh snow on September 24, 2009

* Acquisition time is scene center time for Landsat and median time of acquisition for ALI imagery

**Information from Bull and Buurman, 2013; Wallace et al., 2013; and Waythomas et al., 2013

Table 3.4. Summary of Redoubt lahar channel measurements made from Landsat and Advanced Land Imager imagery acquired between March 26 and April 4, 2009.

Image date	Area of visible lahar channels	Visible lahar channels on perennial snow/ice	Visible lahar channels on seasonal snow	Area of reused channel paths
March 26, 2009	16.4 km ²	3.6 km ²	10.6 km ²	-----
April 1, 2009	16.6 km ²	0.6 km ² *	13.2 km ²	5.0 km ² (from visible lahar channels on March 26)
April 4, 2009	23.3 km ²	0.1 km ² *	16.8 km ²	8.8 km ² (from visible lahar channels on March 26 and April 1)

* The majority of Redoubt summit, flanks, and the piedmont lobe are outside the range of this image.

Table 3.5. Percent variance and total difference between the snow/ice area at the Pavlof and Pavlof Sister subsets for each of the 13 individual snow/ice maps. Negative values indicate images in which the snow/ice area at the Pavlof Sister subset was greater.

Image Date	Percent variance between snow/ice area at Pavlof and Pavlof Sister subsets	Change in snow/ice area (km²) between Pavlof and Pavlof Sister subsets
July 6, 2004	75.3%	14.2
July 8, 2005	72.5%	14.1
April 15, 2006	-2.9%	-2.6
May 25, 2006	6.1%	4.5
July 4, 2006	76.7%	15.2
June 4, 2007	1.1%	0.7
Oct. 19, 2007	1.3%	1.0
Aug. 2, 2008	43.6%	11.1
Oct. 21, 2008	-9.2%	-6.6
Aug. 4, 2009	86.3%	9.1
May 4, 2010	14.6%	13.6
June 17, 2012	15.5%	7.8
April 26, 2013	-9.3%	-9.8

Table 3.6. Percent variance and total area difference between monthly summaries of snow/ice area at the Pavlof and Pavlof Sister subsets, with negative values indicating a decrease in area.

Months	Percent variance in snow/ice cover area at Pavlof Subset	Change in snow/ice area (km²) at Pavlof subset	Percent variance in snow/ice cover area at Pavlof Sister subset	Change in snow/ice area (km²) at Pavlof Sister subset
April to May	-6.4%	-5.9	-14.7%	-14.2
May to June	-2.4%	2.1	-6.1%	-5.1
June to July	-63.1%	-53.8	-75.3%	-58.4
July to August	-22.9%	-7.2	-24.5%	-4.7
August to October	207.6%	50.3	451.7%	65.2

Table 3.7. Summary of main 2013 eruptive events and deposits produced at Pavlof between image endmembers used to study the eruption. [*L7* = Landsat 7 Enhanced Thematic Mapper (ETM+); *ASTER* = Advanced Spaceborne Thermal Emission and Reflection Radiometer; *VNIR* = Visible and Near Infrared; *TIR* = Thermal Infrared; *ALI* = Advanced Land Imager; *L8* = Landsat 8 Operation Land Imager (OLI)].

Image sensor, date, and time*	Events occurring between image dates**
April 26, 2013 [<i>L7</i>] -	<ul style="list-style-type: none"> Increased seismic activity beginning on May 13 Lava fountaining from a vent on the north flank of the volcano with a lava flow advancing down the northwest flank.
May 16, 2013 [<i>Hyperion</i>] (before 21:29:42 UTC)	<ul style="list-style-type: none"> Steaming flows down northwest flank of volcano NE drifting ash plume on May 14 ENE drifting ash plume on May 15 SE drifting plume on May 16
May 16, 2013 (after 21:29:42 UTC) – May 19, 2013 [<i>ASTER VNIR and TIR</i>] (before 22:10:01 UTC)	<ul style="list-style-type: none"> ESE to SE drifting ash plumes on May 17 SE drifting ash plume on May 18 Ash fall on Sand Point, AK (SE from volcano) on May 19 NE drifting ash plume just before image acquisition on May 19
May 19, 2013 (after 22:10:01 UTC) – June 11, 2013 [<i>ALI</i>] (before 21:14:47 UTC)	<ul style="list-style-type: none"> NE drifting ash plumes on May 20, 21, and 22 SE drifting ash on June 4 Lava fountaining and effusive activity on June 4 - 8 WSW drifting ash on June 5 and 6 SE drifting ash on June 8 – 10
June 11, 2013 (after 21:14:47 UTC) – June 28, 2013 [<i>L8</i>] (before 21:54:27 UTC)	<ul style="list-style-type: none"> Intermittent, minor ash drifting to the SE on June 12 and 13 Intermittent, minor ash drifting to the SE on June 14 SW drifting ash on June 25 NW drifting ash on June 26
June 28, 2013 (after 21:54:27 UTC) – June 29, 2013 [<i>ASTER TIR</i>] 08:34:24 UTC) through August 8, 2013	<ul style="list-style-type: none"> Elevated surface temperatures signifying cooling lava flow seen in multiple nighttime images at through the beginning of July Return to background levels of activity. Volcano officially brought down to NORMAL Volcano Alert Level and GREEN Aviation Color Code on August 8

* Acquisition time is scene center time for Landsat and median time of acquisition for ALI and Hyperion imagery

** Information from public weekly updates from the United States Geological Survey Alaska Volcano Observatory, pilot reports, and unpublished AVO data.

Table 3.8. Summary of 2013 Pavlof deposit measurements made from imagery used to study the eruption.

Image date	Deposit type (deposit number in Figures 3.27 and 3.28)	Total visible deposit area	Deposit area on perennial snow/ice	Deposit area on seasonal snow	Area intersected with previous deposits
May 16, 2013	Lava flow (5)	0.2 km ²	0.03 km ²	0.05 km ²	-----
May 16, 2013	Possible lava flow or pyroclastic density current (6)	0.07 km ²	0.04 km ²	0.03 km ²	-----
May 16, 2013	Possible meltwater (7)	0.08 km ²	0.01 km ²	0.07 km ²	-----
May 19, 2013	Lahar(s) (9)	4.3 km ²	0 km ²	3.5 km ²	-----
June 28, 2013	Lava flows (11)	0.3 km ²	0.1 km ²	0.2 km ²	0.002 km ² (with lava flow from May 16)
June 28, 2013	Lahar(s) (12)	1.5 km ²	0 km ²	1.5 km ²	0.5 km ² (with lahar from May 19)
June 28, 2013	Unknown deposits (13)	0.2 km ²	0.09 km ²	0.07 km ²	-----

References

- Adhikary, S., Yamaguchi, Y., and Ogawa, K. 2002: Estimation of snow ablation under a dust layer covering a wide range of albedo: *Hydrological Processes*, v.16, 2853-2865.
- Alaska Volcano Observatory. (2014, February 28). *Pavlof reported activity*. Retrieved from www.avo.alaska.edu
- Belousov, A., Behncke, B., and Belousova, M. 2011: Generation of pyroclastic flows by explosive interaction of lava flows with ice/water-saturated substrate: *Journal of Volcanology and Geothermal Research*, v. 202, 60 – 72.
- Bleick, H.A., Coombs, M.L., Cervelli, P.F., Bull, K.F., and Wessels, R.L. 2013: Volcano-ice interactions precursory to the 2009 eruption of Redoubt Volcano, Alaska: *Journal of Volcanology and Geothermal Research*, 373 - 388.
- Björnsson, H. 2003: Subglacial lakes and jökulhlaups in Iceland: *Global and Planetary Change*, v. 35, 255 – 271.
- Björnsson, H. 2010: Understanding jökulhlaups: from tale to theory: *Journal of Glaciology*, v. 56, n. 200, 1002 – 1010.
- Boresjö Bronge, L. and Bronge, C. 1999: Ice and snow-type classification in the Vestfold Hills, East Antarctica, using Landsat-TM data and ground radiometer measurements: *International Journal of Remote Sensing*, v. 20, n. 2, 225 – 240.
- Bull, K.F. and Buurman, H. 2013: An overview of the 2009 eruption of Redoubt Volcano, Alaska: *Journal of Volcanology and Geothermal Research*, v. 259, 2 – 15.
- Dean, K.G., Dehn, J., Papp, K.R., Smith, S., Izbekov, P., Peterson, R., Kearney, C., and Steffke, A. 2004: Integrated satellite observations of the 2001 eruption of Mt. Cleveland, Alaska: *Journal of Volcanology and Geothermal Research*, v. 135, 51 – 73.
- Dehn, J., Dean, K., and Engle, K. 2000: Thermal monitoring of North Pacific volcanoes from space: *Geology*, v. 28, n. 8, 755 – 758.
- Dehn, J., Dean, K.G., Engle, K., and Izbekov, P. 2002: Thermal precursors in satellite images of the 1999 eruption of Shishaldin Volcano: *Bulletin of Volcanology*, v. 64, 525 – 534.
- Diefenbach, A.K., Bull, K.F., Wessels, R.L., and McGimsey, R.G. 2013: Photogrammetric monitoring of lava dome growth during the 2009 eruption of Redoubt Volcano: *Journal of Volcanology and Geothermal Research*, v. 259, 308 – 316.
- Driedger, C. 1981: Effect of ash thickness on snow ablation. In P. W. Lipman, & D. R. Mullineaux (Eds.), *The 1980 eruptions of Mt. St. Helens, Washington*, USGS professional paper, v. 1250, 757–760. Washington, DC: U.S. Geological Survey.
- Dunning, S.A., Large, A.R.G., Russell, A.J., Roberts, M.J., Duller, R., Woodward, J., Mériaux, A.S., Tweed, F.S., and Lim, M. 2013: The role of multiple glacier outburst floods in proglacial landscape evolution: the 2010 Eyjafjallajökull eruption, Iceland: *Geology*, v. 41, n. 10, 1123 – 1126.

- Edwards, B., Magnússon, E., and Thordarson, T. 2012: Interactions between lava and snow/ice during the 2010 Fimmvörðuháls eruption, south-central Iceland: *Journal of Geophysical Research*, v.117, 1-21.
- Eliasson, J., Larsen, G., Gudmundsson, M.T., and Sigmundsson, F. 2006: Probabilistic model for eruptions and associated flood events in the Katla caldera, Iceland: *Computational Geosciences*, v. 10, 179 – 200.
- Hall, D.K., Foster, J.L., Verbyla, D.L., Klein, A.G., and Benson, C.S. 1998: Assessment of Snow-Cover Mapping Accuracy in a Variety of Vegetation-Cover Densities in Central Alaska: *Remote Sensing of Environment*, v. 66, 129-137.
- Kennedy, G.C. and Waldron, H.H. 1955: Geology of Pavlof Volcano and Vicinity Alaska: Investigations of Alaskan Volcanoes: *Geological Survey Bulletin 1028 – A*.
- Kerle, N., van Wyk de Vries, B., and Oppenheimer, C. 2003: New insight into the factors leading to the 1998 flank collapse and lahar disaster at Casita volcano, Nicaragua: *Bulletin of Volcanology*, v. 65, no. 5, 331 – 345.
- König, M., Winter, J.G., and Isaksson, E. 2001: Measuring snow and glacier ice properties from satellite: *Reviews of Geophysics*, v. 39, Issue 1, 1 – 27.
- Major, J.J. and Newhall, C.G. 1989: Snow and ice perturbation during historical volcanic eruptions and the formation of lahars and floods: A global review: *Bulletin of Volcanology*, v. 52, 1-27.
- Martínez, M., Fernández, E., Valdés, J., Barboza, V., Van der Laat, R., Duarte E., Malavassi, E., Sandoval, L., Barquero, J., and Marino, T. 2000: Chemical evolution and volcanic activity of the active crater lake of Poás volcano, Costa Rica, 1993 – 1997: *Journal of Volcanology and Geothermal Research*, v. 97, issue 1-4, 127 – 141.
- Maxwell, S.K., Schmidt, G.L., and Storey, J.C. 2007: A multi-scale segmentation approach to filling gaps in Landsat ETM⁺ SLC-off images: *International Journal of Remote Sensing*, v. 28, Issue 23, 5339 – 5356.
- McNutt, S.R. 1987. Eruption characteristics and cycles at Pavlof volcano, Alaska, and their relation to regional earthquake activity: *Journal of Volcanology and Geothermal Research*, v. 31, 239 – 267.
- Miller, T.P. and Chouet, B.A. 1994: The 1989 – 1990 eruptions of Redoubt Volcano: an introduction: *Journal of Volcanology and Geothermal Research*, v. 62, 1-10.
- Morisette, J.T., Giglio, L., Csiszar, I., and Justice, C.O. 2005: Validation of the MODIS active fire product over Southern Africa with ASTER data: *International Journal of Remote Sensing*, v. 26, n. 19, 4239 – 4264.
- Nye, C.J., Keith, T.E.C., Eichelberger, J.C., Miller, T.P., McNutt, S.R., Moran, S., Schneider, D.J., Dehn, J., and Schaefer, J.R. 2002: The 1999 eruption of Shishaldin Volcano, Alaska: monitoring a distant eruption: *Bulletin of Volcanology*, v. 64, 507 – 519.
- Paguican, E.M.R., Lagmay, A.M.F., Rodolfo, K.S., Rodolfo, R.S., Tengonciang, A.M.P., Lapus, M.R., Baliatan, E.G., and Obille Jr., E.C. 2009: Extreme rainfall-induced lahars and dike breaching, 30 November 2006, Mayon Volcano, Philippines: *Bulletin of Volcanology*, v. 71, 845-857.

- Pierson, T.C., Janda, R.J., Thouret, J.C., and Borrero, C.A. 1990: Perturbation and melting of snow and ice by the 13 November 1985 eruption of Nevado del Ruíz, Colombia, and consequent mobilization, flow and deposition of lahars: *Journal of Volcanology and Geothermal Research*, v. 41, issues 1-4, 17-66.
- Pierson, T.C. 2005: Hyperconcentrated flow - transitional processes between water flow and debris flow. In Jakob, M. and Hungr, O. (Eds.), *Debris-flow Hazards and Related Phenomena*, 159-202. Berlin, Heidelberg: Springer Praxis.
- Power, J.A., Stihler, S.D., Chouet, B.A., Haney, M.M., and Ketner, D.M. 2013: Seismic observations of Redoubt Volcano, Alaska – 1989-2010 and a conceptual model of the Redoubt magmatic system: *Journal of Volcanology and Geothermal Research*, v. 259, 31 – 44.
- Procter, J., Cronin, S.J., Fuller, I.C., Lube, G., and Manville, V. 2010: Quantifying the geomorphic impacts of a lake-breakout lahar, Mount Ruapehu, New Zealand: *Geology*, v. 38, n. 1, 67 – 70. f
- Ramsey, M., and Dehn, J. 2004: Spaceborne observations of the 2000 Bezymianny, Kamchatka eruption: the integration of high-resolution ASTER data into near real-time monitoring using AVHRR: *Journal of Volcanology and Geothermal Research*, v. 135, issues 1 – 2, 127 – 146.
- Rivera, A., Bown, F., Mella, R., Wendt, J., Casassa, G., Acuña, C., Rignot, E., Clavero, J., and Brock, B. 2006: Ice volumetric changes on active volcanoes in southern Chile: *Annals of Glaciology*, v.43, 111-122.
- Roach, A.L., Benoit, J.P., Dean, K.G., and McNutt, S.R. 2001: The combined use of satellite and seismic monitoring during the 1996 eruption of Pavlof volcano, Alaska: *Bulletin of Volcanology*, v. 62, Issue 6 – 7, 385 – 399.
- Schaefer, J. 2012: The eruption of Redoubt Volcano, Alaska. Alaska Division of Geological and Geophysical Surveys Report of Investigations, 2012 – 2015.
- Sidjak, R.W. and Wheate, R.D. 1999: Glacier mapping of the Illecillewaet icefield, British Columbia, Canada, using Landsat TM and digital elevation data: *International Journal of Remote Sensing*, v. 20, n. 2, 273 - 284.
- Smellie, J.L. 2006: The relative importance of supraglacial versus subglacial meltwater escape in basaltic subglacial tuya eruptions: An important unresolved conundrum: *Earth-Science Reviews*, v.74, 241 – 268.
- Sturm, M., Benson, C., and MacKeith, P. 1986: Effects of the 1966 – 68 eruptions of Mount Redoubt on the flow of Drift Glacier, Alaska, U.S.A.: *Journal of Glaciology*, v. 32, n. 112, 355 – 362.
- Trabant, D.C. and Meyer, D.F. 1992: Flood generation and destruction of “Drift” Glacier by the 1989 – 90 eruption of Redoubt Volcano, Alaska: *International Glaciological Society*, v. 16, 33 – 38.
- Trabant, D.C., Waitt, R.B., Major, J.J. 1994: Disruption of Drift glacier and origin of floods during the 1989-1990 eruptions of Redoubt Volcano, Alaska: *Journal of Volcanology and Geothermal Research*, v. 62, issues 1-4, 369-385.
- Trabant, D.C. and Hawkins, D.B. 1997: Glacier Ice-Volume Modeling and Glacier Volumes On Redoubt Volcano, Alaska: *U.S. Geological Survey Water-Resources Investigations Report 97-4187*.

- Waitt, R.B., Gardner, C.A., Pierson, T.C., Major, J.J., and Neal, C.A. 1994: Unusual ice diamicts emplaced during the December 15, 1989 eruption of Redoubt volcano, Alaska: *Journal of Volcanology and Geothermal Research*, v. 62, issues 1 – 4, 409 – 428.
- Wallace, K.L., Schaefer, J.R., Coombs, M.L. 2013: Character, mass, distribution, and origin of tephra-fall deposits from the 2009 eruption of Redoubt Volcano, Alaska – Highlighting the significance of particle aggregation: *Journal of Volcanology and Geothermal Research*, v. 259, 145 – 169.
- Walder, J.S. 2000a: Pyroclast/snow interactions and thermally driven slurry formation. Part 1: Theory for monodisperse grain beds: *Bulletin of Volcanology*, v. 62, 105-118.
- Walder, J.S. 2000b: Pyroclast/snow interactions and thermally driven slurry formation. Part 2: Experiments and theoretical extension to polydisperse tephra: *Bulletin of Volcanology*, v. 62, 119-129.
- Walder, J.S. 2010: Erosion and entrainment of snow and ice by pyroclastic density currents: some outstanding questions: *Abstract from the American Geophysical Union, Fall Meeting 2010*.
- Watanabe, T. 1988: Studies of snow accumulation and ablation on perennial snow patches in the mountains of Japan: *Progress in Physical Geography*, v. 12, 560 – 581.
- Waythomas, C.F., Miller, T.P., Mangan, M.T. 2006. Preliminary volcano hazard assessment for the Emmons Lake Volcanic Center, Alaska. United States Geological Survey Scientific Investigations Report 2006 – 5248, 33 p.
- Waythomas, C.F., Prejean, S.G., and McNutt, S.R. 2008: Alaska's Pavlof Volcano Ends 11-Year Repose: *EOS, Transactions, AGU*, v. 89, issue 23, 209 – 211.
- Waythomas, C.F., Pierson, T.C., Major, J.J., and Scott, W.E. 2013: Voluminous ice-rich and water-rich lahars generated during the 2009 eruption of Redoubt Volcano, Alaska: *Journal of Volcanology and Geothermal Research*, v. 259, 389 - 413.
- Waythomas, C.F. 2014: Water, ice and mud: lahars and lahar hazards at ice- and snow-clad volcanoes: *Geology Today*, v. 30, n. 1, 34 – 39.
- Webley, P.W., Lopez, T.M., Ekstrand, A.L., Dean, K.G., Rinkleff, P., Dehn, J., Cahill, C.F., Wessels, R.L., Bailey, J.E., Izbekov, P., Worden, A. 2013: Remote observations of eruptive clouds and surface thermal activity during the 2009 eruption of Redoubt volcano: *Journal of Volcanology and Geothermal Research*, v. 259, 185 – 200.
- Wessels, R., Neal, C.A., Waythomas, C., Huggel, C., and Dean, K. 2007: Satellite measurement of glaciers on volcanoes in Alaska: Building an inventory of ice extent and hazards: *Abstract from the 103rd Annual Meeting of the Cordilleran Section of the Geological Society of America*
- Wilson, L. and Head, J.W. 2007: Heat transfer in volcano-ice interactions on Earth: *Annals of Glaciology*, v.45, no. 1, 83-86.
- Xiao, X., Shen, Z., and Qin, X. 2001: Assessing the potential of VEGETATION sensor data for mapping snow and ice cover: a Normalized Difference Snow and Ice Index: *International Journal of Remote Sensing*, v. 22, n. 13, 2479 - 2487.

Chapter 4 Conclusion

4.1 Comparison of snow/ice cover mapping methods for Alaskan volcanoes

We analyzed two different methods of snow/ice cover mapping for Redoubt and Pavlof volcanoes in Chapter 2:

- 1.) Threshold method using combinations of principal component analysis, band ratioing techniques including the Normalized Difference Snow Index (NDSI), and manual pixel mapping using visual inspection of the image where necessary.
- 2.) Linear spectral unmixing analysis

Threshold mapping of the snow/ice cover area required supplemental manual mapping for 11 out of 21 of the Redoubt images and 19 out of 21 of the Pavlof images. When comparing the threshold method with the linear spectral unmixing method, the percent variance between the two methods was generally smaller for the Pavlof region than the Redoubt region. However, the use of one method did not consistently result in a larger area of snow/ice cover to be mapped than the other method. One possible reason for this inconsistency is variations in shadow and illumination between images. Although we took into account the effect of illumination on the image during pre-processing, this may not have been enough to completely remove the influence of variations in illumination on sub-pixel spectral signals (Foppa et al., 2002). Nearly every resulting snow/ice endmember image from the linear spectral unmixing analysis for both volcanoes contained pixels with a percentage value over 1, meaning over 100% of the pixel contains snow/ice. This suggests that snow/ice pixels may exist within the image

that are more spectrally pure than those chosen as the snow/ice endmember using the PC1 versus PC2 scatter plot (EXELIS, 2014). The number of pixels with a value over 1 varied from under 100 to over 100,000 pixels in the Redoubt and Pavlof images analyzed. By using the first iteration snow/ice endmember result, the 100 pixels with the highest percentage value over 1 were then used as the snow/ice input for a second and possibly third iteration linear spectral unmixing analysis. The majority of images required only one additional iteration after the original linear spectral analysis to reduce the number of pixels with high percentage values to less than 100. By greatly reducing the number of pixels with unrealistic percentage values, this helps to provide a more accurate representation of the distribution of snow/ice cover within each image.

While validation using ground control points was beyond the scope of this study, the effectiveness of the linear spectral unmixing method was tested using a 1m resampled IKONOS image. The snow/ice cover area delineated using the higher spatial resolution image was within 0.5 km² of the area mapped using the linear spectral unmixing analysis. This was the only time-coincident high resolution image available, yet this comparison suggests that the linear spectral unmixing analysis is accurate at a higher spatial resolution. Furthermore, the linear spectral unmixing method required less user input compared to the threshold method, which required manual mapping of snow/ice cover pixels for over half of the images for each volcano. Snow/ice cover maps produced from linear spectral unmixing were then used for the analyses in Chapter 3.

4.2 Mapping snow/ice on Redoubt and Pavlof during quiescence and eruption

We produced the following three products in Chapter 3, building on the in depth analysis of snow/ice cover mapping methods performed in Chapter 2:

Product 1.) Snow/ice cover area maps of individual images from the Alaskan summer ablation season,

Product 2.) Summer monthly maps showing the snow/ice cover area consistently present during multiple years for each month,

Product 3.) Maps spatially linking the snow/ice cover present with deposits produced during the 2009 eruption of Redoubt and 2013 eruption of Pavlof as well as an analysis on the changes to visible snow/ice cover area directly before, during, and after the eruptions.

The snow/ice cover area maps created in Products 1 and 2 reveal some interesting trends in how the snow/ice cover varies throughout the ablation season at Redoubt and Pavlof volcanoes. On average, seasonal snow disappears completely from the Drift River valley northeast of Redoubt volcano by July. Melting of seasonal snow by this point in the summer extends south past the furthest extent of the Drift Glacier piedmont lobe, revealing glacial ice covered by debris that could include ash from the previous 1989-1990 eruption (Trabant and Meyer, 1992). The presence of debris and ash cover over glacial ice at Redoubt is significant as, depending on thickness, ash or debris cover can either increase or insulate against melting (Driedger, 1981; Adhikary et al., 2002).

Seasonal snow has been a significant contributor of meltwater during previous eruptions at Redoubt volcano (Trabant et al., 1994). Therefore, conclusions about the disappearance of seasonal snow within the Drift River valley could have large implications for hazards associated with meltwater generation during an eruption. Based on the snow/ice cover area maps made in Products 1 and 2, the largest percent decrease in the snow/ice cover area at Redoubt occurs between July and August. Therefore, an eruption at Redoubt in May, June, or even July could be more hazardous in terms of lahars than an eruption of similar size in August. More work is needed in understanding this, however, in that some researchers suggest the removal of snow and ice can expose loose sediments that could also contribute to lahar formation (see Waythomas, 2014). A rough approach to determining the first date of fresh snowfall showed that most snow first falls in the Redoubt area at around the end of September to October.

We analyzed snow/ice cover area within the Pavlof subset against a Pavlof Sister subset. At the boundaries of the Alaskan ablation season, in April and October, the seasonal snow within the Pavlof Sister subset is greater due to a high elevation region along the northwestern corner of the subset, approximately 15 km NW of the summit of Pavlof Sister. However, from May through August, there is a larger area of snow/ice cover within the Pavlof subset. This could be due to the influence of larger river drainages within the Pavlof Sister subset, where the seasonal snow tends to melt the fastest.

The largest percent decrease in the snow/ice cover within both the Pavlof and Pavlof Sister subsets occurs between June and July, while a small change in snow/ice

cover occurs between May and June. This is very interesting in that, if seasonal snow can be a contributor to meltwater generation (Trabant et al., 1994), there would be a distinct boundary between June and July during which this source of meltwater decreases with the large disappearance of seasonal snow.

After the 2009 eruption of Redoubt volcano, there was a dramatic decrease in the visible snow/ice cover area compared to the expected amount from the monthly snow/ice cover summary maps. While the average visible area of snow/ice cover in May is approximately 200 km^2 , the snow/ice cover on May 13, 2009, one month after the end of the explosive eruption, was less than 2 km^2 . Fresh snow fall occurred at the summit peak of the volcano by the next available cloud-free image on July 8, 2009, when approximately 3.5 km^2 of snow/ice cover was visible. An increase in seasonal snow occurred by September of 2009, with fresh snow fall on around September 24. July and August images acquired one and two years after the end of the eruption showed a smaller snow/ice cover area than expected by the monthly summary maps. This possibly suggests that the 2009 eruption of Redoubt volcano resulted in increased debris cover on the Drift Glacier and piedmont lobe.

No cloud-free images were available after the 2013 eruption of Pavlof volcano, making a direct comparison with expected snow/ice cover areas impossible. However, numerous partly-cloudy images were available during the eruption. The majority of ash emissions traveled south of Pavlof, however, ash plumes from May 19 through May 22 traveled northwest over the summit of Pavlof Sister. Views over the summit of both Pavlof and Pavlof Sister showed extensive ash cover at both volcanoes by June 2013.

The purpose of this study was to spatially connect the volcanic deposits produced during the 2009 Redoubt eruption and 2013 Pavlof eruption with the underlying snow/ice cover. Although the lahars from the 2009 eruption of Redoubt volcano appear to extensively cover the width of the Drift River valley, principal component analyses show the lahars to be quite channelized. Lahar deposits can then be divided into channel areas and bar areas, where overbank lahar mud was deposited in between channels similar to a braided river system (Procter et al., 2010). Only 38% of the lahar channels used from March 26 through April 1 were reused as channels by the April 4 lahars. Cloud-free imagery needed to study the channels utilized by the March 22-24 lahars does not exist, but other researchers report that the large March 23 lahars followed the main Drift River channel (Waythomas et al., 2013).

The majority of the flows produced during the 2013 eruption of Pavlof did not intersect regions of perennial snow and ice but instead were underlain by seasonal snow cover on suspected debris-covered ice. Once again, this could have implications for melt generation as debris cover can help to insulate glacial ice (Driedger, 1981).

4.3 Limitations and future work

One of the largest limitations of this study is the difficulty in mapping snow/ice under debris cover. There may be as much as 2 km³ of debris-covered glacial ice along Pavlof's flanks (Waythomas et al., 2006) and the appearance of debris-covered glacial ice at Redoubt is observed in snow/ice cover maps starting in July. Summer melt has also been observed to cause the redistribution of previously deposited ash over exposed snow

and glacial ice at Pavlof volcano (Kennedy and Waldron, 1955). Debris cover is a common occurrence at Alaskan glaciers and volcanic debris such as ash cover can affect the glaciers surrounding volcanoes for several decades after an eruption (Trabant and Meyer, 1992; Berthier et al., 2010). As previously mentioned, identification of the areas of debris cover on snow/ice is important as, depending on thickness, debris cover can either provide thermal insulation from melt or enhance melt (Driedger, 1981; Adhikary et al., 2002). Therefore, we make a first step at approximating the spatial location of these debris covered areas, however, more work is needed. One of the possible methods of mapping out where the debris cover is spatially located is using the linear spectral unmixing analysis already completed for each image and identifying the pixels that contain both snow/ice and rock endmembers (Sidjak and Wheate, 1999). This would at least map out the areas where the boundaries of debris covered snow/ice could be located.

Another possible area of future work is further development of physical models to test the meltwater generated from the interaction between seasonal snow, perennial snow, glacial ice, and hot volcanic products (Walder, 2000a, 2000b; Waythomas 2014). By better understanding the susceptibility that each snow/ice cover type has to melt during an eruption, the spatial information produced in our study can be better used to quantify the lahar hazards present at Redoubt, Pavlof, and many other snow/ice-covered volcanoes.

References

- Adhikary, S., Yamaguchi, Y., and Ogawa, K. 2002: Estimation of snow ablation under a dust layer covering a wide range of albedo: *Hydrological Processes*, v.16, 2853-2865.
- Berthier, E., Schiefer, E., Clarke, G.K.C., Menounos, B., and Rémy, F. 2010: Contribution of Alaskan glaciers to sea-level rise derived from satellite imagery: *Nature Geoscience*, v. 3, 92 – 95.
- Driedger, C. 1981: Effect of ash thickness on snow ablation. In P. W. Lipman, & D. R. Mullineaux (Eds.), *The 1980 eruptions of Mt. St. Helens, Washington*, USGS professional paper, v. 1250, 757–760. Washington, DC: U.S. Geological Survey.
- EXELIS. (2014, January 28). *Linear Spectral unmixing*. Retrieved from <http://www.exelisvis.com/docs/linearspectralunmixing.html#results>
- Foppa, N., Wunderle, S., and Hauser, A. 2002: Spectral Unmixing of NOAA-AVHRR Data for Snow Cover Estimation: *Proceedings of EARSeL-LISSIG-Workshop: Observing our Cryosphere from Space, Bern, March 11 – 13, 2002*, 8 p.
- Kennedy, G.C. and Waldron, H.H. 1955: Geology of Pavlof Volcano and Vicinity Alaska: Investigations of Alaskan Volcanoes: *Geological Survey Bulletin 1028 – A*
- Procter, J., Cronin, S.J., Fuller, I.C., Lube, G., and Manville, V. 2010: Quantifying the geomorphic impacts of a lake-breakout lahar, Mount Ruapehu, New Zealand: *Geology*, v. 38, n. 1, 67 – 70.
- Trabant, D.C. and Meyer, D.F. 1992: Flood generation and destruction of “Drift” Glacier by the 1989 – 90 eruption of Redoubt Volcano, Alaska: *International Glaciological Society*, v. 16, 33 – 38.
- Trabant, D.C., Waitt, R.B., Major, J.J. 1994: Disruption of Drift glacier and origin of floods during the 1989-1990 eruptions of Redoubt Volcano, Alaska: *Journal of Volcanology and Geothermal Research*, v. 62, issues 1-4, 369-385.
- Sidjak, R.W. and Wheate, R.D. 1999: Glacier mapping of the Illecillewaet icefield, British Columbia, Canada, using Landsat TM and digital elevation data: *International Journal of Remote Sensing*, v. 20, n. 2, 273 - 284.
- Walder, J.S. 2000: Pyroclast/snow interactions and thermally driven slurry formation. Part 1: Theory for monodisperse grain beds: *Bulletin of Volcanology*, v. 62, 105-118.
- Walder, J.S. 2000: Pyroclast/snow interactions and thermally driven slurry formation. Part 2: Experiments and theoretical extension to polydisperse tephra: *Bulletin of Volcanology*, v. 62, 119-129.
- Waythomas, C.F., Miller, T.P., Mangan, M.T. 2006. Preliminary volcano hazard assessment for the Emmons Lake Volcanic Center, Alaska. United States Geological Survey Scientific Investigations Report 2006 – 5248, 33 p.
- Waythomas, C.F., Pierson, T.C., Major, J.J., and Scott, W.E. 2013: Voluminous ice-rich and water-rich lahars generated during the 2009 eruption of Redoubt Volcano, Alaska: *Journal of Volcanology and Geothermal Research*, v. 259, 389 - 413.
- Waythomas, C.F. 2014: Water, ice and mud: lahars and lahar hazards at ice- and snow-clad volcanoes: *Geology Today*, v. 30, n. 1, 34 – 39.

